JOINT EUROPEAN TORUS

JET–P(91)46

J.P. Christiansen, J.G. Cordey, K. Thomsen, A. Tanga and the JET Team*
J. Deboo, D. Schissel, T. Taylor and the DIII-D Team O. Kardaun, F. Wagner,
F. Ryter and the ASDEX Team S.M. Kaye and the PDX and PBX-M Teams
Y. Miura, N. Suzuki, M. Mori, T. Matsuda, H. Tamai, T. Takizuka,
S-I Itoh, K. Itoh and the JFT-2M Team

A Global Energy Confinement H-Mode Database for ITER

A Global Energy Confinement H-Mode Database for ITER

J.P. Christiansen, J.G. Cordey, K. Thomsen, A. Tanga and the JET Team*
J. Deboo[1], D. Schissel[1], T. Taylor[1] and the DIII-D Team O. Kardaun[2], F. Wagner[2],
F. Ryter[2] and the ASDEX Team S.M. Kaye[3] and the PDX and PBX-M Teams
Y. Miura[4], N. Suzuki[4], M. Mori[4], T. Matsuda[4], H. Tamai[4], T. Takizuka[4],
S-I Itoh[5], K. Itoh[5] and the JFT-2M Team

JET-Joint Undertaking, Culham Science Centre, OX14 3DB, Abingdon, UK

[1]General Atomic, San Diego, California, USA
[2]Max-Planck Institut fiir Plasmaphysik, Garching, Germany
[3]Princeton Plasma Physics Laboratory, NJ, USA
[4]Japan Atomic Energy Research Institute, Ibaraki. 319-11, Japan
[5]National Institute Fusion Science, Nagoya, 464-01, Japan
** See Appendix 1*

Preprint of Paper to be submitted for publication in
Nuclear Fusion

ABSTRACT.

This paper describes the content of an H-mode confinement database that has been assembled for the ITER project. Data are collected from six machines of very different sizes ASDEX, DIII-D, JET, JFT2M, PBX-M and PDX. A detailed description of the criteria that are used in the selection of data and the definition of each of the variables are given. After an analysis of the condition of the database, scalings of the energy confinement time with both the engineering and physics variables are determined. Both power law and offset linear models are used to fit the data and the predictions of the confinement time in ITER using the different formulations are presented.

A global energy confinement H-mode data base for ITER

Contents

1. INTRODUCTION

In order to predict the global energy confinement time in the next generation of large tokamaks, such as ITER, it is essential to have data from machines of different sizes. At the request of the ITER project the authors of this paper have assembled H-mode global confinement data from six machines ASDEX, DIII-D, JET, JFT2M, PBX-M and PDX into a single database. The key features of the database are described in this report along with a preliminary analysis of the scaling of the energy confinement time τ_E. Similar multi-machine databases have been assembled by S. Kaye for L-mode data [1, 2]. Since many machines that are currently being designed rely on H-mode confinement to achieve ignition, it clearly would be sensible to base extrapolations on H-mode data rather than applying L-mode scaling with a multiplier.

To set up a database requires extensive analysis of which parameters should be included. The selection is predicated mainly by the confinement interest but the database may no doubt have other uses. The final parameter selection is described in section 2 of this report.

Ideally one would like to construct a database in which the data covers a wide region of the parameter space of interest. Unfortunately not all parameters are fully under the control of the experimentalists; for instance it is not always possible to pre-determine the density n in the H-mode. Certain regions of the parameter space are not accessible for reasons of either gross MHD stability or available input power P_T. Thus in section 3 of the paper we investigate correlations and collinearities between the parameters in the database. It is found that there are fairly strong correlations between plasma current I_p, P_T and geometrical parameters. Furthermore, the dimensionless physics variables ρ/a (larmor radius divided by scale length) and β are also correlated. Collinearity between variables restricts the precision with which the dependence of τ_E upon such variables can be determined. In section 4 the scaling of τ_E is studied. First H-mode enhancement factors for existing L-mode scaling expressions are determined. Then both power law and offset linear models are used to fit the data.

Finally in section 5 of the paper the results of the scaling studies are summarised and predictions are given for the H-mode confinement properties in ITER. The contents of this paper supercede the preliminary results which have been reported previously [3].

2. DATA SELECTION AND MAIN FEATURES

Several different types of improved confinement regimes have now been identified in a tokamak; supershots [4], ion cyclotron resonance heating (ICRH) of pellet fuelled plasmas [5], etc as well as the conventional H-mode regime. The key characteristic of the H-mode regime which distinguishes it from other enhanced confinement regimes is the sharp reduction of the H_α emission during the auxiliary heating phase. Only data from pulses which exhibit a clear reduction in the H_α emission are included in the database. This key H-mode feature which was first observed during neutral beam injection (NBI) heating of an X-point configuration on ASDEX [6], has now been observed with most heating schemes such as ohmic [7], electron cyclotron resonance heating (ECRH) [8], and ICRH [9,10,11] and lower hybrid resonance heating (LH) [12]. It has also been observed in limiter plasma configurations [13,14,15]. Only data from NBI heating of X-point configurations have been included in the present release of the database. The presently released database is identified as ITERHDB.1 to distinguish it from future releases (updates will be made on an annual or as needed basis).

The detailed characteristics of the data and the reasons for its selection from each machine are given in Appendix I. The main differences between the machines are in the occurrence of ELMs. In JET there is usually a long ELM-free period ~ 1 second (after the transition from the L-phase) in which the density n and radiated power P_{rad} increase with time. This period is then either terminated by ELMs or by a radiative collapse back to an L-mode. In some of the other machines the initial ELM-free period is usually very short or sometimes even non existent.

The ELM behaviour is also quite variable in each machine and hence is not easy to classify precisely. The behaviour is divided into three classes: (1) ELM-free when there is no observable ELM activity. This class is denoted by PHASE = H in the database. (2) Small or grassy ELMs are denoted by PHASE = HSELM. These are defined as irregular, usually high frequency very small H_α spikes at a lower level than in the preceding L-mode phase. (3) Large or isolated Giant ELMs are denoted PHASE = HGELM. These usually have an almost regular low frequency and are characterised by an amplitude that is larger than the preceding L-mode level. Although the distinction between these three phases is not precise in most pulses the labelling system has the advantage of being simple.

The six machines also have different divertor geometries, target-plates, limiter materials and conditioning techniques. The required procedures to obtain a good H-mode in the separate machines are described in Appendix II.

Differences in the diagnostics of the six tokamak machines lead to variations on the availability of some parameters. Hence the smoothing of the data and the error estimates show tokamak to tokamak variation. Detailed information is given in the database variable list of Appendix III.

The variable list in Appendix III is basically self explanatory; the units are all MKS with temperatures in eV and the geometry is shown in Fig. 1. One key element needed for the determination of the plasma thermal energy content W_{th} is an accurate estimate of the fast ion energy content W_f. The latter is presented in two forms (variables 60-63 of Appendix III). The variables WFPER and WFPAR denote the perpendicular and parallel fast ion energy content obtained numerically from Fokker-Planck calculations or Monte-Carlo simulations. Such calculations are fairly time consuming and are thus only completed for a few representative shots. The results are supplemented by the variables WFFORM (the total fast ion energy) which is obtained from an approximate formula and WFANI which is an estimate of the ratio of perpendicular to total fast ion energy $W_{\perp f}/W_f$.

The time points for data selection are chosen well clear of changes in the power input but it is not always possible, as mentioned earlier, to choose steady state time points in the ELM-free period for some devices. However, the time derivatives of the density and the energies are given. Further information on the time development of the parameters are shown in review sheets made for each shot. Typical examples from each machine are shown in Figures 2-7. A complete set of these review sheets is available for inspection at each participating laboratory [16].

2.1 The standard ITER H-mode dataset

The entire ITER H-mode database contains 3466 Ohmic, L-mode, and H-mode time slices from 979 discharges. The H-mode data cover a wide range of parameter space including some data with degraded confinement. A set of selection criteria has been established to single out a subset of H-mode data. The subset is referred to as the standard dataset. The selection criteria for the standard dataset are:

1. Select H-mode only, with and without ELMs

2. Omit high radiation discharges, $P_{rad}/P_T \leq 0.6$ where $P_T = P_{abs} + P_{ohm}$
3. Limit fast ion content, $W_f/W \leq 0.40$
4. Omit degraded confinement due to sawtooth and beam deposition effects.
5. Limit transient discharges, $-0.05 \leq \dot{W}/P_T \leq 0.35$
6. Omit discharges with excessive MHD activity near a beta limit

The first criterion is accomplished by including only observations with phase H, HGELM, or HSELM which eliminates all Ohmic and L-mode data. The criterion discards approximately half of the JET and ASDEX observations and about one-third of the JFT2M observations. Table I shows separately for each tokamak the number of observations eliminated by each of the above criteria. Since numerous observations can be eliminated by several constraints the sum of eliminated observations is greater than the total.

There are special situations which occur when discharges with a high radiated power fraction are eliminated. All PDX discharges and about two-thirds of the ASDEX discharges have missing entries for P_{rad}. However, the PDX and ASDEX team members have estimated that these discharges comply with the restriction that P_{rad}/P_T is less than 60%. Consequently all ASDEX and PDX discharges with missing P_{rad} values have been accepted. Approximately one-half of the DIII-D observations also have missing entries for P_{rad} but do have a radiated power trace on the review sheets included with the database e.g. see Fig. 3. By examining these traces the DIII-D team found that data with P_{rad} missing can be accepted apart from the following observations (shot number. time): 062950.03100, 064446.03450, 064514.03150, 064514.02050, 064519.02060, 064523.02020, 062879.02490, 067801.02500, and 062881.02440. For JET data with P_{rad} missing only the following observations can be accepted: 017010.55800, 017010.56300, and 017010.56590.

The limit on the fast ion energy content is accomplished by the variable WFFORM. ASDEX has no data for WFFORM (see section 4) but in the team members opinion the fast ion fraction is less than 40% for almost all of the ASDEX observations. Therefore, all ASDEX data with WFFORM missing have been accepted. Some of the DIII-D data have WFFORM missing but the team members indicate that these discharges satisfy the 40% criterion. With the

constraint on the fast ion fraction set to less than or equal to 40% only a few discharges are eliminated from each machine. If this criterion is made more restrictive then the ASDEX data are essentially eliminated entirely, since fast ion fractions of order 30% were deemed quite possible in their data.

Transient observations are eliminated by constraining the ratio of $\dot{W}/P_T$. The $\dot{W}/P_T$ constraint is applied to $\dot{W}$ determined from MHD fits and from diamagnetic measurements (if available).

Another constraint is to eliminate discharges with degraded confinement due to a combination of sawteeth and beam deposition effects. This is often discussed in terms of degraded confinement at low safety factor q. Work on JET [17] and recent experiments on DIII-D [18] indicate that the proper parameter may not be q but rather some function of I_p/B_T. On DIII-D the degradation of confinement begins near I_p [MA]/B_T [T] ≈ 1 which for the typical elongations κ corresponds to $q_{95} \approx 3$ (q at the flux surface that encloses 95% of the total poloidal flux). Each team has estimated the constraint for their machine needed to eliminate degraded confinement. The selection criterion is $q_{95} \geq 3.1$ for JET, ASDEX and DIII-D, while it is $q_{95} \geq 2.7$ for JFT2M. The effects being eliminated do not exist in the PDX and PBX-M data and hence all values of q_{95} can be accepted for these two machines. About one-third of the ASDEX data and one-fourth of the JFT2M data are eliminated by this constraint. For JET some of the observations do not have a q_{95} value. In these few cases the expression

$$q^*_{95} \equiv \frac{5a^2 B_T}{R I_p}\left(\frac{1+\kappa^2}{2}\right)\left[1+\frac{3}{2}\left(\frac{a}{R}\right)^2\right] \qquad (1)$$

is used to apply the constraint. In Eq. (1) B_T, R and a denote toroidal magnetic field, major radius and minor radius, respectively. Only 27 JET discharges are eliminated by this selection criterion. It has been decided to formulate a scaling expression that applies only to discharges with no degraded confinement as a result of sawteeth and beam deposition effects. Since at present it is not possible to predict for future machines where this type of degradation will occur, it is also not possible to determine the precise value of q above which the derived scaling expressions apply.

The final selection criterion aims at eliminating those observations with excessive MHD activity which also can degrade confinement. This type of activity is typically observed as the beta limit is approached in DIII-D although not all discharges near a beta limit exhibit excessive MHD activity. Since JET and JFT2M do not operate near a beta limit the constraint is not necessary. The constraint imposed is $\beta_T \leq 4.0 \times 10^{-8}\ I_P$ [A]/a[m] B_T [T] for PBX-M and $\beta_T \leq 2.8 \times 10^{-8}\ I_p$ [A]/a[m] B_T [T] for PDX. For ASDEX the beta limit does not influence the confinement scaling very much and the constraint does therefore not apply. Before submission to the ITER database the DIII-D data have been checked against excessive MHD activity by monitoring magnetic probe signals; hence no constraint is required.

Several other minor constraints must be applied before the standard dataset is complete. Pellet fuelled discharges are removed from the standard dataset (a few JFT2M discharges) by allowing the PELLET parameter to be missing or not equal to H or D when it exists. ASDEX data obtained with a carbonized vessel are eliminated by not allowing the EVAP parameter to be equal to CARB. There are a few observations with missing density (DIII-D) and a few with missing diamagnetic confinement data (JET) that survive the above selection. These observations are also removed from the standard dataset.

The net number of observations in the standard dataset is 1239 (see Table I) with a significant contribution from each tokamak. The parameter ranges covered by the standard dataset for the database as a whole and for each individual machine are given in Table II.

2.2 Dataset for offset linear scaling analysis

In section 4.4 an offset linear scaling model for the thermal energy content W_{th} is examined. The method of analysis is different from the regression analysis applied to power law models. The dataset which is used in the analysis is defined by another set of selection criteria. The resulting dataset consists of 2 parts. The first part which forms the basis for the analysis is data selected from the D-shaped open divertor tokamaks DIII-D, JET and JFT2M. The 2nd part which is used for comparison is data selected from the closed divertor tokamaks ASDEX and PDX and from the bean shaped open divertor tokamak PBX-M.

The following criteria apply to all machines: (1) only data with a phase of H or HGELM are used; (2) since the thermal energy content is analysed instead of the energy confinement time the degree to which the discharge is not in steady state is restricted to $|\dot{W}/P_T| < 0.2$; (3) observations with a high fraction of radiation $P_{rad}/P_T > 0.6$ are omitted. In addition the following machine dependent selection criteria are applied:

For ASDEX: CONFIG = DN (double null X-point); $q_{95} > 3$.

For DIII-D: CONFIG = SN (single null X-point); $q_{95} > 3$.

For JET: CONFIG = SN; $q^*_{95} > 3$; omit shots with SEPLIM ≤ 0 including observations with missing SEPLIM values. (If the distance between the separatrix and limiter is too small, the characteristics of the confinement in the open divertor configuration could be affected).

For JFT2M: CONFIG = SN; $q_{95} > 2.7$ (the window for the q-values is widened, because the degradation of confinement is first observed for $q_{95} < 2.7$); omit shots with pellets; balanced injection with bucket ion source BSOURCE = 801010 and $0 <$ COCTR < 1. One of the best conditions for the H-mode is observed with co-injection and duopigatron ion source BSOURCE = 603010. However this parameter region is too narrow so balanced injection with bucket ion source is chosen.

For PBX-M: CONFIG = DN; $3 < q_{95} < 4$.

For PDX: CONFIG = SN; $q_{95} > 3$; DALFDV/DALFMP > 4 (the ratio of divertor D_α emissivity to midplane D_α emissivity, see appendix I).

The net number of observations in this dataset is 480. The D-shaped open divertor part consists of 305 observations from DIII-D (102), JET (50) and JFT2M (153). The other part consists of 175 observations from ASDEX (96), PBX-M (54) and PDX (25).

3. COLLINEARITY AND REGRESSION STABILITY

One important aspect of regression analysis is the investigation of collinearity of the regression variables. It can give an answer to (i) how reliably the regression coefficients can be determined and (ii) how reliably a prediction for a new machine can be made from the available data, both under the assumption that the postulated model is correct.

A feature common of these two different problems is that a reliable determination may be impeded by collinearity in the data, which means that some of the regressor variables are to a high degree linear combinations of other variables. The effects of collinearity resemble those of an instability of a system with respect to perturbations. It is useful to distinguish between an instability due to a particular method of analysis and an instability arising from the properties of the available data. Collinearity is caused by little experimental variation in some of the regression variables e.g. B_T or q_{cyl}, and by correlation between regression variables, e.g. between l_p, P_L, and R. Both these aspects have to be taken into account in order to determine how well-conditioned the data are. Neglecting one of these aspects can lead to serious interpretation errors.

3.1 **Principal component analysis**

A standard method for examining properties of multivariate experimental data is to calculate principal components (p.c.'s) which are special linear combinations of the original variables. Correlations between p.c.'s are zero. The transformation matrix connecting the new and the old variables is orthogonal. A regression model which is linear (e.g. power law) is invariant under *any* linear transformation. However, the orthogonality condition simplifies and unifies some interpretations. A familiar geometrical picture is to represent all $N \times P$ values of the P regression variables as N points in P-dimensional space. Expressing the data in terms of the principal components is equivalent to looking at the data in a new coordinate system in which the axes are formed by the principal axes of the P-dimensional ellipse fitted to the first and second moments of the data. See Fig. 8 for a 2-dimensional example. The smallest p.c.'s correspond to directions in which the data are varied least; the standard deviation of a principal component is proportional to the length of the corresponding half-axis of the ellipse.

Two yardsticks that determine which p.c.'s are 'small' are discussed. The choice of yardstick depends on the purpose of the investigation. For the more physics oriented objective (i), the standard deviation λ_{pc} of each p.c. should be large with respect to the standard deviation λ_e of the measurement error in the same principal direction.

There are serious collinearity problems for $\lambda_e \simeq \lambda_{pc}$. With $\lambda_{pc} < \lambda_e \leq 4\lambda_{pc}$, the regression coefficients obtained by an ordinary least squares (OLS) fit have a non-negligible bias. In that case more advanced techniques based on measurement error models [19, 20] should be employed. If $\lambda_{pc} > 4\lambda_e$ the bias along that direction is less than 1/16 ~ 6% of the regression estimate, which shall be considered as negligible here.

From the engineering viewpoint (ii), it is important to have a small prediction uncertainty for the new machine. Hence, it is preferable that the standard deviation λ_{pc} of each p.c. is not small with respect to the distance λ_{ITER} between the new machine (ITER) and the database averages of the regression variables, i.e. ($< \log (I_p) >$, $< \log (n) >$, ...), along the corresponding principal direction.

The larger the ratio $\lambda_{ITER}/\lambda_{pc}$ becomes the more uncertain the prediction is in that direction. Given that about 95% of the datapoints projected on a particular principal axis lie within $2\lambda_{pc}$ of the database average, one may be inclined to regard directions for which $\lambda_{ITER} > 4\lambda_{pc}$ as relatively ill-conditioned for prediction. It should be noted however, that the prediction uncertainty due to those directions is precisely taken into account in the (OLS) prediction interval for the new machine, provided that the type of model is correct and provided that the standard regression can be trusted, i.e. $\lambda_e << \lambda_{pc}$.

3.2 Condition of the standard dataset and subsets

The condition for various subsets of the standard ITER H-mode dataset has been investigated. The restrictions leading to the standard dataset are discussed in detail in section 2.1. Some of these are more oriented towards isolating a regime in which a single physical process may be dominant (physics goal), rather than towards covering all of the parameter space thought to be relevant for future devices (engineering goal). For instance, the restriction $q_{95} > 3$ is an attempt to exclude discharges with degraded confinement due to sawteeth effects, thereby simplifying the regression analysis. In as much as a degraded confinement region [18, 22, 23] is excluded, the usefulness for making predictions for ITER, which has a relatively low value of q_{95}, is limited by this procedure.

Tables III to V summarise the results. Table III gives the mean values, standard deviations and the correlation matrix of the basic regression variables, all based on a natural logarithmic scale. A distinction between ELM-free and ELMy discharges has been made because the regression of the confinement time is expected to be different for those two types of discharges [21, 23]. From Table III it can be seen that the correlations and the ranges of many of the variables are considerable. It can also be perceived that the correlations in the ELM-free dataset are usually somewhat higher than in the ELMy dataset.

Table IV is constructed from a principal components analysis of the covariance matrix of the basic regression variables on a natural logarithmic scale. It means that multiplication with a constant factor is considered equally important for B_T, n, κ ..... etc. In Table IV, the column STD contains the square root of the elements of the diagonalised covariance matrix. An entry gives 1 standard deviation in absolute units of the corresponding principal component. Note that if the regressor variables are measured with random error then an element of STD estimates $\lambda_{pc} + \lambda_e$ instead of λ_{pc}. A row of the columns Log (I_p), Log (B_T) ,...., Log (κ) expresses a p.c. in the original variables. It reads for example p.c.1 = .80 log (I_p) + 0.10 log (B_T) + ..., etc. Because of the orthogonality of the transformation matrix the numbers in the j^{th} row can also be interpreted as the direction cosines of the j^{th} principal axis of the ellipse with respect to the original coordinate axes, j=1 ,....., 7.

The two yardsticks discussed in section 3.1 are displayed in the columns ERR and ITER. The column ERR gives the ratio between λ_e and STD along each of the principal directions. It is assumed that the standard deviations of the non-systematic measurement errors in I_p, B_T, n, P_L, R, A, κ are 1%, 1%, 5%, 5%, 0.5%, 1%, 1%, respectively and that the errors in these variables are uncorrelated. Under this assumption, the column ERR estimates the ratio between λ_e and $\lambda_{pc} + \lambda_e$. As discussed above, the bias of standard OLS regression is estimated to be less than 6% and hence considered negligible if ERR < 20%.

The column ITER gives the ratio between λ_{ITER} and STD along each of the principal directions. For ITER the design parameters (I_p, B_T, n, P_L, R, A, κ) = (22, 4.85, 1.24×10^{20}, 160, 6, 2.15, 2.2) [MA,T,m^{-3}, MW, m, ,] are used. Provided the model is correct, and ERR_j is small for j = 1 ,....., 7, the prediction error for the average confinement time of ITER at the above design parameters is proportional to

$$\sqrt{1+\sum_{j=1}^{7} ITER_j^2}.$$

From Table IV, it can be concluded that the condition of the database is quite reasonable as long as all 6 tokamaks are included.

There is of course always room for improvement: A linear combination of the two least principal components which certainly for the ELM-free shots are hardly distinguishable (their eigenvalues are almost the same) comes close to log (q_{cyl}) which is relatively small for ITER. In the subset of the data where τ_{dia} is available a problematic least principal component from both points of view emerges and it is strongly associated with R, R/a, and κ. This is largely due to the exclusion of PBX-M and PDX. Without PBX-M it becomes very difficult to disentangle the effects of the geometrical parameters within the present dataset.

Table V also shows that the two least eigenvalues and to a lesser extent also the associated eigenvectors of the standard dataset are not too different from those of the two separate datasets ELMs and no ELMs. Notice that for the diamagnetic subset PRIN6 and PRIN7 are swapped!

3.3 Selection of regressor variables

As a special topic in the area of selection of variables, it is discussed whether n and B_T should be excluded as variables in a regression analysis. It should be noted that neither B_T nor n is correlated with the problematic least principal component that arose. Expressed otherwise, the same features as discussed above persist if B_T and n are deleted from the variable list (see the first part of Table V). For simplicity only the 5^{th} p.c.'s are shown. Notice that if B_T is omitted, then the 5^{th} p.c. corresponds nearly to a linear combination of the 6^{th} and 7^{th} p.c. of Table IV. From collinearity considerations there is thus no reason to drop B_T and n as regression variables. Other considerations are based on the magnitude of the effect that the variables have on the regression. There are the following possibilities: (1) If both B_T and n have a negligible effect on τ_E, then including or excluding them will not alter the other regression coefficients. (2) If either B_T or n have a non-negligible effect on τ_E, then they should not be excluded especially since the design values of ITER or CIT are not close to the database average for these two variables. (3) If the dependence on B_T for large values of I_p is different from the dependence on B_T for small values of I_p, then a simple power law scaling with no interaction terms is not adequate and has to be adjusted. In this case it can be misleading to present any simple power law either with B_T and n included or excluded. Problems of this type occur in the standard dataset. The presence of interaction can be tested to a reasonable degree by statistical methods. The experimental alternative would be to have well designed B_T scans at various fixed values of the other plasma parameters.

3.4 Condition of open or closed divertor tokamak subsets

It has been suggested that the type of divertor, i.e. open or closed, may have a substantial influence on the confinement time [24, 25]. To investigate this, a scaling can be found for the open divertor tokamaks (DIII-D, JET, JFT2M, PBX-M). The prediction of this scaling for the closed divertor tokamaks (ASDEX and PDX) can then be compared with the actual observations on these machines. From the last part of Table V it can be seen that in the open divertor tokamak dataset a problematic least principal component has emerged which is strongly, but not exclusively, correlated with κ. This should also be clear from elementary considerations, as κ is 1.4, 1.6, 1.85, 1.85 for the open divertor tokamaks JFT2M, PBX-M, DIII-D, JET respectively but near 1 for the closed divertor tokamaks. The situation is aggravated by the fact that in the ELMY dataset,

there arerelatively few (9) shots from JFT2M. Furthermore, in the open divertor tokamak dataset κ is strongly correlated with variables having a wide range. Hence any statement on the relative position of the closed versus open divertor tokamaks is essentially based on a postulated magnitude of the effect of κ.

In Table VI the collinearity analysis is summarised for the open divertor tokamaks when κ is deleted as a regressor. As expected the situation for the diamagnetic subset is rather bad from both points of view (measurement errors and prediction for ITER), and it is due largely to the deletion of PBX-M. For the ELMY H-mode dataset with τ_{mhd} available (Table VI versus Table III) one observes a significant deterioration of the condition of the subset of all open divertor tokamaks with κ omitted compared to the set with all tokamaks and κ included. ERR = 0.15 implies an estimated bias in the ordinary least squares (OLS) regression coefficients of about 4%, whereas ERR = 0.25 implies that this estimated bias is about 10%. However, for the ELM-free shots the condition is roughly the same in both cases and ERR = 0.2, which means a roughly estimated bias of 1/16 = 6%.

The conclusion is that if κ is not included as a regressor then the condition of the ELM-free dataset of all 4 open divertor tokamaks is satisfactory for OLS analysis. Of course it should be mentioned that the results in that case depend on a postulated κ dependence (e.g. 0.0 or 0.5) which cannot be determined from the present open divertor dataset. This is one way of approaching the entanglement between the effect of κ and the divertor type, the other way being to infer the divertor effect from other experimental information. In any case, open divertor H-modes experiments in low κ machines would be the source to provide the necessary complementary information. Such information may exist in the PDX dataset for certain conditions (see discussion in Sec. 4 and Appendix I).

3.5 Condition of ELMy dataset with JET data excluded

The deletion of JET data from the ELMy dataset leads to the results displayed in Table VII. The interesting subset is the first part of the table (with ELM's and all tokamaks except JET). From the point-of-view of measurement errors, the situation is fine. However, there is a large prediction problem for ITER in the direction of the smallest principal component, the distance of the center of the database to ITER being 23 times as large as the spread (1 standard deviation)

of the data in that direction. The conclusion is that leaving out the ELMy data from JET would not be justified in the present context.

One could consider regressing the ELMy and ELM-free data together, but this does not seem to be a good idea because the ELM-free and ELMy data may scale differently. Not only is the constant term different but also the dependence on some of the plasma parameters. Furthermore, operating with and without ELM's is a physically meaningful distinction for ITER (particle exhaust, divertor load, etc.). Hence, the best thing to do is to analyse the ELM-free and the ELMy datasets separately and keep the ELMy JET data in the analysis.

4. THE SCALING OF THE ENERGY CONFINEMENT TIME

In this section the scaling of the global energy confinement is determined in terms of both the engineering variables I_p, n, P_L, B_T, a, R, etc and the dimensionless physics variables ν^*, ρ/a etc. For the engineering variables both power law and offset linear forms are used for the scaling expression.

In the analysis a total energy confinement time τ_E as well as thermal energy confinement time τ_{th} will be used. These are defined as follows:

$$\tau_E = W/P_L \quad \text{and} \quad \tau_{th} = (W-W_f)/P_L \qquad (2)$$

where the net input power P_L is defined as

$$P_L = P_{ohm} + P_{abs} - \dot{W} \qquad (3)$$

and W_f is the fast ion energy. However, before any regression can be performed it must be determined whether to use MHD or diamagnetic measurements for W, $\dot{W}$, and therefore τ_E. One choice is simply to use MHD values which are available for all tokamaks and observations in the standard dataset (1239 obs). If only diamagnetic values are used then the dataset is reduced to 693 obs. because diamagnetic measurements are not available for PBX-M [26] and PDX [27] and the contribution from DIII-D is reduced by 40%. It is also possible to choose MHD from certain tokamaks and use diamagnetic values from others without reducing the dataset. For example in the regression analysis presented in section 4.1.2 it has been decided to use MHD values for DIII-D, JFT2M, PBX-M and PDX, diamagnetic values for JET and MHD-like values for ASDEX for the total stored energy. The MHD-like stored energy for ASDEX

was computed from the diamagnetically determined stored energy W_{dia} in the following manner

$$W = W_{dia} + 0.75\ W_f\ (2\text{-}3\ WFANI) \qquad (4)$$

with WFANI representing the fast ion anisotropy ($W_{\perp f}/W_f$). The ASDEX team has used 0.3 for WFANI and W_f has been represented by 0.04×10^{19} PABS/NEL.[1]

4.1 Comparison with existing scaling expressions

The confinement times of the ITER H-mode database have been compared to the confinement times predicted by four popularly used L-mode scaling expressions, Goldston [28], Kaye-Big [2], ITER89-P [29], and Rebut-Lallia [30]. In the analysis the following estimates of τ_E are used: MHD values for DIII-D, JFT2M, PBX-M and PDX, diamagnetic values for JET and MHD-like values for ASDEX.

The average enhancement factors for the standard selection (1239 obs.) are 1.65, 2.02, 2.11, and 2.35 for Goldston, Kaye-Big, ITER89-P, and Rebut-Lallia respectively (see Table VIII). For the Rebut-Lallia scaling Fr = 2 (W = Fr × electron energy content) and Z_{eff} = 3 were assumed. The enhancement factor for the Rebut-Lallia scaling depends on Z_{eff}. For Z_{eff} = 2 and Z_{eff} = 4 the factor changes from 2.49 to 2.25. Unfortunately Z_{eff} estimates do not exist for most of the tokamaks and therefore the comparison with the Rebut-Lallia scaling is not strictly correct. The expressions, however, do not represent the data well in that the standard deviations of the enhancement factors are 28%, 26%, 22%, and 42%, respectively, compared with less than 13% for the best least squares fit to the data. This difference is statistically highly significant and suggests that the parametric dependences of the existing L-mode scalings do not represent those of the H-mode data very well. Figs. 9-12 show the experimental values of the confinement time plotted versus the L-mode fit values (after the enhancement factor is applied). It is clear that systematic differences among the groups of data from the different tokamaks exist. Therefore, the use of *enhanced* L-mode scaling expressions for extrapolation purposes can lead to an uncertain and biased prediction.

[1] Using the MHD-like values instead of the experimental MHD values does not lead to a significant change in the overall scaling.

4.2 Power law scaling for H-mode confinement

Regression analysis is performed on the standard dataset for a power law model with global plasma parameters as the regression parameters. The general functional form used in this section is

$$\tau_E \propto I_p^{\alpha_I} B_T^{\alpha_B} n^{\alpha_n} P_L^{\alpha_P} A^{\alpha_A} (R/a)^{\alpha_\varepsilon} R^{\alpha_R} \kappa^{\alpha_\kappa} \qquad (5)$$

with units of sec, MA, T, 10^{19} m^{-3}, MW, and m respectively. The variable $A = \frac{1}{2}(A_{gas} + A_{beam})$ denotes the effective plasma ion mass number. An offset-linear functional form is discussed in section 4.4.

4.2.1 *Individual machine scalings*

Before attempting to establish the α's of Eq. (5) for the standard dataset it is essential to assess the dependences for the individual machines. If these dependencies are similar for all machines, then a fit to the standard dataset according to Eq. (5) has a straightforward interpretation. The regression is performed with only I_p, B_T, n, and P_L since size/shape parameters are not significantly varied within one machine.

The individual machine results are shown for MHD and diamagnetic confinement in Table IX. The results of this study indicate no significant difference between MHD and diamagnetic for JFT2M and DIII-D but raise some concern for ASDEX and JET (see Table IX). For some of the ASDEX and JFT2M entries in Table IX, the uncertainties in α_B are larger than the exponents, and the change in σ of the fit when these parameters are removed is not statistically significant. The DIII-D fits are not included in Table IX since one-third of the discharges do not have a diamagnetic determination of W. Although the MHD and diamagnetic fits are similar for DIII-D, they do not reflect the true parametric dependence as is represented in Table X and are therefore not displayed. For ASDEX, the dependence on global parameters is essentially the same but the magnitude of the MHD τ_E values are systematically about 25% larger than the diamagnetic values. However, since the fast ion distribution in ASDEX is not isotropic (recall for ASDEX $W_{\perp f}/W_f \sim 0.3$), there is no reason to expect that the MHD determined τ_E should be the same as the diamagnetic τ_E.

For JET the MHD fit produces a 50% larger root mean square error (indicating a significant increase in the scatter of the data about the fit) than the diamagnetic results do for reasons not yet understood. Also the reason for the high B_T and the weak current dependence in the MHD fit is not understood. Typically, linear current scaling is observed experimentally during current scans [32]. The JET team indicate more confidence in the diamagnetic measurements. The choice of using diamagnetic values for JET and MHD values for DIII-D and JFT2M, and MHD-like values for ASDEX also raises some concern over the possibility of biasing results due to the fact that diamagnetic and MHD measurements have differing sensitivities to anisotropic velocity distributions which could occur through the fast ion distribution. Since the fast ion distribution in JET is nearly isotropic (WFANI ~ 0.75), the difference between MHD and diamagnetic measurements should be small and combining the JET diamagnetic confinement with MHD and MHD-like confinement from the other machines should not present any difficulties. If only diamagnetic data are chosen for all devices then less data are available for DIII-D and no data are available for PDX and PBX-M.

Individual regression results for JET, DIII-D, ASDEX, JFT2M, PBX-M and PDX are shown in Table X. The fits are done using the uncertainties in confinement time as indicated in Appendix III and given below Table X. The results displayed in the table indicate good agreement between machines on the power scaling but a substantial variation is seen in the current and toroidal field scaling. The large uncertainties in the exponents for PBX-M and PDX are due partly to a lack of variation in the parameters. Another effect is that the assumed error (25%) for these two machines is larger than that assumed for the other devices. The JET result in Table X shows a weaker current dependence than the other devices. It is also weaker than previously published JET [31,32] results which are based on an ELM-free dataset that contains some but not all of the 5 MA shots. This result is, however, in agreement with the results [21,23] of an analysis that takes these shots into account. The dependence of τ_E on toroidal field in Table X varies considerably amongst the five devices from $B_T^{0.53}$ in JET to $B_T^{-0.20}$ in ASDEX but with a large uncertainty (here, we disregard the PBX-M scaling since there was little variation in B_T in this dataset). For JFT2M and DIII-D (and almost for ASDEX), the statistical uncertainty in α_B is larger than the estimate of α_B and the change in the σ of the fit after removing B_T as a regressor variable is not statistically significant. Experimental results from ASDEX [24], DIII-D [32], and JFT2M [34] indicate that τ_E depends very weakly on B_T. JET [31]

results show a similar scaling of τ_E with B_T as Table X, although a smaller toroidal field dependence of $B_T^{0.3}$ is supported by more recent data[2]. The dependence of energy confinement on plasma density also varies from machine to machine. For DIII-D there is a strong correlation between density and current for cases where near steady state values of density have been achieved and therefore the dependence of confinement on n and I_p can not be determined simultaneously.

The variation in toroidal field and density dependence may be due to an inadequate model. When performing regression analysis on a large group of tokamak data taken over many years, the data can be taken under a wide variety of conditions. It is quite possible that some unknown parameters, that significantly affect τ_E, change over the years but they have not been included in the power law expression of Eq. (5). Regression on such a dataset may indicate trends that are not seen experimentally when a single parameter scan is performed. On the other hand also in single parameter scans, hidden parameters can affect the results. Hence, in case of a clash, the assumptions in both approaches should be scrutinized in order to resolve the paradox.

Only the data from DIII-D and JFT-2M contain a few cases with a pure hydrogen ($H^\circ \rightarrow H^+$) H-mode. All other machines have either pure deuterium ($D^\circ \rightarrow D^+$) or an unknown mixture of hydrogen and deuterium ($H^\circ \rightarrow D^+$, $D^\circ \rightarrow H^+$). The mass scaling that is determined in the fit for DIII-D is $A^{0.63 \pm 0.05}$. Another source of uncertainty is that in the cases with a mixture of hydrogen and deuterium the effective mass is assumed to be 1.5, the average value. Because of the paucity of mass scaling information when the standard dataset of all devices is fit together, a scaling of $A^{0.5}$ is assumed [35]. Since there is no Z variation in the database, the dependence on this parameter could not be addressed. However, it has been observed on DIII-D [33] that the helium (^4He) H-mode has the same value of τ_E as the hydrogen H-mode.

4.2.2 *Regression on the standard dataset*

Results of regression on the standard dataset are shown in the first category in Table XI. The uncertainty in confinement time values assumed to derive the errors in the regression coefficients is 17%, roughly the median of the

[2] This data will be included in ITERHDB.2.

uncertainties given in Appendix III. A striking result from this fit is that when the data from all machines are combined together a very strong B_T dependence results. As an aside, if the JET data are removed from the standard dataset the strong toroidal field dependence remains. Note that for the standard case a weak dependence on aspect ratio and hence minor radius (both at fixed R and κ), and a strong dependence on major radius is seen. This fit is displayed in Fig. 13 with data from each device distinguishable. Data from each machine lie reasonably close to the fit with the exception of PDX which exhibits confinement values considerably below this fit. PDX has previously reported low values of τ_E for small values of the compression ratio as reflected by the ratio of the divertor D_α emission to the mid-plane D_α emission. The PDX data which are below the fit in Fig. 13 are roughly consistent with this observation. The root mean square error about the fit is 15.5%.

4.2.3 *Regression on subsets of the standard dataset*

We now consider the question of whether a scaling expression based on a thermal confinement time yields any significant differences from one based on total confinement time. Then regression results for ELM-free and ELMy data are compared and finally whether there is a difference between open and closed divertors will briefly be addressed.

The database contains the parameter TAUTH2 which represents the thermal confinement determined by MHD. This confinement definition uses a thermal stored energy computed from $W-W_f$ and an input power corrected for $\dot{W}$ and power lost via fast ion charge exchange and unconfined orbits (PFLOSS). Three machines (JET, ASDEX, DIII-D) can not use TAUTH2 either because W_f or PFLOSS is missing or because TAUTH2 is computed with MHD values. For these machines a thermal energy confinement can be estimated by multiplying the total τ_E used in the previous section by $(1 - W_f/W)$ without subtracting out PFLOSS in the denominator, where now the value of W_f (WFFORM) represents each team's best estimate of the fast ion stored energy computed from a formula (typically from Stix [36] or Callen [37]) as opposed to being computed in a full transport analysis. For PBX-M and PDX, the quantity $W_f=3/4W_{f\perp}+3/2W_{f\parallel}$ was subtracted. However the ASDEX data are not included since WFFORM is not entered into the database. The thermal fit is also performed by adding ASDEX diamagnetic τ_E (assuming $\tau_E \sim \tau_{th}$ for ASDEX) with no substantial change in the results. It is difficult to assess the uncertainty in WFFORM, and hence the

thermal confinement time τ_{th}. A minimum uncertainty of 20% is estimated for τ_{th}. Compared to the standard dataset fit, the thermal confinement fit, shown in Table XI, differs most notably with respect to α_B, α_n, and α_κ. There is no strong evidence indicating that a thermal analysis yields totally different results from the analysis with total stored energy. A separate thermal analysis of ELM-free JET and DIII-D data [32] from discharges of similar plasma geometry at constant toroidal field yields approximately the same I_p and P_L scaling as Table XI but a weaker size dependence of $R^{1.48}$.

A comparison of ELM-free and ELMy datasets is also given in Table XI. The ELMy dataset includes both giant (HGELM) and small (HSELM) ELMs. The ELMy dataset yields a weaker current dependence and a stronger dependence on notably the major radius than the ELM-free dataset. Each dataset contains about the same number of observations but with a different mix of machines. The current dependence in the ELMy dataset is substantially weaker than the dependence seen in the ELM-free dataset in full agreement with an earlier investigation at JET [21]. While the ELM-free dataset is more uniformly represented by both large and small radius machines, the range in R for most of the ELMy data is limited, with R between 1.3 and 1.7 m. However, it should be recalled that the ELMy dataset is at least as well-conditioned as the ELM-free dataset, as discussed in section 3. Note, that the sum $\alpha_B + \alpha_I$ is roughly the same in the ELMy and ELM-free case. This curious trade-off between I_p and B_T dependence calls for further investigation. Another factor that may influence the scaling of the ELMy dataset is that no quantitative characterization of ELMs has been made. Therefore the HSELM and HGELM flags may not represent the same type of ELM in each machine.

Finally, because there are two basic types of divertor configurations represented by the six tokamaks the question has been raised whether there is a difference between open and closed divertor H-mode confinement. To address this question a dataset containing only open divertors, JET, DIII-D, JFT2M and PBX-M is analysed. Unfortunately, as mentioned in section 3.4 on collinearity in the data, this dataset is poorly conditioned. In an attempt to overcome this difficulty two fits are performed with a fixed elongation dependence of $\kappa^{0.0}$ and $\kappa^{1.0}$. Both κ dependencies fit the data about equally well. However, with $\kappa^{0.0}$ the PDX data lies above and the ASDEX data lies on the fitted line, and with $\kappa^{1.0}$ the PDX data lies on and the ASDEX data lies below the line. Since the κ dependence is unknown and its functional form

impacts the results of the open versus closed divertor comparison, it is not possible within the present approach to disentangle the κ dependence and the effect of open/closedness of the divertor on the confinement time. The same conclusion was reached in section 3.4.

4.2.4 *Regression on the ELM-free dataset*

Of all the data groups examined the ELM-free dataset appears to be the best candidate for further investigation since it is relatively well conditioned, represents all machines, and does not have the effect of ELMs. Previously it has been mentioned that the standard dataset has a very strong B_T dependence. It is clear from Table XI that the ELM-free τ_E also has a strong dependence on toroidal field. However, it should be remembered that toroidal field scans at fixed parameters in individual devices show a weak or no confinement variation. Therefore, in an effort to bracket the dependence of τ_E on B_T, four different fits to the ELM-free dataset are shown in Table XII. The first entry is a duplicate of the fit shown in Table XI while the next three have the toroidal field dependence fixed at different values. These fixed values of α_B are 0.0 (DIII-D and JFT2M like), 0.30 (JET like), and 0.15 which is the average of the two extremes. There is a statistically significant increase in χ^2 for these cases indicating B_T or perhaps some other parameters yield a fit with less scatter about the fit. However, since the toroidal field dependence has been shown to be weak in individual machines it seems very unlikely that setting α_B equal to zero is the true reason for an increase in χ^2.

The values of α_I, α_B and α_κ in Table XII tend to trade off one another throughout the different cases. However, since no machine individually reports a large value of α_B (with concomitant small errors), it is difficult to have a high degree of confidence in $\alpha_B = 0.69$. Furthermore, it is also difficult to have confidence in α_κ since as the value of α_B is increased the value of α_κ also increases. When α_B is set to a small value, α_I responds by increasing to a value that is observed by individual machines. The second smallest principal component of the ELM-free dataset is $B_T\kappa/R$ (see Table IV) which is consistent with the correlated behaviour of α_B and α_κ.

In the absence of a firmer conclusion on the toroidal field scaling, we set α_B=0.15. In addition, the PDX data, which has a strong dependence on I_p and the compression ratio, has been eliminated from the ELM-free dataset. For

these choices, the resulting ITER90H-P scaling expression for total energy confinement time is (Fig. 14)

$$\tau_E = 0.082\ I_p^{1.02}\ B_T^{0.15}\ P_L^{-0.47}\ A^{0.5}\ R^{1.60}\ \kappa^{-0.19} \qquad (6)$$

with units of sec, MA, MW, and m. The uncertainties in the multiplier and α's are 0.005, 0.02, -, 0.02, -, 0.07, and 0.08 respectively, where '-' indicates that the uncertainty is missing since the exponent was fixed.. Notice that the uncertainty in the κ dependence is large[3]. The density and aspect ratio variables are missing in Eq. (6) because the error in the exponents are larger than the exponents, $.02 \pm .03$ and $-.05 \pm .06$ respectively, and there is no change in the χ^2 of the fit with these variables removed.

4.2.5 *Regression under alternate assumptions*

To show how critically the resulting scaling expression depends on the input data subset and various presuppositions, we now look what happens if we revise some of the assumptions that led to Eq. (6). Specifically, we reconsider a) the choice of WMHD and WDIA for the various tokamaks, b) the inclusion of PDX data, and c) the restrictions on the B_T and A dependence.

With respect to a), we wish to determine a zeroth order approximation to the quantity that is the sum of the thermal energy plus a fixed contribution, W_f/W_{th}, of fast particles. We will make a simple choice between WDIA and WMHD such that all tokamaks are treated roughly equally with respect to beam anisotropy; this leads to using WDIA for parallel injection and WMHD for perpendicular injection. Since only τ_{mhd} is available for PDX and PBX-M, we use τ_{mhd} for DIII-D, PDX, and PBX-M, and τ_{dia} for ASDEX, JET[4], and JFT-2M. This selection criterion is not based on the definition of stored energy that necessarily gives the maximum value for each device.

Combined with the above selection, several additional corrections to the data were made in order to minimize systematic differences among the machine

---

[3]Larger confinement values are obtained on the closed divertor ASDEX experiment (κ=1). The κ dependence has been studied on JFT-2M for limiter H-mode configurations. The enhancement of τ_E was found to be larger with larger κ [44] (see also Fig. 24).

[4]We include JET in this group, as pencil code simulations at JET indicate a high degree of isotropy, and WDIA was considered to be more accurate than WMHD.

datasets. The JFT-2M team considered WMHD during the ohmic phase to be more reliable than WDIA, so for JFT-2M, we take during the H-phase $WDIA_C$=WDIA+($WMHD_{oh}$-$WDIA_{oh}$). It should be noted that the same type of ohmic offset correction was applied to the ASDEX diamagnetic data prior to storing these data in the database. For ASDEX, PABS in the database equals PINJ minus shine-through, charge-exchange, and bad orbit losses, while for the other tokamaks only shine-through is subtracted. Since shine-through is negligible in ASDEX, we take $\tau_{dia,c}=\tau_{dia}$(PABS+POHM-DWDIA)/(PINJ+POHM-DWDIA)[5].

As far as b) goes, despite the dependence on compression ratio, (see discussion in I.6), which might also apply to other tokamaks, the scatter in the PDX data is not very much larger than in some of the other tokamaks (see Table IX), so we left these data in.

Ordinary least squares regression gives for the total standard dataset (n=1239)

$$\tau_E = 0.025\ I_p^{0.75} B_T^{0.6}\ P_L^{-0.55}\ A^{0.48}\ R^{2.09}\ n_e^{0.16} (a/R)^{-0.05}\ \kappa^{0.68} \qquad (7)$$

with an rmse of 13.8%, and for the ELM-free dataset (n=691),

$$\tau_E = 0.026\ I_p^{0.86}\ B_T^{0.6}\ P_L^{-0.57}\ A^{0.53}\ R^{1.83}\ n_e^{0.10}\ (a/R)^{-0.08}\ \kappa^{0.77} \qquad (8)$$

with an rmse of 12.9%, with the variables in the same units as in Eq. (6). The standard errors of the exponents in the ELM-free case are 0.04,0.06,0.02,0.04,0.07,0.05,0.07,0.03, and are similar for the total standard dataset. Plots of the observed fitted values for the ELM-free scaling are presented in Fig. 15. In both the full and the ELM-free regression, there is a marked B_T dependence. Residual analysis suggest that this variation is systematic across machines and is not due to any particular sub-group of shots.

4.2.6 *Summary of power law regression analysis*

[5]These changes will be made in the update (ITERHDB.2) of the present database, scheduled to be released in Nov. 1991.

It is quite clear that the regression results depend to some extent on the chosen subset of data. Some of the differences in the results shown in Table XI may be due to the different physics aspects that each subset of data was attempting to isolate. However, a common trend for all cases studied appears to be that the confinement is most strongly dependent on R and weakly dependent on n and R/a. Furthermore, the confidence in the dependence of confinement on P_L is high since the variation in α_P is small for the cases studied.

Several scaling relations have been given for the standard subset of the ITER H-mode database for a variety of situations. Eqs. (6) and (8) were developed using slightly different parameter definitions and data selection for the ELM-free dataset. These relations predict confinement times of 5.4 and 6.7 sec respectively for an ITER design point of I_p=22 MA, B_T=4.85 T, n_e=1.24x10^{20} m^{-3}, 160 MW (heating + fusion) power, A=2.5 AMU, R=6 m, a=2.15 m, and κ=2.2. The difference between the two predictions may be related to the difficulty in determining some of the regression coefficients. The dependence on B_T remains a point of concern, as does the dependence on atomic mass and elongation. In addition, it is also plausible to expect that there are other parameters not included in the above scaling expressions that influence confinement time. One such candidate for this is the open/closedness of the divertor, as quantified for PDX by the ratio of the D_α signal in the divertor to that in the midplane. Further work investigating this issue has been started. More sophisticated statistical methods may be applied to refine, and possibly correct at some points, the present approach. However, in view of the issues discussed above, it would be most useful to improve the empirical basis of the present H-mode dataset, especially by 1) extensive B_T scans, 2) low kappa experiments in open divertor devices, 3) more extensive isotope experiments, and 4) a more quantitative classification of ELM behavior. Furthermore, a careful scrutiny into the reasons for conflicting results between particular single parameter scans and analyses of larger databases is indicated.

4.3 Power law scaling expressed in dimensionless physics variables

In this section it is examined whether the thermal energy confinement data satisfy the constraints imposed by plasma physics theory. These constraints were first derived by Kadomtsev [38] and then by Connor and Taylor [39]. If the transport physics is described by the quasi-neutral high-β Fokker-Planck equation, and the dependence on profile scale lengths can be neglected, then

the invariance properties of the basic equations demand that the thermal energy confinement time τ_{th} should be expressible in the form [38]

$$\tau_{th} = \tau_B \, F(\rho/a, \nu^*, \beta, q_{cyl}, \kappa, \varepsilon, A) \qquad (9)$$

where τ_B is the Bohm time, ρ/a the normalised larmor radius, β the plasma beta, ε inverse aspect ratio, κ plasma elongation, q_{cyl} cylindrical safety factor and $A = 1/2\,(A_{gas} + A_{beam})$ the plasma ion mass number. The parameters which are not directly available in the database are expressed as in reference [40] in terms of available averages as follows:

$$\tau_B = \frac{9\mu_0 e \pi}{4} \frac{a^4 n I_p \kappa}{\varepsilon P_L \tau_{th}}, \quad \rho^* = \rho/a = \frac{2\pi}{\mu_0} \left(\frac{\varepsilon P_L \tau_{th} A}{a^3 n I_p^2 \kappa} \right)^{1/2}$$

$$\nu^* = 3\sqrt{2}\pi^{5/2} e^4 \frac{\log \Lambda_{ei}}{\varepsilon_0^2} \frac{a^7 n^3 \kappa^2}{\varepsilon^3 P_L^2 \tau_{th}^2}, \quad \beta = \frac{8}{3\mu_0} \frac{\varepsilon P_L \tau_{th}}{a I_p^2} \qquad (10)$$

$$\varepsilon = \frac{a}{R}, \quad \kappa = \frac{b}{a}, \quad q_{cyl} = \frac{2\pi}{\mu_0} \frac{\varepsilon a \kappa B_T}{I_p}$$

4.3.1 *Regression model*

The model used for τ_{th} in the analysis is of the power law type

$$\tau_{model} = \tau_B^{x1} (\rho/a)^{x2} \nu^{*x3} \beta^{x4} \varepsilon^{x5} \kappa^{x6} q_{cyl}^{x7} A^{x8} \qquad (11)$$

where x1 - x8 are to be estimated. Because τ_B, ρ/a, ν^* and β themselves depend on τ_{th}, ordinary least squares regression applied directly to the variables in Eq. (11) would give misleading results. An easy way around this problem is to introduce 4 variables $\tilde{\tau}_B$, $\tilde{\rho}/a$, $\tilde{\nu}^*$, and $\tilde{\beta}$ defined as in Eq. (10) but with τ_{th} left out. Using natural logarithms on all the variables the regression model becomes linear and the power law expression with the 4 new variables plus A, ε, κ, and q_{cyl} is just a simple linear transformation of the regressor

variables used in section 4.2 Eq. (5). Hence, by ordinary least squares, we estimate $\tilde{x}1$, $\tilde{x}2$,... Then, the theoretical linear restrictions on x1, x2,... can be translated into a linear restriction on $\tilde{x}1$, $\tilde{x}2$,... (or equivalently, linear restrictions on α_I, α_B,...). In practice, the theoretical constraints are tested by restricted least squares of τ_{th} on the engineering variables, I, B,... (or on the auxiliary variables $\tilde{\tau}_B$, $\tilde{\rho}$ /a, ...). Before proceeding with the regression, all variables are standardised which implies that the constant (or intercept) drops out as a fitting parameter.

4.3.2 *Collinearity in data*

A thermal confinement time τ_{th} and the variables in Eq. (10) and those described in section 4.3.1 have been established for the standard dataset.

This data yield an intrinsic relation between minor radius a and A (small machines-hydrogen, large machines-deuterium). The result is that the A scaling is not well established. The dependence upon collisionality and beta is difficult to determine as is the dependence upon Larmor radius because of collinearity in the ITER H-mode data between the corresponding regressor variables. Figures 16 and 17 show plot of these variables. The spread of the data in the log $\tilde{\beta}$, log $\tilde{\nu}*$ - plane (Fig. 17) is larger than that in the log $\tilde{\rho}$/a, log $\tilde{\beta}$ - plane (Fig. 16) The approximate relations

$$\log \tilde{\rho}/a \sim 0.8 \log \tilde{\beta} \ , \ \log \tilde{\beta} \sim -0.8 \log \tilde{\nu}* \qquad (12)$$

imply that trade offs between values x2, x3, and x4 (Table XIV) can be made if a certain theoretical model is desired as fit to the data. It should be remarked however that the full width of the worst principal direction in Table XIV is $\pm$ 0.6 which is still rather large with respect to the measurement error in that direction.

4.3.3 *Results from regression analysis*

Tables XIII and XIV summarise the results from an extensive series of analyses. Five theoretical models for thermal transport are considered and the results from these are compared with an unconstrained model which naturally yields

the smallest root mean square error σ (or rmse). The latter is defined as the square root of

$$\sigma^2 = \frac{1}{N-8+M} \sum_{j=1}^{N} (\log \tau - \log \tau_{model})_j^2 \qquad (13)$$

where N is the number of observations and M the number of restrictions imposed by the theoretical model in question.

The σ's obtained by fits to τ_{mhd}, τ_{dia} as well as τ_{th} derived from MHD and diamagnetic data are listed in Table XIII. The values of Table XIII show by statistical arguments, i.e. σ and δσ, that the theoretical models consistent with the data are the high-β collisional and gyro-bohm models. For example τ_{th} derived from diamagnetic data in the ELM-free dataset (693 obs.) can be represented by the dimensionally correct scaling form which satisfies the high-β Fokker-Planck constraint of Kadomtsev and that of the short wavelength gyro-kinetic scaling (see Table XIV)

$$\tau_{th} = 4.75 \times 10^{-7}\ \tau_B (\rho/a)^{-1}\ \nu^{*-0.15}\ \beta^{-1.30}\ \varepsilon^{-5.58}\ \kappa^{-0.53}\ q_{cyl}^{1.77}\ A^{1.29} \qquad (14a)$$

with τ_B in seconds. The equivalent form in engineering variables is

$$\tau_{th} = 0.036\ a^{2.15}\ n^{0.3}\ I_p^{0.81}\ P_L^{-0.71}\ \varepsilon^{-1.75}\ \kappa^{0.76}\ B_T^{0.50}\ A^{0.36} \qquad (14b)$$

with units of sec, m, 10^{19} m^{-3}, MA, MW and Tesla.

The thermal confinement time range for ITER predicted by the scalings in Table XIV is [41]

$$4.23\ s < \tau_{ITER} < 4.95\ s.$$

4.4 Offset Linear Scaling for H-mode Confinement

An offset linear scaling for the thermal energy content W_{th} is determined for the D-shaped open divertor tokamaks DIII-D, JET and JFT2M. The predictions for the bean shaped open divertor tokamak PBX-M and the closed divertor tokamaks ASDEX and PDX are compared with the actual observations on these machines.

The analysis is performed on the dataset described in section 2.2 with the following definitions of W_{th} for the different machines:
W_{th} = WMHD - 1.5 × WFFORM × (1 - 0.5 × WFANI) for DIII-D (WFFORM = 0 assumed when missing), JFT2M, PBX-M and PDX;
W_{th} = WDIA - 1.5 × WFFORM × WFANI for ASDEX and JET.

The power dependence of W_{th} is depicted in Fig. 18 for the D-shaped open divertor tokamaks. It is seen that the data can be described well with the offset linear form

$$W_{th} = W_o + \tau_{inc}\, P \qquad (15)$$

where $P = P_{abs} + P_{ohm} - \dot{W} - P_{floss}$, with P_{floss} being power lost via fast ion charge exchange and unconfined orbits (PFLOSS).

4.4.1 *Incremental confinement time*

The scaling of the incremental confinement time τ_{inc} is established first by determining the dependence on I_p, n, B_T and A from JFT2M [42] data alone. The size or R dependence is then obtained under that assumption from the three machines data combined.

The current dependence of τ_{inc} for the JFT2M data is shown in Fig. 19a. Up to currents of 250 kA (i.e. $q_{95} > 2.7$), a linear I_p dependence of τ_{inc} is seen. There is a considerable collinearity between n and I_p and the dependence of τ_{inc} on the magnetic field is weak in the JFT2M data, at least for $q_{95} > 2.7$. Therefore only I_p is kept as a scaling variable. The result of the analysis is that the JFT2M scaling for τ_{inc} can be written as

$$\tau_{inc} \propto I_p\sqrt{A} \qquad (16)$$

It is assumed that Eq. (16) is valid for DIII-D and JET, (see Figs. 19 b-c) and that the remaining variation in τ_{inc} is due to a dependence on R the geometrical major radius. Under these assumptions the R dependence is as shown in Fig. 20. Combining this result with Eq. (16) the scaling of τ_{inc} for the D-shaped divertor tokamaks is

$$\tau_{inc} = 2.9\text{x}10^{-8}\ I_p^{1.0}\ R^{0.87}\ \sqrt{A} \qquad (17)$$

in MKS units. It is noted that the uncertainty in the R dependence is increased if the JET data with negative or missing values of SEPLIM are included (see section 2.2).

4.4.2 *Offset part of the energy*

The offset part of the thermal energy is defined by

$$W_o = W_{th} - \tau_{inc}\ P \qquad (18)$$

The scaling of W_o is determined in 2 steps. First the dependences on I_p and B_T are established. Then as before a scaling with R is obtained with these dependences fixed.

In Fig. 21 the dependence of W_o on I_p for fixed B_T in JFT2M, JET and DIII-D is shown. Notice the dependence is almost linear. Similarly the dependence on B_T for fixed I_p is shown in Fig. 22 for the 3 machines. In the ohmic discharges on JFT2M it is found that $W \propto I_p\ B_T$. Assuming $W_o \propto I_p^{\alpha_I}\ B_T^{\alpha_B}$ it is found that α_I varies from 0.77 to 1.43 and α_B from 0.56 to 1.0 for the three tokamaks. In order to proceed to the next step in the analysis the averages of the exponents are chosen i.e. it is assumed that

$$W_0 \propto I_p^{1.1} B_T^{0.91} \qquad (19)$$

Under this assumption the remaining variation in W_o is shown against R in Fig. 23. Adding this R-dependence to Eq. (19) the following scaling for the offset part of the energy is obtained

$$W_o = 0.0046\ R^{1.9}\ I_p^{1.1}\ B_T^{0.91}\ \sqrt{A} \qquad (20)$$

4.4.3 *Offset linear scaling*

Combining the results of Eqs. (17) and (20) leads to the following offset linear scaling (ITER90H-O) of the thermal energy for H-mode

$$W_{th} = 0.0046\ R^{1.9}\ I_p^{1.1}\ B_T^{0.91}\ \sqrt{A} + 2.9 \times 10^{-8}\ I_p^{1.0}\ R^{0.87} \sqrt{A}\ P \qquad (21)$$

Figure 24(a) illustrates the scaling expression with the H-mode data from the open divertor tokamaks. The root mean square error is 14.5% for this figure. The scaling expression Eq. (21) is also compared with the data from other configurations. Figure 24 compares Eq. (21) with the results in ASDEX, DIII-D, JET, JFT2M, PBX-M and PDX.

The PBX-M data, which have an elongation of 1.6 and indentation of 0.15, fit well. Only a few points of the PDX data fit this scaling. These points are characterized by a large value of DALFDV/DALFMP and $\kappa = 1$. Data from ASDEX ($\kappa = 1$) show slightly better values compared to Eq. (21). These observations suggest that the offset linear scaling Eq. (21) should include a dependence on κ and divertor type (open or closed). Figure 25 illustrates the distribution of the enhancement factor in ASDEX, DIII-D and JFT2M. The abscissa is τ_E normalized to the ITER89-P L-mode scaling expression. ASDEX has clearly a larger enhancement factor and these three devices have similar major radii.

It can hypothesized that the improvement is larger in tokamaks with closed divertor than in those with open divertor. It has been found on PDX that a change to the neutral pressure in the main chamber can lead to factor of two difference in τ_E [43]. Thus the conductance of the divertor throat affects the confinement time. This has also been shown in ASDEX [24, 25].

The dependence of the enhancement factor on the configuration may be more clearly seen in the case of the limiter H-mode. In the case of the limiter H-mode (such as in JFT2M [44], JT-60 [12] or JIPP-TIIU [14]), the L/H-transition is as clear as those in divertor plasma, but the enhancement of τ_E is smaller. Though the quantitative study on the dependence of τ_E on the configuration is not completed, the comparison of the results in closed divertor, open divertor and limiter suggests the importance of the configuration on the enhancement of the energy confinement time.

5. SUMMARY

This report and its appendices contain essential information for potential users of the ITER H-mode database.

A preliminary analysis of the database has been presented. It has been found that the ELM-free data is well conditioned for predicting the confinement time in ITER, however there are difficulties in predicting the ITER confinement time with ELMy data due to the sparsity of high quality JET ELMy data.

Several scaling expressions have been given for the ELM-free and ELMy data under a variety of different assumptions and data subsets. The power law forms (Eqs. 6 and 8) yield predicted global confinement times for ITER of 5.4 and 6.7 sec respectively. The estimated thermal confinement data have been shown to satisfy to a high degree the high-β collisional constraint of Kadomtsev as well as the short wavelength turbulence constraint. The predicted confinement time for this power law scaling is ≈4.5 sec. Finally, the offset linear form describing the thermal stored energy predicts an ITER confinement time of 6.2 sec. All scalings are open to further improvement by future investigations.

REFERENCES

[1] KAYE, S.M. GOLDSTON, R.J., Nucl. Fusion **25** (1985) 65.

[2] KAYE, S.M., BARNES, C.W., BELL, M.G., et al., Status of Global Energy Confinement Studies, Rep. PPPL-2670, Princeton Plasma Physics Laboratory, Princeton, NJ (1990), to be published in Phys. Fluids.

[3] CORDEY, J.G., DEBOO, J., KARDAUN, O., et al., Plasma Physics and Controlled Nuclear Fusion Research 1990 (Proc. 13th Int. Conf. Washington, 1990) IAEA-CN-53 IF-3-19.

[4] STRACHAN, J.D., BITTER, M., RAMSEY, A.T., et al., Phys. Rev. Lett. **58** (1987) 1004.

[5] JET Team, in Plasma Physics and Controlled Nuclear Fusion Research 1988 (Proc. 12th Int. Conf. Nice, 1988), Vol. 1, IAEA, Vienna (1989) 215.

[6] WAGNER, F., BECKER, G., BEHRINGER, K., et al., Phys. Rev. Lett. **49** (1982) 1408.

[7] OSBORNE, T.H., BROOKS, N., BURRELL, K.H., et al., Nucl. Fusion **30** (1990) 1023.

[8] LOHR, J.M., STALLARD, B.W., PRATER, R., et al., Phys. Rev. Lett, **60** (1988) 2630.

[9] STEINMETZ, K., NOTERDAEME, J.-M., WAGNER, F., et al., Phys. Rev. Lett. **58** (1987) 124.

[10] MATSUMOTO, H., OGAWA, T., TAMAI, H., et al., Nucl. Fusion **27** (1987) 1181.

[11] TUBBING, B., JACQUINOT, J., STOCK, D., TANGA, A., Nucl. Fusion **29** (1989) 1953.

[12] TSUJI, S., USHIGUSA, K., IKEDA, Y., et al., Phys. Rev. Lett. **64** (1990) 1023.

[13] ODAJIMA, K., FUNAHASHI, A., HOSHINO, K., et al., Plasma Physics and Controlled Nuclear Fusion Research 1986 (Proc. 11th Int. Conf. Kyoto, 1986), Vol. I, IAEA, Vienna (1987) 151.

[14] TOI, K., KAWAHATA, K., MORITA, S., et al., Phys. Rev. Lett. **64** (1990) 1895.

[15] BUSH, C.E., GOLDSTON, R.J., SCOTT, S.D., et al., Phys. Rev. Lett. **65** (1990) 424.

[16] Contacts at

ASDEX: O. KARDAUN - Max-Planck Institut für Plasmaphysik
DIII-D: J. DEBOO - General Atomics
JET: K. THOMSEN - JET Joint Undertaking
JFT2M: Y. MIURA - JAERI
PBX-M/PDX: S.M. KAYE - Plasma Physics Princeton Laboratory

[17] BHATNAGAR, V.P., CORDEY, J.G., JACQUINOT, J., START, D.F.H., Plasma Physics and Controlled Fusion **31** (1989) 333.

[18] BURRELL, K.H., ALLEN, S.L., BRAMSON, G., et al., Plasma Physics and Controlled Fusion **31** (1989) 1649.

[19] FULLER, W.A., Measurement Error Models, John Wiley and Sons, Inc., New York (1987).

[20] HILLEGERS, L.T.M.E., The estimation of parameters in functional relationship models, PhD Thesis, Technical University of Eindhoven, Eindhoven (1986).

[21] KARDAUN, O., THOMSEN, K., CHRISTIANSEN, J.P., et al., in Controlled Fusion and Plasma Physics (Proc. 16th Eur. Conf. Venice, 1989), Vol. 13B, Part I, European Physical Society (1989) 253.

[22] SCHISSEL, D.P., BROOKS, N., BURRELL, K.H., et al., in Controlled Fusion and Plasma Physics (Proc. 16th Eur. Conf. Venice, 1989), Vol. 13B, Part I, European Physical Society (1989) 115.

[23] KARDAUN, O., THOMSEN, K., CORDEY, J.G., WAGNER, F., et al., in Controlled Fusion and Plasma Heating (Proc. 17th Eur. Conf. Amsterdam, 1990), Vol. 14B, Part I, European Physical Society (1990) 110.

[24] ASDEX Team, Nucl. Fusion **24** (1989) 1959.

[25] RYTER, F., GRUBER, O., VOLLMER, O., WAGNER, F., in Controlled Fusion and Plasma Heating (Proc. 17th Eur. Conf. Amsterdam, 1990), Vol. 14B, Part I, European Physical Society (1990) 94.

[26] BELL, R.E., ASAKURA, N., BERNEBET, S., CHANCE, M.S., DUPERREX, P.-A., et al., Phys. Fluids B **2** (1990) 1271.

[27] KAYE, S.M., BELL, M.G., BOL, K., BOYD, D., BRAU, K., et al., J. Nuclear Mat. **121** (1984) 115.

[28] GOLDSTON, R.J., Plasma Phys. Controll. Fusion **26** (1984) 87.

[29] YUSHMANOV, P.N., TAKIZUKA, T., RIEDEL, K.S., et al., Nucl. Fusion **30** (1990) 1999.

[30] REBUT, P.H., BRUSATI, M., HUGON, M., LALLIA, P., in Plasma Physics and Controlled Nuclear Fusion Research 1986 (Proc. 11th Int. Conf. Kyoto, 1986), Vol. 2, IAEA, Vienna (1987) 187.

REBUT, P.H., LALLIA, P.P., WATKINS, M.L., in Plasma Physics and Controlled Nuclear Fusion Research 1988 (Proc. 12th Int. Conf. Nice, 1988), Vol. 2, IAEA, Vienna (1989) 191.

[31] JET Team, in Plasma Physics and Controlled Nuclear Fusion Research 1988 (Proc. 12 Int. Conf. Nice, 1988), Vol 1, IAEA, Vienna (1989) 159.

[32] SCHISSEL, D.P., DEBOO, J.C., BURRELL, K.H., et al., H-Mode Energy Confinement Scaling from the DIII-D and JET Tokamaks, Rep. GA-A19925, General Atomics, San Diego, CA (1990), Rep. JET-P (90) 16, JET Joint Undertaking, Abingdon, Oxfordshire (1990), accepted for publication in Nucl. Fusion.

[33] SCHISSEL, D.P., BURRELL, K.H., DEBOO, J.C., et al., Nucl. Fusion **29** (1989) 185.

[34] SUZUKI, N., MIURA, Y., HASEGAWA, M., HOSHINO, K., KASAI, S., et al, in Controlled Fusion and Plasma Physics (Proc. 14th Eur Conf. Madrid, 1987), Vol. 11D, Part II, European Physical Society (1987) 217.

[35] WAGNER, F., BESSENROTH-WEBERPALS, M., FAHRBACH, H.U., et al., in Controlled Fusion and Plasma Physics (Proc. 16th Eur. Conf. Venice, 1989), Vol. 13 B, Part I, European Physical Society (1989) 195.

[36] STIX, T.H., Plasma Phys. **14** (1972) 367.

[37] CALLEN, J.D., COLCHIN, R.J., FOWLER, R.H., et al., in Plasma Physics and Controlled Nuclear Fusion Research 1974 (Proc. 5th Int. Conf. Tokyo, 1974), Vol. 1, IAEA, Vienna (1975) 645.

[38] KADOMTSEV, B.B., Soviet J. Plasma Physics **1** (1975) 295.

[39] CONNOR, J.W., TAYLOR, J.B., Nucl. Fusion **17** (1977) 1047.

[40] CHRISTIANSEN, J.P., CORDEY, J.G., THOMSEN K., Nucl. Fusion **30** (1990) 1183.

[41] CHRISTIANSEN, J.P., CORDEY, J.G., KARDAUN, O., THOMSEN, K., Application of plasma physics constraints to confinement data, submitted to Nucl. Fusion, 1991.

[42] SUZUKI, N., AIKAWA, A., HOSHINO, K., et al., in Plasma Physics and Controlled Nuclear Fusion Research 1988 (Proc. 12th Int. Conf. Nice, 1988) Vol. 1, IAEA, Vienna (1989) 207.

[43] FONCK, R.J., BEIRSDORFER, P., BELL, M., et al., Proc. 4th Int. Symp. on Heating in Toroidal Plasmas, Rome, March 21-28, 1984, Vol. 1, 37.

[44] MATSUMOTO, H., FUNAHASHI, A., HASEGAWA, M., et al., in Controlled Fusion and Plasma Physics (Proc. 14th Eur. Conf. Madrid, 1987), Vol. 11D, Part I, European Physical Society (1987) 5.

APPENDIX I - DATA FEATURES

I.1 ASDEX data

The ASDEX contribution to the ITER database consists of 1071 timeslices from 153 discharges. For each shot, 7 timeslices are provided: 3 ohmic, 1 L-mode and 3 H-mode points. The three ohmic points are stationary. The third H-mode point in each shot is chosen at maximal W, such that $\dot{W}$= 0 (no abrupt drop in W). $\dot{W}$ has been determined from a parabolic fit of the three available H-mode points (DWHC=0), or, 'set by hand' from drawing the right or left tangent to the WDIA time trace (DWHC=1). In a number of cases, the value of WDIA was influenced by the choice of PHASE (with or without ELMs). For the ohmic points and the third H-mode point in each discharge, $\dot{W}$ has been set to zero. The ELM-free period usually being very short, all available H-mode time points, except for a few, are during the ELMy phase.

All shots are tangentially injected NB shots $H^0 \rightarrow D^+$ with the beams parallel to the direction of the current (co-injection) from 2 main operating periods: (1) 1982-1984: Before the introduction of the ICRH antenna. (2) 1985-1986: After the introduction of the ICRH antenna, but before the hardening of the vessel. During both operating periods, a closed, low by-pass divertor (DV I) has been in use.

For all shots the radiated power at the stationary H-point it less than 30% of the injected power. The offset in β_{dia} has been corrected for by constraining β_{dia} to be

equal to β_{mhd} during the ohmic phase. During the H-mode, β_{mhd} has been determined by subtracting the slightly larger (but better known) value of $l_i/2$ during th eohmic phase from the signal that measures $\beta_{mhd} + l_i/2$.

The ranges of the most important plasma parameters are as follows:

$0.2\ MA < I_p\ [MA] < 0.45$, $1.6T < B_T\ [T] < 2.6$, $1.0 < P_{inj}\ [MW] < 3.6$,
$1.9 < \approx \overline{n}\ [10^{19}\ m^{-3}] < 9.3$, $0.13 < n_{ohm}\ [10^{19}\ m^{-3}] < 5$, $2.2 < q_{cyl} < 5.8$.

Ten shots are with carbonised walls. All shots are divertor discharges, about half of them double null.

I.2 DIII-D data

The DIII-D contribution to the ITER H-mode database consists of 152 time slices taken from 121 discharges. All discharges are single-null divertor discharges with the X-point located at the bottom of the vessel, in the direction of $\nabla B \times B$. Nearly all discharges are taken from the 1989 operating period with fixed vessel wall armor of graphite tiles covering the top, inside, and bottom of the inconel vessel walls. The data are collected from experimental run days where systematic parameter scans have been performed for studying various aspects of H-mode confinement in DIII-D.

Almost all of the data is with deuterium neutral beam injection into deuterium plasmas. There are 13 time slices included with hydrogen neutral beam injection into hydrogen plasmas so that a dependence of confinement on mass can be addressed. Cases with mixed species, $H^0 \rightarrow D^+$ or $D^0 \rightarrow H^+$, are not included in order to avoid confusion because the mix of species is not well known. Three examples of ohmically heated divertor discharges during L-mode phase are also included in the DIII-D database.

The data cover wide ranges in global parameters with $0.6 < I_p$ [MA] < 2.5, $1 < P_{abs}$ [MW] < 11, $1.4 < B_T$ [T] < 2.2, $3 < \bar{n}$ [10^{19} m^{-3}] < 13 and $1.7 < \kappa < 2.1$ where P_{abs} is the neutral beam power absorbed in the plasma and κ is the plasma elongation at the separatrix surface. The database includes values of q_{95} down to three. Values below three are omitted because confinement deteriorates in that region and the responsible mechanism(s) are as yet not understood. The data cover a wide range in toroidal beta up to normalized values of 2.9, $\beta_{norm} = \beta$ [%] a[m] B_T [T]/I [MA]. As the beta limit is approaching, near $\beta_{norm} = 3.5$ for most cases in DIII-D, large amplitude coherent and incoherent MHD activity is sometimes observed. This MHD activity can result in an observable confinement deterioration so any high beta discharges exhibiting significant MHD activity are not included in the database.

The ohmic power given in the database is determined from the plasma resistivity assuming the electric field is constant across the plasma. An estimate of the volume averaged electron temperature is obtained from the MHD value of total stored energy assuming a dilution factor of one and Z_{eff} is determined from central chord visible Bremsstrahlung measurements. When calculated this way, the ohmic power does not show significant variation due to transient events such as the addition of neutral beam power or change in I_p. This is often the case when P_{ohm} is determined from a measurement of the plasma loop voltage with an attempt to compute and remove inductive effects.

In general the data taken at a specific time slice are not averaged in time, with the exception of MHD data determined from an equilibrium MHD code. Magnetic probe information required as input to the MHD code is averaged over ± 5 ms.

The majority of the data included in the database are taken from times of giant ELM activity, which are also usually during a steady state period with respect to stored energy and plasma density. During this phase of the H-mode, the fast ion fraction of the total stored energy is usually small, 15% or less, particularly at high current where the density is large and the slowing-down time short. Some timeslices are taken from the ELM-free period of a discharge, which is typically after the L- to H-mode transition but before the first giant ELM. During this period, the plasma density is still evolving from the ohmic level which is typically well below, factor of two for high current, the final equilibrium level, and the time derivative of stored energy is an important term in the computation of confinement time. During the ELM-free period, fast ions can become more significant due to the longer slowing down times associated with lower density levels. At low current and high beam power, $I_p \leq 0.8$ MA and $P_{abs} \geq 7$ MW, the fast ions can account for 50% of the total stored energy during the ELM-free period. Accordingly, it is more appropriate to consider the thermal energy confinement time for most ELM-free timeslices. Only at high current levels does the stored energy reach a maximum and then decrease during the ELM-free phase of the discharge due to an increase in radiation levels associated with increased density levels during long ELM-free periods. In these cases, the fast ion energy content is again a small fraction of the total.

I.3 JET data

The JET contribution to the ITER H-mode database consists of 1171 time slices from 171 discharges There are 113 timeslices from 16 double-null divertor discharges and 1048 time slices from 155 single-null divertor discharges with the X-point located at the top of the vessel, in the direction of the ion grad-B drift. For each discharge 3 ohmic reference points are given which amounts to 513 of the 1171 time slices. The discharges have been selected from the period 1986-1988. In 1986 only single-null H-modes have been produced with no X-point tiles present in the vessel; the inner wall was covered by Carbon and single outboard carbon limiters together with 3 carbon framed ICRH antennae were present on the low field side. In 1987 carbon belt limiters, 8 ICRH antennae and carbon X-point tiles were installed. Only a few discharges have been included from this initial period with belt limiters. The main

selection of discharges is from the 1988 operating period where the inside of the vessel was the same as in 1987 but with improved boundary conditions due discharge conditioning of the interior.

All of the H-mode data is with deuterium neutral beam injection into deuterium plasmas. The data cover wide ranges in global parameters with $2 < I_P$ [MA] < 5.2, $3.1 < P_{abs}$ [MW] < 17.9, $1.8 < B_T$ [T] < 3.7, $1.65 < \bar{n}$ [10^{19} m^{-3}] < 6.7 and $1.7 < \kappa < 1.9$. The range in q_{95} is 2.8-6.3 and no real evidence for confinement degradation has been observed. The data with $q_{95} \approx 3$ are obtained in 5MA discharges and the confinement in these discharges is lower than expected.

The ohmic power given in the database is very uncertain during NBI. In future releases better estimates calculated using the DIII-D approach may be provided.

In general the data taken at a specific time slice is averaged over ± 0.1 sec in time. The majority of the H-mode data included in the database is at times without ELM activity. The characteristics of the JET ELM-free H-mode is that radiation density and energy keep increasing until the return of the L-mode phase. However, at least one timeslice per discharge with $\dot{W}/P_T \leq .3$ is included. Mostly grassy ELM's are observed on JET. In the database 105 timeslices are from H-modes with grassy ELM's and only 21 timeslices from H-modes with giant ELM'S. The observed giant ELM's are not as regular as on other machines. Using a Fokker-Planck solver to estimate the fast ion energy content W_f it turns out that, to a good approximation, $W_f \propto P_{NB}/\langle n \rangle$, and that for low density discharges the fast ion energy content can be a substantial fraction of the total energy.

I.4 JFT2M data

JFT2M data in the ITER H-mode database consists of 654 timeslices from 218 discharges. For each discharge, 3 time slices (ohmic, $\dot{W} > 0$ and $\dot{W} \approx 0$) are provided. Most shots are examples of the typical ELM-free H-mode in JFT2M, except for a few shots near the threshold power. The majority of discharges are open single-null divertor discharges with the ion grad B drift direction towards the X-point and they include scanning shots on throat length and minor radius. Only 7 shots with double-null divertor configuration are included for comparison.

The discharges have been selected from experiments between 1985 and 1989. The machine conditions are a little different for shots before July 1987 compared to the

conditions for shots after that time. The main changes are that the inside wall surface of stainless steel has been covered with carbon tiles to reduce metallic impurities, and the composition of neutral beam ion source has been changed from one duopigatron type and one bucket type to two bucket types to increase input power and also to improve the proton ratio from 60% to 80%.

Only data on hydrogen neutral beam injected into hydrogen plasma and deuterium plasma are included. In the case of deuterium plasma the dilution by hydrogen beam reaches roughly 50%. Power scanning data from co-injection, counter-injection and balanced-injection, as well as data for two ion source types and beam energy scanning are included for comparison. The best data have been obtained for the co-injection with duopigatron source.

The highest stored energy has been obtained by pellet injection. Therefore 4 shots with hydrogen pellet injection into hydrogen plasma (20% better) and 3 shots with deuterium pellet injection into deuterium plasma (30% better) are included for comparison with gas puffing.

The parameter ranges are as follows: $0.116 < I_p[MA] < 0.291$, $0.78 < B_T[T] < 1.4$, $1.0 < \overline{n}\,[10^{19}\ m^{-3}] < 8.6$, $1.28 < \kappa < 1.5$, $0.2 < P_{abs}\,[MW] < 1.6$ and $2.2 < q_{95} < 5.5$. The safety factor q_{95} is calculated with an equilibrium code; however, it is about 10% lower than the surface safety factor defined on a magnetic surface 5 mm inside the plasma, which is a good variable to represent MHD activity in JFT2M. This means that the degradation due to low q operation seems to begin at $q_{95} \lesssim 2.7$ in the JFT2M data. Variables evaluated from magnetic measurements are averaged over 5 ms to cancel noise (600 Hz) from thyristor power supplies. The diamagnetic energy W_{dia} have been corrected with density scan data in the ohmic phase such that the absolute error in W_{dia} is within 1-2 kJ. P_{ohm} is simply calculated as $V_{surf} \times I_P$, so it is not corrected for the inductive part due to changes in l_i. But the estimated error in P_{ohm} may be less than 20% at the selected times. P_{rad} inside the separatrix also has a 20% error, because intense radiation around the X-point makes it difficult to separate the inside P_{rad} from the outside P_{rad}. The beam power into the torus is measured with a 2 dimensional calorimeter array and power losses are estimated from an approximate formula which is made from results calculated with a Monte Carlo code for various parameters corresponding to the JFT2M operational range. The uncertainty in absorbed power P_{abs} is less than 10%, however, the uncertainty in loss power P_{floss} (CX loss and orbit loss) and fast ion energy WFFORM may be about 20%. The fast ion

contribution to total energy content in almost all discharges is about 10%, except at low density.

I.5 PBX-M data

The PBX-M dataset consists of 264 timeslices from 156 discharges. Both steady-state ($|\dot{W}| \leq 0.1\ P_T$) and non-steady-state ($|\dot{W}| = 0.1\text{-}0.3\ P_T$) discharges are provided. The H-mode discharges in this dataset are taken from runs in late March and early October 1989 in a double-null, open divertor configuration. All discharges have deuterium injected into deuterium with variable mixtures of perpendicular ($R_{tan} = 0.348$ m) and tangential ($R_{tan} = 1.30$ m) beams into plasmas with $R_0 \sim 1.65$ m and $a_{mid} \sim 0.28$ m. The geometry of PBX-M is such as to present a high aspect ratio ($R/a \approx 5.5$) device. The H-mode discharges cover a fairly narrow region of operating space, with $0.28 < I_p$ [MA] < 0.38, $1.3 < B_T$ [T] < 1.43, $2 < \overline{n}$ [10^{19} m^{-3}] < 9, and $1.5 < P_{abs} + P_{ohm}$ [MW] < 5.3 (in some cases, $P_{ohm}<0$). The latter two parameters, density and heating power, exhibit a strong positive correlation. The PBX-M plasmas are slightly indented, 15% on the outer flux surface, and the indentation is > 0 only on the outer several flux surfaces. The elongation of these plasmas is ~ 1.6.

The PBX-M dataset exhibit distinct groupings of data. The discharges with giant ELMs, typically occur at high power and they have degraded confinement. The H and HSELM discharges, however, exhibit comparable confinement trends and values. The second grouping is delineated by $q_{95} = 4$. The $q_{95} < 4$ discharges exhibit a strong degradation of confinement time with power, going as $\tau_E \propto P^{-0.7}$ with power and density being correlated.

Above $q_{95} = 4$, the confinement time degradation with power is less fierce, with $\tau_E \propto P^{-0.25}$. In both regimes only density and power vary enough to be used as regressor variables but in both regimes density and power are collinear. Because of the narrow operating regime of PBX-M H-mode plasmas, multi-parameter scalings are very difficult to determine. Nevertheless, the PBX-M dataset can serve nicely as an anchor point for aspect ratio scaling.

I.6 PDX data

The PDX dataset consists of 154 time slices from 154 discharges. The H-mode experiments in PDX have been performed during the year of 1983 in a single-null, closed divertor configuration with the ion grad B drift towards the X-point. In PDX, all

four heating beams have been oriented in a near-perpendicular direction with R_{tan} = 0.348 m (R_0 ~ 1.4m, a ~ 0.4m). Most of the contributed data are with deuterium into deuterium, although there are 44 discharges with hydrogen injected into deuterium plasmas. Operating parameter ranges for these discharges are $0.25 < I_p$ [MA] < 0.45, $1.0 < B_T$ [T] < 2.0, $2.5 < \bar{n}$ [10^{19} m^{-3}] < 10, and $1.5 < P_{abs} + P_{ohm}$ [MW] < 5.5. The discharges are essentially in steady-state.

The relatively wide range of operating parameter space covered in these experiments allows for studying the parametric dependence of the confinement time. In particular, the species dependence can be obtained by comparing H^0 and D^0 injection. The precise mixture of thermal H to D not being known, an effective mass, which is the simple average of the beam and thermal mass species, is assumed.

The parametric dependences of the different types (H, HSELM, HGELM) discharges, are approximately the same.

In addition to the parameter ranges discussed above, the discharges range in q_{95} from 2.5 to 4.0. No degradation of confinement is seen for $q_{95} \leq 3$ in PDX. Plasmas with either hydrogen or deuterium injection exhibit a strong dependence on I_p (increasing in a faster than linear fashion) and both sets exhibit degradation of confinement with heating power. In general, for the same operating parameters, the D^0 injection plasmas have confinement times approximately 40 to 50% higher than those with H^0 injection. However, extreme care must be taken. One of the hidden parameters in the PDX dataset is the parameter defined by the ratio of divertor D_α (div) emissivity to that in the midplane D_α (mp). Larger values of D_α (div)/D_α (mp) can be interpreted as evidence for a more localized recycling in the divertor region. For the D^0 injection, a 75% increase in D_α (div)/D_α (mp) leads to a 40-50% increase in confinement, holding all other parameters fixed. The 40-50% higher confinement in D^0 relative to H^0 plasmas is at comparable values of D_α (div)/D_α(mp), and this improvement translates into an almost linear dependence of confinement on effective mass. The dependence on toroidal field and plasma density is weak, although there is a significant collinearity between I_p and B_T; interdependences among all the other variables are weak. The confinement is seen to degrade strongly with power, going as $P^{-0.7}$.

APPENDIX II - OPERATIONAL PROCEDURES TO OBTAIN GOOD H-MODE CONFINEMENT

II.1 General Comments

In each of the Tokamaks represented in this data base, a set of operating conditions have emerged for which good (high confinement) H-modes are achieved in each machine. These operating procedures may imply correlations in the data which should not be ignored when obtaining scaling relations from the data.

The procedures to obtain good H-mode confinement in each machine can be divided primarily into two categories:

a) Avoid large and frequent Edge Localized Modes (ELMs).
b) Obtain the threshold conditions necessary for the L to H transition.

The operational criteria that are followed to avoid large and frequent ELMs is conveniently divided into 3 groups;

1) Edge fuelling source.
2) Impurity radiation.
3) Plasma position, area of interaction, and X-point location.

These are addressed separately below with the operational procedures developed by each Tokamak group.

II.2 Edge Fuelling

It is widely observed that the H-mode confinement is degraded when the edge fuelling source is excessive, usually by an increase in the ELM frequency and/or the return to L-mode.

ASDEX

Low edge recycling is obtained by operating a closed divertor. Long ELM-free periods are obtained with a closed divertor and after careful positioning of the plasma inside the vessel. With an open divertor, the power required to obtain H-mode increases and only ELMy discharges are obtained.

DIII-D

Low edge low fuelling is obtained via reducing the recycling by baking the torus and conditioning the vessel wall with a ~5 min glow in He before every discharge; by

operating at moderate to low target densities (20 to 50% of the Ohmic limit); and by normally turning off the cold gas fuelling at or before the L-H transition. The lowest target density is limited by non rotating locked modes, and because these are more a problem at high current and low q, these high current and low q discharges have a higher target density. The power threshold also increases approximately linearly with density.

JET

Good H-modes in JET are obtained with target densities approximately $2 \times 10^{19} m^{-3}$ for 3 MA discharges and 3×10^{19} m^{-3} for 4 MA discharges. At lower densities the power threshold begins to increase. With carbon walls the best H-modes occur after helium glow wall conditioning with lower power threshold and lower Zeff.

JFT2M

Titanium gettering is routinely used to reduce the recycling of the working gas. The cold gas fuelling is turned off at the L to H transition. Higher target density provides better results. Central fuelling with pellets in the L-phase results in peaked density H-modes with better confinement. Better confinement with higher target density is believed to be related to the ability to reach higher H-mode density before the confinement degradation caused by impurity accumulation occurs.

PBX-M

Titanium gettering is used to reduce recycling. The gas feed is kept on after the H-transition at a rate of 10-20 Torr- l/sec. Higher gas feed rates have been used to ward off impurity build-up, but this results in increased recycling in the main chamber and thus a degradation in the H-mode confinement.

PDX

Confinement improves as the recycling becomes more localized in the divertor; accomplished by a) gas injection in the divertor region, b) low cold gas fuelling rates (< 10 Torr- l/s) kept constant through the transition, c) using the single null configuration with the ion grad–B drift in the direction of the single null. In addition titanium gettering has typically been employed.

II.3 Impurity radiation

The ELM frequency generally increases with increased low-Z edge radiation. Low Z radiation also increases the threshold power.

ASDEX

Clean plasma conditions lead to better confinement. Plasmas with the highest energy confinement time in ELM-free phases are achieved with boronization, because the detrimental effect of impurity radiation is delayed. Also the longest ELM-free H-mode phases are obtained with boronization. At present the boronized shots as well as discharges with a very regular ELM frequency are not yet included in the data base.

DIII-D

A high level of low Z impurities (primarily oxygen) can prevent the transition to H-mode, in the worse cases even at high input power. Helium glow conditioning between discharges maintains a low and reproducible level of oxygen. The oxygen level is monitored by a residual gas analyzer and if it is high (as perhaps after a severe disruption), the glow is extended to reduce it to a nominally good level.

JET

Nickel concentration of approximately 10^{-3} and/or oxygen and carbon concentrations above $1\text{-}2 \times 10^{-2}$ prevent the H-mode transition. He glow conditioning is used to reduce the low Z impurities and the best discharges follow the He glow.

JFT2M

Titanium gettering is used to reduce radiation due to low-Z impurities.

PBX-M

Titanium gettering is used to reduce radiation due to low Z impurities. Radiation from metallic impurities is reduced by increasing the gas feed rate; however, this has the effect of increasing recycling in the main chamber, and causing confinement to degrade.

PDX

Titanium gettering is used and low Z radiation is normally not a problem. Metallic impurity radiation is reduced by increasing the gas feed rate; as in PBX-M, this has however the effect of increasing recycling in the main chamber, and causing confinement to degrade.

II.4 Plasma Position and X-point position

ASDEX

Best shots are obtained with the plasma displaced outwards toward the outer wall and with the plasma displaced upward slightly to give a single null with the grad B drift toward the dominant null. The X-point position does not vary significantly in ASDEX.

D3D

The distance between the last closed flux surface and the outer limiter is greater than 4-5 cm, to minimize any interaction with the outer limiter. If this distance reaches zero, the H-mode phase terminates. Interaction with the inner limiter seems to degrade confinement only slightly if at all. The distance between X-point and the divertor tiles is typically 5 - 15 cm, although the confinement at most varies very weakly with this distance. If the X-point moves too far outside the vessel (becomes well limited), a slight degradation in confinement results from increased ELM activity. Also if XPLIM becomes too large (~ 25 cm), the ELM frequency increases and confinement is appreciably degraded.

JET

Good H-modes are achieved with 5-8 cm. gaps between the plasma and outer belt limiter and inner wall. The main requirement seems to be that virtually all the recycling must occur at the X-point region. The position of the X-point is in general very close to the target tiles ($\leq$ 10 cm). The X-point target separation depends on plasma current. At Ip < 3MA, it can be 15 cm; at high plasma current the discharge is marginally limited.

JFT2M

Good H-modes are obtained with the outer distance between separatrix and limiter greater than 5 cm and throat length larger than 9 cm. The outer gap seems to be more important than the inner gap.

PBX-M

The X-point is kept at a reasonably large distance from any material surface, XPLIM > 14 cm. The midplane distance between the plasma and stabilizer plates on the low field side and between the plasma and the pusher coil on the high field side is quite small, ~ several cm. It is important to keep the plasma wall interaction small to obtain good H-modes, and accurate position control is critical.

PDX

Plasma is displaced upward for the best conditions to give a single null divertor with enhanced localized recycling.

II.5 Threshold conditions

ASDEX

The power required for the transition to H-mode depends weakly on n_e, I_p and B_T. It is lowest under SN conditions with the ion grad-B drift towards the X-point and with deuterium counter injection into deuterium plasmas (~ 1 MW). The threshold power is higher for hydrogen co-injection into deuterium plasmas (1.2 MW for SN and 1.8 MW for DN). High recycling (open divertor, configuration DVII with bypass conductance about 3 times neck conductance) increases the threshold to about 1.8 MW for SN and to above 2.5 MW for DN. With dirty walls, the H-mode is obtained in the SN, but not in the DN configuration.

DIII-D

The power threshold increases approximately linearly with n_e and B_T. No low density threshold is observed because the lowest densities obtainable are limited by locked modes. A slightly lower threshold is observed with the X-point closer to the divertor tiles. Deuterium injection into deuterium plasmas have a lower threshold than hydrogen into hydrogen. In all cases the threshold condition is found to be $T_e(\text{edge})/B_T > 100$ eV/T.

III.1 General

1. **TOK:** This value designates which tokamak has supplied the data. Options are ASDEX, D3D, JET, JFT2M, PBX-M, PDX.

2. **UPDATE:** This value indicates the most recent update for any variable listed in the database with the structure YYMMDD.

3. **DATE:** The date the shot was taken with the structure YYMMDD.

4. **SHOT:** The shot from which the data are taken.

5. **TIME:** Time during the shot at which the data are taken in seconds.

6. **PHASE:** The phase of the discharge at TIME. Possible values are OHM for ohmic, L for L-mode, H for ELM-free H-mode, HSELM for H-mode with small ELMs, and HGELM for H-mode with large ELMs.

7. **LHTIME:** The time of the L to H transition in seconds.

III.2 Plasma composition

8. **PGASA:** Mass number of the plasma working gas. If the plasma working gas is hydrogen then PGASA = 1, if the working gas is deuterium then PGASA = 2, and if the working gas is helium (He^4) then PGASA = 4.

9. **PGASZ:** Charge of the plasma working gas. If the plasma working gas is hydrogen then PGASZ = 1, if the working gas is deuterium then PGASZ = 1, and if the working gas is helium then PGASZ = 2.

10. **BGASA:** Mass number of the neutral beam gas. If the neutral beam gas is hydrogen then BGASA = 1, if the NB gas is deuterium then BGASA = 2, and if the NB gas is helium then BGASA = 4.

11. **BGASZ:** Charge of the neutral beam gas. If the neutral beam gas is hydrogen then BGASZ = 1, if the NB gas is deuterium then BGASZ = 1, and if the NB gas is helium then BGASZ = 2.

JET

H-modes are not obtained in JET at low density,. Good H-modes are achieved with target densities of 2×10^{19} m^{-3} for 3 MA and 3×10^{19} m^{-3} for 4 MA discharges. In addition the threshold power increases with toroidal field.

JFT2M

The power threshold for H-transition increases approximately linearly with q at $q > 3$. There is a threshold target density of about $n_e > 2 \times 10^{19}$ m^{-3} to achieve H-mode. In the case of hydrogen beam injection into hydrogen plasma, the threshold power is about 2 times higher than that for a deuterium plasma.

PBX-M

Threshold power down to 0.75 MW (with co-injection). No transition is observed with counter-injection even with powers up to 5 MW. Large edge pedestals in T_e and n_e after transition are seen only at higher B_T (1.6T).

PDX

The threshold condition is $P_{abs} \sim 1.7$ MW for ion grad-B drift either toward or away from single null X-point. The transition is easier to obtain the transition in $D^o \rightarrow D^+$ than in $D^o \rightarrow H^+$ or $H^o \rightarrow D^+$. Also, the transition is more difficult to obtain the transition with (lower power) counter-injection. No apparent edge T_e threshold is observed.

APPENDIX III - VARIABLE LIST

The time averaging for the majority of data is ± 2 ms for ASDEX, ± 8 ms for DIII-D, ± 100 ms for JET, ± 2.5 ms for JFT2M, ± 3.75 ms for PBX-M, and ± 5 ms for PDX. MHD analysis from DIII-D uses a full equilibrium fit. PDX uses a full equilibrium MHD fit for representative discharges. Data from JET, PBX-M, ASDEX and JFT2M are obtained with a current filament approach except for some of the JFT2M variables (RMAG, q_{95}, $\beta_I + 0.5\, l_i$, β_p, B_T, W) which are calculated with a full equilibrium fit. In the variable list the abbreviation Na is used if a variable is not available and the normal level of accuracy of a variable is often given in brackets without further explanation.

III.3 Geometry

12. **RGEO:** The plasma geometrical major radius in meters, from an MHD equilibrium fit, defined as the average of the minimum and the maximum radial extent of the plasma.
Normal level of accuracy is ASDEX (± 0.5%), D3D (± 0.6%) JET (± 1%), JFT2M (± 0.75%), PBX-M (± 0.65%), PDX (± 0.75%).

13. **RMAG:** The major radius of the magnetic axis in meters from an MHD equilibrium fit.
Normal level of accuracy is ASDEX (± 0.5%), D3D (± 1%), JET (± 2%), PBX-M (± 1%), PDX (± 4%), JFT2M (±2%).

14. **AMIN:** The horizontal plasma minor radius in meters from an MHD equilibrium fit.
Normal level of accuracy is ASDEX (± 1%), D3D (± 0.5%), JET (± 3%), JFT2M (± 3%), PBX-M (± 3%), PDX (± 3%).

15. **SEPLIM:** The minimum distance between the separatrix flux surface and either the vessel wall or limiters in meters from an MHD equilibrium fit.
Normal level of accuracy is ASDEX (± 1 cm), D3D (± 0.5 cm), JET (± 1 cm), JFT2M (± 1 cm), PBX-M (± 0.5 cm), PDX (± 1 cm).

16. **XPLIM:** The minimum distance between the X-point and either the vessel walls or limiters in meters from an MHD equilibrium fit.
Normal level of accuracy is ASDEX (Na), D3D (± 3 cm), JET (± 5 cm), JFT2M (± 3 cm), PBX-M (± 5 cm), PDX (± 5 cm).

17. **KAPPA:** The plasma elongation determined from an MHD equilibrium fit.
Normal level of accuracy is ASDEX (± 1%), D3D (± 1%), JET (± 5%), JFT2M (± 10%), PBX-M (± 10%), PDX ($\kappa = 1$ for all records, ± 10%).

18. **DELTA:** The triangularity of the plasma boundary from an MHD equilibrium fit.
Normal level of accuracy is ASDEX (Na), D3D (± 10%), JET (± 10%), JFT2M (± 10%), PBX-M (± 25%), PDX (Na).

19. **INDENT:** Indentation of the plasma determined from an MHD equilibrium fit.

Normal level of accuracy is ASDEX (Na), D3D (Na), JET (Na), JFT2M (Na), PBX-M (± 15%), PDX (Na).

20. **AREA:** Area of plasma cross section in m^2 determined from an MHD equilibrium fit.
Normal level of accuracy is ASDEX (± 3%), D3D (± 3%), JET (± 6%), JFT2M (± 5%), PBX-M (± 10%), PDX (± 5%).

21. **VOL:** The plasmas volume in m^3 determined from an MHD equilibrium fit.
Normal level of accuracy is ASDEX (± 3%), D3D (± 3%), JET (± 6%), JFT2M (± 5%), PBX-M (± 10%), PDX (± 5%).

22. **CONFIG:** The plasma configuration. Possible values are SN for single null and DN for double null.

ASDEX:	DN if vertical shift ΔZ is less than 5 mm, otherwise SN.
D3D:	DN if two nulls and the separatrix flux surface are inside the divertor tiles and on the same flux surface within 0.25 cm.
JET:	Determined by operation session leader.
JFT2M:	DN if two nulls are inside the limiter.
PBX-M:	DN
PDX:	SN

III.4 Machine condition

23. **WALMAT:** The material of the vessel wall with possible values SS for stainless steel, IN for inconel, C for carbon, and IN/C for Inconel with carbon.

24. **DIVMAT:** The material of the divertor tiles with possible values SS for stainless steel, IN for inconel, C for carbon, CU for copper and TI for titanium.

25. **LIMMAT:** The material of the limiters with possible values BE for beryllium, and C for carbon.

26. **EVAP:** The evaporated material used to cover the inside of the vessel with possible values BO for boron, C for carbon, TI for titanium and NONE for no evaporation.

III.5 Magnetics

27. **BT:** The vacuum toroidal magnetic field in Tesla at RGEO determined from the TF coil current.
Normal level of accuracy is ± 1% for all machines.

28. **IP:** The plasma current in amperes determined from an external Rogowski loop with vessel current subtraction.
Normal level of accuracy is ASDEX (± 2%), D3D (± 1%), JET (± 1%), JFT2M (± 1%), PBX-M (± 1%), PDX (± 1%).

29. **VSURF:** The loop voltage at the plasma boundary in volts.
Normal level of accuracy is ASDEX (± 5%), D3D (Na), JET (± 5%), JFT2M (± 5%), PBX-M (± 50%), PDX (± 10%).

30. **Q95:** The plasma safety factor from the MHD equilibrium fit evaluated at the flux surface that encloses 95% of the total poloidal flux.
Normal level of accuracy is ASDEX (± 15%), D3D (± 3%), JET (± 10%), JFT2M (± 10%) PBX-M (± 10%), PDX (± 10%).

31. **BEILI2:** This quantity is determined from MHD and represents $\beta_i + 0.5\, l_i$, where β_i is the shafranov beta and l_i the internal inductance. Normal level of accuracy is ASDEX (± 10%).

32. **BEIMHD:** Beta Shafranov from MHD.
Normal level of accuracy is ASDEX (± 15%).

33. **BEPMHD:** Poloidal beta computed from the MHD equilibrium fit.
Normal level of accuracy is ASDEX (± 15%), D3D (± .05), JET (Na), JFT2M (± 15%), PBX-M (± 20%), PDX (± 20%).

34. **BETMHD:** Toroidal beta computed from the MHD equilibrium fit.
Normal level of accuracy is ASDEX (± 18%), D3D (± $0.05/\beta_p$), JET (± 12%), JFT2M (± 10%), PBX-M (± 20%), PDX (± 20%).

35. **NEL:** Central line average electron density in m^{-3} from interferometer. Normal level of accuracy is ASDEX (± 2%), D3D (± 2×10^{18} m^{-3}), JET (± 8%), JFT2M (± 2%), PBX-M (± 5%), PDX (± 5%).

36. **DNELDT:** The time rate of change of NEL in m^{-3}/s.
Normal level of accuracy is similar to NEL.

37. **NEV:** The volume averaged electron density in m^{-3}.

ASDEX: Determined before shot 18023: from 4 interferometry channels fitting
$n(x) = n(1) + (n(0) - n(1))\,(1 - x^{\alpha})^{\beta}$, $0 \le x \le 1$, (± 5%)
After shot 18023: from 16 radial YAG laser measurements fitting
$n(x) = n(o)\exp(ax^2 + bx^4 + cx^6)$, $0 \le x \le 1$, (± 5%).
For all volume integrations (NEV, TEV, WEKIN), a circular plasma was assumed.

D3D: Determined by a spline density profile fit to the CO_2 and Thomson scattering density data (± 10%).

JET: Determined from weighted summation over 6 interferometer channels (± 10%).

JFT2M: Determined from an analytic fit with fixed profile shape to 2 interferometer channels (± 30%).

PBX-M, PDX: (Na).

38. **NEØ:** The central electron density at the magnetic axis in m^{-3} determined in same manner as NEV.
Normal level of accuracy if ASDEX (± 10%).

39. **NEØTSC:** The electron density in m^{-3} determined from Thomson scattering.

ASDEX: Average of the 3 YAG laser channels closest to the equatorial plane, (± 5%).

D3D: Thomson scattering point that is closest to the magnetic axis (less than 10 cms).

JET, JFT2M, PBX-M, PDX: Na.

III.6 Impurities

40. **ZEFF:** Line average plasma effective charge.

D3D: Determined from visible bremsstrahlung, (± 20%).

JET: Determined from visible bremsstrahlung, (± 30%).

ASDEX, JFT2M, PBX-M, PDX: Na.

41. **ZEFFNEO:** Plasma effective charge as determined by neoclassical resistivity.

JET: Determined using volume averaged quantities (± 25%).
ASDEX, D3D, JFT2M, PBX-M, PDX: Na.

42. **PRAD:** Total radiated power in watts as measured by Bolometer.
Normal level of accuracy is ASDEX (± 20%), D3D (± 15%), JET (± 10-15%), JFT2M (± 10 - 20%), PBX-M (± < 25%), PDX (Na).

III.7 Input powers

43. **POHM:** Total ohmic power in watts.

ASDEX:	Determined from max {0, VSURF × IP}, (Ohmic: ± 5% H: ± 50%).
D3D:	Calculated using $CB_{10}I_p^2V/(W_T n_e)$. B_{10} is the line average electron density. When n_e is determined from the radial (vertical) CO_2 chord C is equal to 1.43×10^{-8} (1.37×10^{-8}) (± 15%).
JET:	Corrected for inductance effects (± 20%).
JFT2M:	Calculated as VSURF × IP (± 10%).
PBX-M:	Calculated as VSURF × IP (± 50%).
PDX:	Calculated using VSURF and IP corrected for inductance effects (± 20%).

44. **ENBI:** Neutral beam energy weighted by power in volts. This quantity is calculated from $\Sigma E_i P_i / \Sigma P_i$ where E_i is the beam energy and P_i is the beam power for source i. ASDEX (primary energy component given).

45. **PINJ:** Total injected neutral beam power that passes into the torus in watts.
Normal level of accuracy for this variable is ASDEX (± 10%), D3D (± 10%), JET (± 6%), JFT2M (± 5%), PBX-M (± 5%), PDX (± 10%).

46. **PABS:** Total injected neutral beam power minus shine through in watts. (For ASDEX, total injected power minus shine-through, charge-exchange and orbit losses[6]).
Normal level of accuracy is ASDEX (± 10%), D3D (± 10%), JET (± 10%), JFT2M (< ± 10%), PBX-M (± 10%), PDX (± 10%).

47. **PFLOSS:** Amount of neutral beam power in watts that is lost from the plasma through charge exchange and unconfined orbits.

---

[6] PABS for ASDEX will be modified to have only shine-through losses subtracted in ITERHDB.2.

ASDEX: PINJ-PABS[7] (from fits to the FREYA code results, ±30%)
D3D: Not yet in the database.
JET: Set to zero.
JFT2M: From fits to Monte Carlo code results (± 20%).
PBX-M: From fits to the TRANSP code results (± 20%).
PDX: From fits to the TRANSP code results (± 30%).

48. **DWDIA:** Time rate of change of the total plasma stored energy as determined by the diamagnetic loop in watts.

ASDEX: Parabolic fit to time evolution of diamagnetic beta β_p over ± 6 ms when DWHC = 0 (± 20%). Set by hand from drawing the tangent to the WDIA timetrace when DWHC = 1.
JET: Running average method over ± 100 ms (± 10%).
JFT2M: Simple derivative over 10 ms.
D3D, PBX-M, PDX: Na.

49. **DWMHD:** Time rate of change of the total plasma stored energy as determined from MHD in watts.

ASDEX: As for DWDIA (± 20%).
D3D: A spline fit is made to W and this fitted curve is then differentiated (± 25%).
JET: As for DWDIA (± 20%).
JFT2M: As for DWDIA with 5 ms integration time.
PBX-M: (± 10%).
PDX: (± 10%).

III.8 Temperatures

50. **TEV:** The volume averaged electron temperature eV.

ASDEX: From 16 radial YAG measurements fitting $T_e(x) = T_e(0) \exp(ax^2 + bx^4 + cx^6)$, (± 5%).
D3D: Determined by a spline temperature profile fit to the Thomson scattering data (± 10%).
JET: From 51 point ECE temperature profile (± 10%).
JFT2M: Na.
PBX-M: Volume averaged electron temperature computed from BETMHD, VOL, NEL, assuming $Z_{eff} = 1$ (± 30%).
PDX: Volume averaged electron temperature computed from BETMHD, VOL, NEL, assuming $Z_{eff} = 1$ (± 30%).

51. **TEØ:** The electron temperature at the magnetic axis in eV.

---

[7] PFLOSS for ASDEX will be modified to include only bad orbit and charge exchange losses subtracted in ITERHDB.2.

ASDEX: From 16 radial YAG measurements under the same profile assumptions as for TEV (± 10%).
D3D: Determined by a spline temperature profile fit to the Thomson scattering data (± 10%).
JET: From ECE temperature profile (± 10%).
JFT2M, PBX-M, PDX: Na.

52. **TEØTSC:** The electron temperature in eV determined from the Thomson scattering point that is closest to the magnetic axis.

ASDEX: Average of the 3 YAG laser channels closest to the equatorial plane, (± 5%).
D3D: Determined by a spline temperature profile fit to the Thomson scattering data. (± 10%).
JET, JFT2M, PBX-M, PDX: Na.

53. **TIV:** The volume averaged ion temperature in eV.

D3D: Determined by a spline temperature profile fit to the charge exchange recombination data (± 10%).
JET: Estimated from TIV = TIØ × TEV/TEØ (± 30%).
PBX-M, PDX: TIV = TEV (± 30%).
ASDEX, JFT2M: Na.

54. **TIØ:** The ion temperature at the magnetic axis in eV.

D3D: Determined by a spline temperature profile fit to the charge exchange recombination data (± 10%).
JET: From charge exchange recombination spectroscopy (± 10%).
ASDEX, JFT2M, PBX-M, PDX: Na.

III.9 Energies

55. **WDIA:** Total plasma energy in joules as determined from the diamagnetic loop.

ASDEX: Diamagnetic energy, $0.471 R_{geo}\ 10^{-6} Ip^2 \beta_p$ (dia), (ohmic: ± 20%, H: ± 10%).
Normal level of accuracy is D3D (± $0.1/\beta_p$), JET (± 5%), JFT2M (± 1-2 KJ in ohmic).
PBX-M, PDX: Na.

56. **WMHD:** Total plasma energy in joules as determined by a MHD equilibrium fit.

ASDEX: MHD energy, 0.471 $R_{geo}\ 10^{-6} I_p^2 \beta_p$ (MHD), (ohmic: ± 20%, H: ± 10%).

Normal level of accuracy is D3D (± $0.05/\beta_p$), JET (± 15%), JFT2M (± 15%), PBX-M (± 15%), PDX (± 15%).

57. **WKIN:** Total thermal plasma energy in joules as determined from kinetic measurements.

D3D: Normal level of accuracy is ± $0.05/\beta_p$.
JET: From a profile fit assuming flat Z_{eff} profile and T_i profile as T_e (± 25%).

ASDEX, JFT2M, PBX-M, PDX: Na.

58. **WEKIN:** Total thermal electron plasma energy in joules as determined from kinetic measurements.

Normal level of accuracy is ASDEX (± 10%, H: ± 15%), D3D (± 15%), JET (±20%). JFT2M, PBX-M, PDX: Na.

59. **WIKIN:** Total thermal ion plasma energy in joules as determined from kinetic measurements.

D3D: Error ± 15%.
JET: From ECE temperature profile shape normalized to T_i (o) from crystal X-ray diagnostic (± 15%).

ASDEX, JFT2M, PBX-M, PDX: Na.

60. **WFPER:** Total perpendicular fast ion energy in joules as determined from transport calculations.

JET: Calculated from the PENCIL code (± 30%).
JFT2M: From Monte Carlo code (± 20%).
PBX-M: Calculated from slowing down formula and calibrated from several representative TRANSP runs (± 30%).
PDX: Calculated from slowing down formula and calibrated from several representative TRANSP runs (± 50%).

ASDEX, D3D: Na.

61. **WFPAR:** Total parallel fast ion energy in joules as determined from transport calculations.

JET: Calculated from the PENCIL code (± 30%).
JFT2M: From Monte Carlo code (± 20%).

PBX-M: Calculated from slowing down formula and calibrated from several representative TRANSP runs (± 30%).
PDX: Calculated from slowing down formula and calibrated from several representative TRANSP runs (± 50%).
ASDEX, D3D: Na.

62. **WFFORM:** Total fast ion energy in joules estimated from approximate formula.

JET: From $.16 \times 10^{19}$ PINJ/NEV.

63. **WFANI:** Estimate of fraction of perpendicular fast ion energy as compared to the total fast ion energy (± 50%).

III.10 Energy confinement times

64. **TAUDIA:** Total diamagnetic energy confinement time (WDIA/(POHM + PABS - DWDIA)) in seconds.
Normal level of accuracy is ASDEX (ohmic ± 25%, H ± 15%), D3D (± 15%), JET (± 25% for Ohmic, ±10% for H-mode), JFT2M (± 20%), D3D (± 15%).
PBX-M, PDX: Na.

65. **TAUMHD:** Total MHD energy confinement time (WMHD/(POHM + PABS - DWMHD)) in seconds.
Normal level of accuracy is ASDEX (H ± 15%), D3D (± 15%), JET (± 35%), JFT2M (± 20%), PBXM (± 20%), PDX (± 20%).

66. **TAUTH1:** Thermal energy confinement time (WKIN/(POHM + PABS - DWMHD-PFLOSS)) in seconds.
Normal level of accuracy is D3D (± 25%), JET (± 35%).
ASDEX, JFT2M, PBX-M, PDX: Na.

67. **TAUTH2:** Thermal energy confinement time (WMHD-WFFORM)/(POHM + PABS - DWMHD - PFLOSS)) in seconds. For both PBX-M and PDX, 3.4 $W_{f\perp}+3/2W_{f\parallel}$ was used instead of WFFORM.
Normal level of accuracy is ASDEX (± 30%) , JET (± 30%), JFT-2M (± 25%), PBX-M (≥ ± 30%), PDX (≥ ± 40%).
D3D: Na.

III.11 Extra information

68. **BMHDMDIA:** Offset for ASDEX between diamagnetic beta poloidal and MHD beta poloidal during the ohmic phase.

69. **PELLET:** Pellet material if a pellet has been injected.
JFT2M: Set to H or D.
ASDEX, D3D, JET, PBX-M, PDX: No pellets

70. **COCTR:** Fraction of beam power co-injected as compared to to the total beam power injected.

71. **BSOURCE:** The power fractions injected by neutral beam e.g. P_1 = 80%, P_2 = 10% and P_3 = 10% then BSOURCE = 801010.

72. **DALFMP:** D_α emission on the mid plane for PDX.

73. **DALFDV:** D_α emission in the divertor for PDX.

74. **DWDIAPAR:** Time derivative for ASDEX of W_{dia} from a parabolic fit to the three available H-mode points. DWDIAPAR has been used in calculating TAUDIA.

75. **BEPDIA:** Corrected poloidal diamagnetic beta for ASDEX from diamagnetic coils averaged over the 3 ohmic points in the database, (± 15%).

76. **DWHC:** = 1 when DWDIA and DWMHD have been corrected by hand for ASDEX.

FIGURE CAPTIONS

Fig. 1 Definition of inverse aspect ratio, elongation, triangularity and indentation.

Fig. 2 Example of review sheet from ASDEX.

Fig. 3 Example of review sheet from DIII-D.

Fig. 4 Example of review sheet from JET.

Fig. 5 Example of review sheet from JFT2M

Fig. 6 Example of review sheet from PBX-M.

Fig. 7 Example of review sheet from PDX.

Fig. 8 2-dimensional example of changing from coordinates (x_1, x_2) to principal component coordinates (y_1, y_2).

Fig. 9 (a) τ_E versus 1.65 × Goldston L-mode scaling [28].
(b) Corresponding data frequency versus τ_E/(1.65 × Goldston).

Fig. 10 (a) τ_E versus 2.02 × Kaye-Big L-mode scaling [2].
(b) Corresponding data frequency versus τ_E/(2.02 × Kaye-Big).

Fig. 11 (a) τ_E versus 2.11 × ITER89-P L-mode scaling [29].
(b) Corresponding data frequency versus τ_E/(2.11 × ITER89-P).

Fig. 12 (a) τ_E versus 2.35 × Rebut-Lallia L-mode scaling [30] assuming $Z_{eff} = 3$ and $F_r = 2$. (b) Corresponding data frequency versus τ_E/(2.35 × Rebut-Lallia).

Fig. 13 τ_E versus the resulting fit from regression on the standard dataset.

Fig. 14 τ_E versus the resulting fit (ITER90H-P) from regression on the ELM-free dataset with the B_T dependence fixed.

Fig. 15 τ_E versus the resulting fit from regression on the ELM-free dataset for the alternate regression (Eq. 8).

Fig. 16 The physics variables $\tilde{\beta}$ versus $\tilde{\rho}/a$ on natural logarithmic scale from the ELM-free dataset.

Fig. 17 The physics variables $\tilde{\beta}$ versus $\tilde{\nu}^*$ on natural logarithmic scale from the ELM-free dataset.

Fig. 18 Thermal part of the energy versus input power for (a) JFT2M, (b) JET, (c) DIII-D. Currents chosen are 135 kA, 170 kA, 210 kA, 255 kA (JFT2M), 2MA, 3.1MA (JET) and 1MA, 1.9MA (DIII-D).

Fig. 19 Incremental confinement time versus current for (a) JFT2M, (b) JET and (c) DIII-D.

Fig. 20 Size dependence of the incremental confinement time.

Fig. 21 Offset part of the thermal energy versus current for (a) JFT2M , (b) JET and (c) DIII-D.

Fig. 22 The magnetic field dependence of the offset part of the thermal energy for (a) JFT2M, (b) JET, and (c) DIII-D.

Fig. 23 Size dependence of the offset part of the thermal energy.

Fig. 24 (a) Comparison of the offset linear scaling with the data from D- shaped open divertor tokamaks. Root mean square error is about 14.5%. (b) Data from ASDEX, PBX-M and PDX are compared to the offset linear scaling. The number of data points from each tokamak is given in brackets.

Fig. 25 Distribution of the enhancement factor for (a) ASDEX, (b) DIII-D and (c) JFT2M. Abscissa is the energy confinement time normalized to the ITER89-P L-mode scaling expression.

Machine	Total	Selection Criteria						
		H-mode	P_{rad}	Fast Ions	Low q	$\dot{W}$	MHD	Net
ASDEX	1071	612	31	0	391	183	0	256
DIII-D	152	3	10	1	4	7	0	121
JET	1171	513	606	0	27	322	0	286
JFT2M	654	218	100	2	160	46	0	231
PBX-M	264	0	32	4	0	7	7	216
PDX	154	0	0	15	0	9	2	129
Totals	**3466**	**1346**	**779**	**22**	**582**	**574**	**9**	**1239**
→								

Table I *Number of observations eliminated by the criteria (1-6) for each tokamak.*

All Tokamaks

Variables	Units	Number	Data range	Mean	Std. dev.
Toroidal field B_T	Tesla	1239	1.05 - 3.72	1.87	0.56
Plasma current I_p	MA	1239	0.14 - 5.13	1.04	1.19
Average density n	10^{19} m^{-3}	1239	1.66 - 11.7	4.35	1.56
Major radius R	m	1239	1.29 - 2.91	1.83	0.56
Minor radius a	m	1239	0.25 - 1.14	0.53	0.32
Elongation κ		1239	0.93 - 2.0	1.45	0.35
Inverse aspect ratio e		1239	0.16 - 0.40	0.27	0.09
Safety factor q_{cyl}		1239	1.87 - 9.15	2.70	0.69
q at 95% flux surface q95		1239	1.87 - 9.15	3.97	0.97
Ion mass (ave. beam and plasma) A	AMU	1239	1 - 2	1.75	0.31
Absorbed power Pabs	MW	1239	0.18 - 17.9	3.69	2.81
Ohmic power Pohm	MW	1239	0.00 - 3.34	0.29	0.33
MHD Conf. Time τ_{mhd}	s	1239	1.2e-2 - 1.21	0.21	0.29
Diam. Conf. Time τ_{dia}	s	849	1.2e-2 - 1.30	0.30	0.36
MHD Stored Energy W_{mhd}	MJ	1239	1.3e-2 - 10.2	1.23	2.03
Diam. Stored Energy W_{dia}	MJ	850	1.2e-2 - 10.7	1.82	2.49
Bohm time τ_B	ms	1239	5.e-3 - 0.46	8.0e-2	0.10
Collisionality ν^*	s^{-1}	1239	1e-3 - 1.32	0.04	0.07
Plasma beta β		1239	9.9e-2 - 2.22	0.89	0.47
Larmor radius ρ/a		1239	0.00 - 2e-3	1e-3	0.00

ASDEX

Variables	Units	Number	Data range	Mean	Std. dev.
Toroidal field B_T	Tesla	256	1.57 - 2.61	2.18	0.13
Plasma current I_p	MA	256	0.20 - 0.43	0.32	4.1e-2
Average density n	10^{19} m^{-3}	256	2.1 - 6.8	3.86	0.76
Major radius R	m	256	1.63 - 1.71	1.67	1.7e-2
Minor radius a	m	256	0.37 - 0.43	0.40	1.0e-2
Elongation κ		256	0.93 - 1.02	0.99	1.5e-2
Inverse aspect ratio ϵ		256	0.22 - 0.26	0.24	6e-3
Safety factor q_{cyl}		256	2.60 - 5.83	3.29	0.54
q at 95% flux surface q95		256	3.10 - 9.14	4.08	0.91
Ion mass (ave. beam and plasma) A	AMU	256	1.5 - 1.5	1.5	0
Absorbed power Pabs	MW	256	1.37 - 3.56	2.46	0.47
Ohmic power Pohm	MW	256	0.00 - 0.73	0.13	0.12
MHD Conf. Time τ_{mhd}	s	256	3.9e-2 - 9.9e-2	6.4e-2	1.2e-2
Diam. Conf. Time τ_{dia}	s	256	3.0e-2 - 8.4e-2	5.1e-2	9e-3
MHD Stored Energy W_{mhd}	MJ	256	8.1e-2 - 0.22	0.14	3.1e-2
Diam. Stored Energy W_{dia}	MJ	256	6.2e-2 - 0.19	0.12	2.5e-2
Bohm time τ_B	ms	256	1.2e-2 - 3.2e-2	1.8e-2	3e-3
Collisionality ν^*	s^{-1}	256	0.74 - 2.22	2.7e-2	1.8e-2
Plasma beta β		256	0.74 - 2.22	1.36	0.26
Larmor radius ρ/a		256	1e-3 - 2e-3	1e-3	0.00

DIII-D

Variables	Units	Number	Data range	Mean	Std. dev.
Toroidal field B_T	Tesla	121	1.46 - 2.13	1.97	0.25
Plasma current I_p	MA	121	0.62 - 2.23	1.40	0.41
Average density n	10^{19} m^{-3}	121	2.72 - 11.6	7.02	2.18
Major radius R	m	121	1.66 - 1.69	1.67	8e-3
Minor radius a	m	121	0.61 - 0.63	0.62	4e-3
Elongation κ		121	1.76 - 2.0	1.85	4.8e-2
Inverse aspect ratio e		121	0.36 - 0.37	0.37	2e-3
Safety factor q_{cyl}		121	1.99 - 5.36	2.92	0.77
q at 95% flux surface q95		121	3.22 - 9.11	4.61	1.28
Ion mass (ave. beam and plasma) A	AMU	121	1 - 2	1.91	0.29
Absorbed power Pabs	MW	121	1.16 - 11.1	5.82	2.34
Ohmic power Pohm	MW	121	8.4e-2 - 1.52	0.54	0.29
MHD Conf. Time τ_{mhd}	s	121	6e-2 - 0.30	0.17	5.6e-2
Diam. Conf. Time τ_{dia}	s	76	5.5e-2 - 0.34	0.15	5.8e-2
MHD Stored Energy W_{mhd}	MJ	121	0.22 - 1.59	0.93	0.36
Diam. Stored Energy W_{dia}	MJ	97	0.19 - 1.53	0.88	0.36
Bohm time τ_B	ms	121	3.8e-2 - 0.29	0.13	4.2e-2
Collisionality ν^*	s^{-1}	121	3e-3 - 7.8e-2	0.03	1.6e-2
Plasma beta β		121	0.24 - 1.16	0.57	0.20
Larmor radius ρ/a		121	0.00 - 0.01	0.00	0.00

JET

Variables	Units	Number	Data range	Mean	Std. dev.
Toroidal field B_T	Tesla	286	1.81 - 3.72	2.55	0.45
Plasma current I_p	MA	286	2.01 - 5.13	3.03	0.66
Average density n	10^{19} m^{-3}	286	1.66 - 5.86	3.53	0.85
Major radius R	m	286	2.72 - 2.91	2.81	4.9e-2
Minor radius a	m	286	1.06 - 1.13	1.09	1.4e-2
Elongation κ		286	1.70 - 1.91	1.83	4.3e-2
Inverse aspect ratio e		286	0.37 - 0.40	0.39	6e-3
Safety factor q_{cyl}		286	2.01 - 4.85	3.08	0.56
q at 95% flux surface q95		286	3.23 - 7.92	4.45	0.79
Ion mass (ave. beam and plasma) A	AMU	286	2 - 2	2	0.00
Absorbed power Pabs	MW	286	3.11 - 17.9	7.50	2.28
Ohmic power Pohm	MW	286	0.00 - 3.34	0.56	0.51
MHD Conf. Time τ_{mhd}	s	286	0.40 - 1.21	0.71	0.17
Diam. Conf. Time τ_{dia}	s	286	0.45 - 1.30	0.79	0.18
MHD Stored Energy W_{mhd}	MJ	286	2.00 - 10.2	4.63	1.55
Diam. Stored Energy W_{dia}	MJ	286	2.44 - 10.7	5.10	1.61
Bohm time τ_B	ms	286	0.11 - 0.46	0.24	6.6e-2
Collisionality ν^*	s^{-1}	286	1e-3 - 1.8e-2	6e-3	3e-3
Plasma beta β		286	0.10 - 0.71	0.38	0.14
Larmor radius ρ/a		1239	0.00 - 0.00	0.00	0.00

JFT-2M

Variables	Units	Number	Data range	Mean	Std. dev.
Toroidal field B_T	Tesla	231	1.07 - 1.32	1.26	2.7e-2
Plasma current I_p	MA	231	0.14 - 0.26	0.22	3.7e-2
Average density n	10^{19} m^{-3}	231	2.12 - 7.28	4.24	0.97
Major radius R	m	231	1.29 - 1.32	1.30	8e-3
Minor radius a	m	231	0.25 - 0.29	0.27	6e-3
Elongation κ		231	1.30 1.45	1.40	3.4e-2
Inverse aspect ratio e		231	0.19 - 0.22	0.21	5e-3
Safety factor q_{cyl}		231	1.94 - 3.37	2.30	0.37
q at 95% flux surface q95		231	2.70 - 4.61	3.15	0.52
Ion mass (ave. beam and plasma) A	AMU	231	1 - 1.5	1.34	0.23
Absorbed power Pabs	MW	231	0.18 - 1.59	0.91	0.40
Ohmic power Pohm	MW	231	0.03 - 0.33	0.16	0.07
MHD Conf. Time τ_{mhd}	s	231	1.5e-2 - 7.5e-2	3.1e-2	1.2e-2
Diam. Conf. Time τ_{dia}	s	231	1.2e-2 - 6.5e-2	2.6e-2	1.0e-2
MHD Stored Energy W_{mhd}	MJ	231	1.3e-2 - 4.5e-2	2.9e-2	6e-3
Diam. Stored Energy W_{dia}	MJ	231	1.2e-2 - 3.7e-2	2.3e-2	5e-3
Bohm time τ_B	ms	231	1.1e-2 - 3.0e-2	2e-2	3e-3
Collisionality ν^*	s^{-1}	231	2.9e-2 - 0.23	9.6e-2	3.9e-2
Plasma beta β		231	0.50 - 1.32	0.81	0.16
Larmor radius ρ/a		231	1e-3 - 2e03	1e-3	0.00

PBX-M

Variables	Units	Number	Data range	Mean	Std. dev.
Toroidal field B_T	Tesla	216	1.30 - 1.43	1.34	3.7e-2
Plasma current I_p	MA	216	0.28 - 0.39	0.33	1.9e-2
Average density n	10^{19} m^{-3}	216	2.35 - 8.97	4.87	1.27
Major radius R	m	216	1.62 - 1.66	1.65	8e-3
Minor radius a	m	216	0.25 - 0.29	0.27	6e-3
Elongation κ		216	1.52 - 1.70	1.61	3.0e-2
Inverse aspect ratio e		216	0.16 - 0.18	0.16	4e-3
Safety factor q_{cyl}		216	1.66 - 2.35	1.90	0.16
q at 95% flux surface q95		216	3.38 - 5.79	4.33	0.56
Ion mass (ave. beam and plasma) A	AMU	216	2 - 2	2	0.00
Absorbed power Pabs	MW	216	1.37 - 4.81	2.86	0.86
Ohmic power Pohm	MW	216	1e-3 - 0.49	0.16	0.11
MHD Conf. Time τ_{mhd}	s	216	3.3e-2 - 8.1e-2	5.2e-2	9e-2
Diam. Conf. Time τ_{dia}	s	0	-	-	-
MHD Stored Energy W_{mhd}	MJ	216	9.2e-2 - 0.21	0.14	2.7e-2
Diam. Stored Energy W_{dia}	MJ	0	-	-	-
Bohm time τ_B	ms	216	5.e-3 - 0.02	1.0e-2	3e-3
Collisionality ν^*	s^{-1}	216	2e-2 - 8.8e-2	1.5e-2	1.6e-2
Plasma beta β		216	0.88 - 2.12	1.45	0.27
Larmor radius ρ/a		216	1.0e-3 - 2e-3	1e-3	0.00

PDX

Variables	Units	Number	Data range	Mean	Std. dev.
Toroidal field B_T	Tesla	129	1.05 - 2.04	1.66	0.23
Plasma current I_p	MA	129	0.24 - 0.46	0.38	5.1e-2
Average density n	10^{19} m^{-3}	129	2.31 - 9.86	3.94	1.55
Major radius R	m	129	1.40 - 1.40	1.40	0.00
Minor radius a	m	129	0.43 - 0.42	0.40	4e-3
Elongation κ		129	1.00 - 1.00	1.00	0.00
Inverse aspect ratio e		129	0.29 - 0.30	0.29	3e-3
Safety factor q_{cyl}		129	1.67 - 3.85	2.55	0.33
q at 95% flux surface q95		129	1.87 - 4.75	2.98	0.42
Ion mass (ave. beam and plasma) A	AMU	129	1.5 - 2	1.84	0.24
Absorbed power Pabs	MW	129	0.94 - 3.45	2.10	0.50
Ohmic power Pohm	MW	129	0.05 - 0.38	0.20	6.9e-2
MHD Conf. Time τ_{mhd}	s	129	1.2e-2 - 8.8e-2	3.5e-2	1.1e-2
Diam. Conf. Time τ_{dia}	s	0	-	-	-
MHD Stored Energy W_{mhd}	MJ	129	2.3e-2 - 0.12	7.3e-2	2.1e-2
Diam. Stored Energy W_{dia}	MJ	0	-	-	-
Bohm time τ_B	ms	129	1.7e-2 - 8.2e-2	3.5e-2	1.3e-2
Collisionality ν^*	s^{-1}	129	1.1e-2 - 1.32	9.8e-2	0.19
Plasma beta β		129	0.32 - 1.23	0.64	0.20
Larmor radius ρ/a		129	1.0e-3 - 1e-3	1e-3	0.00

Table II *The units, data range (min. - max.) and standard deviations of the basic variables in the standard H-mode dataset (n=1239). The variables τ_B, ρ/a, ν^* and β are defined in section 4.3.*

(a)		Log (I_p)	Log (B_T)	Log (n)	Log (P_L)	Log (R)	Log (1/ε)	Log (κ)
	Mean	13.10	0.65	45.21	14.86	0.51	1.33	0.20
	Std. dev.	0.77	0.23	0.35	0.54	0.17	0.25	0.28
	Log (I_p)	1.00						
Elements	Log (B_T)	0.38	1.00					
of	Log (n)	0.24	-0.23	1.00				
correlation	Log (P_L)	**0.76**	0.26	0.44	1.00			
matrix	Log (R)	**0.72**	0.59	-0.10	0.54	1.00		
	Log (1/ε)	**-0.76**	-0.41	-0.03	-0.52	-0.36	1.00	
	Log (κ)	**0.76**	-0.10	0.49	**0.68**	0.47	-0.35	1.00

(b)		Log (I_p)	Log (B_T)	Log (n)	Log (P_L)	Log (R)	Log (1/ε)	Log (κ)
	Mean	13.41	0.53	45.13	14.79	0.61	1.37	0.45
	Std. dev.	1.17	0.32	0.28	0.83	0.33	0.36	0.16
	Log (I_p)	1.00						
Elements	Log (B_T)	**0.93**	1.00					
of	Log (n)	-0.16	-0.21	1.00				
correlation	Log (P_L)	**0.87**	**0.83**	-0.07	1.00			
matrix	Log (R)	**0.95**	**0.88**	-0.32	**0.88**	1.00		
	Log (1/ε)	**-0.90**	**-0.89**	0.23	**-0.69**	**-0.80**	1.00	
	Log (κ)	**0.75**	0.54	0.00	**0.70**	**0.74**	-0.51	1.00

Table III *Data description of standard dataset. All tokamaks are included and P_L is calculated from P_T and $\dot{W}_{MHD}$.*
The mean, standard deviation and correlation matrix are given for the two subsets (a) with ELMs (548 observations) and (b) ELM-free (691 obs.) separately. Correlations $|\rho| \geq 0.7$ are typed in bold-face.

Subset	p.c.	Log (I_p)	Log (B_T)	Log (n)	Log (P_L)	Log (R)	Log (1/ε)	Log (κ)	STD	ERR	ITER
With ELMS	1	**0.80**	0.10	0.15	0.50	0.10	-0.20	0.25	0.952	0.03	5.9
τ_{mhd} available	2	-0.30	-0.30	**0.75**	0.40	-0.15	0.20	0.20	0.400	0.10	1.8
548 obs.	3	-0.35	0.35	-0.30	**0.75**	0.10	0.05	-0.35	0.273	0.15	5.5
	4	0.05	0.55	0.55	-0.20	-0.10	-0.35	-0.45	0.209	0.15	0.8
	5	0.05	0.50	0.15	-0.15	0.45	**0.70**	0.20	0.177	0.08	3.9
	6	-0.30	0.45	-0.10	0.00	-0.25	-0.30	**0.75**	0.082	0.13	-7.1
	7	-0.25	-0.20	0.10	0.00	**0.80**	-0.45	0.10	0.061	0.15	2.6
With ELMS	1	**0.80**	0.05	0.10	0.50	0.10	-0.20	0.25	1.072	0.02	5.1
τ_{dia} available	2	-0.35	-0.15	**0.75**	0.50	-0.25	0.00	0.00	0.352	0.13	3.0
360 obs.	3	-0.30	0.35	-0.45	**0.70**	0.15	0.05	-0.35	0.303	0.14	4.8
	4	0.20	**0.70**	0.45	-0.25	0.20	0.20	-0.40	0.177	0.15	43.8
	5	-0.25	0.60	-0.05	-0.05	-0.20	-0.40	0.60	0.068	0.15	-6.3
	6	0.20	0.15	-0.15	0.05	-0.65	**0.70**	0.15	0.052	0.22	0.7
	7	-0.20	0.00	0.10	0.05	0.65	0.50	0.55	0.031	0.33	21.6
ELM-free	1	**0.75**	0.20	-0.05	0.50	0.20	-0.20	0.10	1.499	0.02	3.6
τ_{mhd} available	2	-0.40	-0.10	0.35	**0.80**	-0.05	0.35	0.05	0.375	0.11	5.3
691 obs.	3	0.25	0.00	**0.90**	-0.25	-0.20	-0.10	0.05	0.279	0.17	2.1
	4	0.25	-0.50	-0.05	-0.20	0.25	0.55	0.55	0.170	0.08	-0.4
	5	0.05	0.65	0.10	-0.15	0.30	0.60	-0.25	0.099	0.14	3.8
	6	0.00	0.45	-0.15	0.00	-0.65	0.10	0.60	0.066	0.17	-3.3
	7	-0.35	0.30	0.15	-0.05	**0.60**	-0.35	0.55	0.060	0.19	1.3
ELM-free	1	**0.75**	0.20	-0.05	0.55	0.20	-0.20	0.10	1.708	0.02	3.1
τ_{dia} available	2	-0.45	0.00	0.40	**0.75**	-0.15	0.10	-0.10	0.317	0.14	5.8
489 obs.	3	0.30	-0.05	**0.90**	-0.30	-0.15	0.00	0.10	0.280	0.17	2.3
	4	-0.05	**0.90**	0.10	-0.15	-0.05	0.05	-0.40	0.128	0.10	0.5
	5	0.05	0.30	-0.15	0.05	**-0.75**	0.05	0.60	0.060	0.20	-4.1
	6	-0.35	0.30	0.15	-0.05	0.55	-0.30	0.60	0.051	0.23	-0.6
	7	0.10	0.05	0.00	0.00	0.30	0.90	0.25	0.034	0.29	17.3

Table IV *Principal components for different subsets of the standard dataset (Coefficient ≥ 0.7 are typed in bold-face). In addition the standard deviation STD of the data along each principal direction and the two yardsticks ERR and ITER as defined in the text are given.*

	Subset	p.c.	Log (I_p)	Log (B_T)	Log (n)	Log (P_L)	Log (R)	Log (1/ε)	Log (κ)	STD	ERR	ITER
(a)	W. ELMS, τ_{mhd} avail. 548 obs.	5	-0.35	-	-	0.00	0.65	-0.55	0.40	0.067	0.12	-1.4
	W. ELMS, τ_{dia} avail. 360 obs	5	-0.10	-	-	0.10	0.40	**0.70**	0.55	0.036	0.29	16.5
	ELM-free, τ_{mhd} avail. 691 obs.	5	-0.35	-	-	0.05	0.35	-0.55	0.70	0.072	0.14	-2.5
	ELM-free, τ_{dia} avail. 489 obs.	5	0.10	-	-	0.00	0.30	**0.95**	0.15	0.034	0.28	17.4
(b)	ELMs and ELM-free, τ_{mhd} avail. 1239 obs.	6	-0.20	0.55	-0.10	0.05	-0.35	-0.15	**0.70**	0.081	0.13	-3.1
		7	-0.35	-0.05	0.15	0.00	**0.75**	-0.50	0.25	0.066	0.16	0.9
	ELMs and ELM-free, τ_{dia} avail. 849 obs	6	0.00	0.20	0.05	0.05	0.20	**0.85**	0.40	0.056	0.19	12.6
		7	-0.35	0.20	0.15	-0.05	**0.70**	-0.40	0.45	0.053	0.22	1.4
	ELMs and ELM-free, τ_{mhd} avail. 1239 obs.	4	0.05	-	-	-0.10	**0.80**	0.45	-0.40	0.141	0.06	3.0
		5	-0.40	-	-	0.05	0.60	-0.55	0.40	0.074	0.12	-1.8
	ELMs and ELM-free, τ_{dia} avail. 849 obs.	4	-0.30	-	-	0.05	**0.80**	0.00	0.50	0.080	0.09	3.1
		5	0.15	-	-	0.10	0.00	**0.98**	0.10	0.056	0.19	12.4
(c)	ELMs and ELM-free, τ_{mhd} avail. 8584obs.	6	-0.25	-0.05	0.25	0.00	**0.85**	-0.35	-0.20	0.064	0.21	4.0
		7	-0.15	0.15	0.00	-0.05	0.15	-0.10	**0.96**	0.036	0.29	-3.2
	ELMs and ELM-free, τ_{dia} avail. 593 obs	6	-0.30	0.15	0.15	-0.10	0.60	-0.65	0.30	0.054	0.24	-2.6
		7	0.00	0.05	-0.05	0.00	0.00	0.45	**0.90**	0.020	0.50	10.3
	ELMs and ELM-free, τ_{mhd} avail. 854 obs.	4	0.35	-	-	-0.10	**-0.75**	0.50	0.20	0.092	0.09	-0.2
		5	-0.15	-	-	-0.05	0.15	-0.10	**0.97**	0.038	0.27	-4.0
	ELMs and ELM-free, τ_{dia} avail. 593 obs.	4	0.25	-	-	0.05	-0.20	**0.85**	-0.40	0.064	0.16	8.9
		5	0.00	-	-	0.00	0.10	0.45	**0.90**	0.021	0.47	11.3

Table V *Selected p.c.'s from principal component analysis on different subsets (coefficients ≥0.7 are typed in bold-face).*

(a) The smallest principal component p.c. 5 for the indicated subsets of the standard dataset with the variables B_T and n omitted.

(b) The two smallest p.c.'s for the indicated subsets of the standard dataset with and without the variables B_T and n.

(c) The two smallest p.c.'s for the indicated subsets of the open divertor tokamak subset with and without the variables B_T and n.

Subset	p.c.	Log (I_p)	Log (B_T)	Log (n)	Log (P_L)	Log (R)	Log (1/ε)	STD	ERR	ITER
With ELMS	1	**0.80**	0.25	-0.05	0.45	0.15	-0.30	1.160	0.02	4.0
τ_{mhd} avail.	2	-0.25	-0.10	0.65	0.65	-0.15	0.10	0.514	0.09	3.6
203 obs.	3	-0.25	0.00	-0.65	0.55	0.30	0.40	0.303	0.14	3.0
	4	0.30	0.20	0.35	-0.20	0.40	**0.75**	0.183	0.12	5.0
	5	-0.30	**0.95**	0.00	0.00	-0.10	-0.10	0.109	0.09	-0.8
	6	-0.25	-0.05	0.20	-0.05	**0.85**	-0.40	0.049	0.25	5.1
With ELMS	1	**0.70**	0.20	0.00	0.60	0.20	-0.15	1.115	0.03	4.1
τ_{dia} avail.	2	-0.30	-0.15	**0.75**	0.50	-0.30	-0.05	0.556	0.08	2.1
120 obs.	3	0.50	0.10	0.60	-0.60	0.00	0.05	0.297	0.15	-0.8
	4	-0.25	**0.95**	0.05	0.00	0.00	0.25	0.142	0.07	1.7
	5	0.10	-0.20	0.00	0.15	0.10	**0.95**	0.061	0.20	12.4
	6	-0.25	-0.05	0.25	0.00	**0.95**	-0.10	0.045	0.30	11.3
ELM-free	1	**0.75**	0.20	-0.05	0.50	0.20	-0.20	1.530	0.02	3.5
τ_{mhd} avail.	2	-0.40	-0.10	0.30	**0.80**	-0.05	0.35	0.383	0.11	5.2
651 obs.	3	0.20	0.00	**0.90**	-0.20	-0.20	-0.15	0.277	0.17	2.4
	4	0.35	-0.30	0.05	-0.20	0.35	**0.80**	0.128	0.12	1.7
	5	-0.10	**0.90**	0.05	-0.10	0.00	0.35	0.086	0.13	2.7
	6	-0.30	0.05	0.25	-0.05	**0.90**	-0.30	0.062	0.21	4.2
ELM-free	1	**0.75**	0.20	-0.05	0.55	0.20	-0.20	1.723	0.02	3.0
τ_{dia} avail.	2	-0.45	-0.05	0.45	**0.75**	-0.15	0.10	0.314	0.14	6.0
473 obs.	3	0.35	0.00	**0.85**	-0.35	-0.15	0.00	0.275	0.17	1.9
	4	-0.15	**0.97**	0.00	-0.05	-0.15	0.10	0.102	0.10	0.6
	5	-0.25	0.10	0.25	-0.10	**0.90**	-0.15	0.054	0.24	5.0
	6	0.15	-0.05	0.00	0.00	0.20	**0.96**	0.036	0.28	16.4

Table VI *Principal components for different open divertor tokamak subsets and κ omitted. The standard deviation STD of each p.c. and the two yardsticks ERR and ITER as defined in the text are given.*

Subset	p.c.	Log (I_p)	Log (B_T)	Log (n)	Log (P_L)	Log (R)	Log ($1/\varepsilon$)	Log (κ)	STD	ERR	ITER
With ELMs	1	0.65	0.00	0.35	0.60	0.05	-0.15	0.25	0.772	0.05	7.3
τ_{mhd} avail.	2	-0.35	-0.45	0.55	0.10	0.00	0.50	0.30	0.311	0.09	-2.7
506 obs.	3	-0.45	0.25	-0.25	**0.75**	0.10	0.20	-0.25	0.277	0.15	5.0
	4	-0.05	0.65	0.65	-0.15	0.15	0.05	-0.35	0.198	0.18	1.9
	5	0.20	0.45	-0.30	-0.15	0.30	0.55	0.50	0.148	0.13	5.6
	6	-0.45	0.15	0.10	0.00	0.30	-0.60	0.55	0.069	0.15	-8.1
	7	0.15	-0.35	-0.05	-0.05	**0.90**	0.00	-0.25	0.041	0.17	23.2
With ELMs	1	**0.70**	0.00	0.30	0.55	0.00	-0.20	0.25	0.830	0.04	6.8
τ_{dia} avail.	2	-0.35	0.30	-0.30	**0.75**	0.10	0.05	-0.35	0.317	0.13	5.0
318 obs.	3	-0.05	0.40	**0.80**	-0.10	0.05	0.20	-0.40	0.188	0.21	1.6
	4	0.50	0.65	-0.45	-0.25	0.15	0.00	-0.15	0.129	0.21	8.4
	5	-0.40	0.45	0.15	-0.05	0.10	-0.60	0.50	0.059	0.20	-8.8
	6	-0.05	0.30	0.00	0.10	-0.50	0.60	0.50	0.049	0.21	-2.5
	7	-0.05	-0.05	0.00	0.00	**0.85**	0.40	0.35	0.016	0.44	62.2

Table VII *Principal components for subsets with ELMs of the standard dataset with the JET data omitted. The standard deviation STD of each p.c. and the two yardsticks ERR and ITER as defined in the text are given.*

L-mode Scaling	Mean	Std. Dev. (%)	Min.	Max.
Goldston	1.65	28.8	0.45	2.05
Kaye Big	2.02	25.9	0.40	1.91
ITER89-P	2.11	21.8	0.43	1.91
Rebut-Lallia	2.35	42.4	0.34	2.35

Table VIII *H-mode enhancement factors (Mean) for different L-mode scalings obtained from the standard dataset. For Rebut-Lallia scaling Fr = 2.0 and Zeff = 3. The standard deviation and range of the ratio* $\tau_E/(\text{Mean} \times \tau_{L\text{-mode}})$ *are given as well.*

Tokamak	Observations	σ(%)	α_I	α_B	α_n	α_P	α_A
ASDEX (MHD)	256	11.5	0.90 (0.08)	-0.11 (0.16)	-0.06 (0.05)	-0.51 (0.04)	-
ASDEX (Dia)	256	10.1	0.90 (0.08)	-0.19 (0.16)	0.14 (0.05)	-0.52 (0.04)	-
JET (MHD)	286	12.1	-0.05 (0.12)	0.81 (0.16)	0.64 (0.10)	-0.58 (0.09)	-
JET (Dia)	286	8.3	0.43 (0.03)	0.53 (0.05)	0.48 (0.03)	-0.61 (0.03)	-
JFT2M (MHD)	231	7.7	0.83 (0.09)	0.51 (0.61)	0.10 (0.08)	-0.68 (0.04)	0.10 (0.09)
JFT2M (Dia)	231	10.3	0.58 (0.09)	0.69 (0.61)	0.24 (0.08)	-0.67 (0.04)	0.16 (0.09)

Table IX *Individual regression results for ASDEX and JET, and JFT-2M using either τ_{mhd} or τ_{dia}. Entries in parantheses are one standard deviation uncertainties in regressor variables. Estimated uncertainties in measured τ_E are listed in Appendix III. A "-" entry for α_A indicates the mass scaling could not be determined because the data contained only one effective mass.*

Tokamak	Observations	σ (%)	α_I	α_B	α_n	α_P	α_A
ASDEX (MHD-like)	256	9.4	0.83 (0.08)	-0.20 (0.16)	-0.08 (0.05)	-0.50 (0.04)	-
DIII-D (MHD)	121	15.0	1.00 (0.11)	0.10 (0.17)	-0.21 (0.10)	-0.52 (0.04)	0.60 (0.09)
JET (DIA)	286	8.3	0.43 (0.06)	0.53 (0.08)	0.48 (0.05)	-0.61 (0.04)	-
JFT2M (MHD)	231	7.7	0.83 (0.09)	0.51 (0.61)	0.10 (0.08)	-0.68 (0.04)	0.10 (0.09)
PBXM (MHD)	216	9.9	0.49 (0.27)	1.59 (0.55)	-0.32 (0.07)	-0.34 (0.07)	-
PDX (MHD)[a]	129	17.0	1.34 (0.18)	0.39 (0.16)	0.04 (0.07)	-0.48 (0.10)	1.07 (0.14)

Table X *Individual regression results for ASDEX, DIII-D, JET, JFT2M, PBXM and PDX. Entries in parentheses are one standard deviation uncertainties in regressor variables. Estimated uncertainties in measured τ_E are listed in Appendix III.*

[a] The ratio of the D_α emission in the divertor to that in the midplane, as an indicator of compression ratio, was determined to be an important parameter, as discussed in Appendix I. Including this parameter changes the I and B scaling somewhat, but has little effect on the other regression coefficients.

Category [Observations]	α_I	α_B	α_n	α_P	α_ϵ	α_R	α_κ	χ^2
Standard dataset [1239]	0.55 (0.03)	0.91 (0.04)	0.17 (0.02)	–0.55 (0.01)	–0.19 (0.04)	2.30 (0.06)	0.70 (0.05)	956
Thermal analysis [964]	0.77 (0.03)	0.49 (0.05)	0.30 (0.03)	–0.71 (0.02)	-0.26 (0.05)	2.28 (0.07)	0.38 (0.05)	595
ELM-free [691]	0.74 (0.04)	0.69 (0.07)	0.09 (0.03)	–0.54 (0.02)	–0.06 (0.06)	1.91 (0.09)	0.70 (0.09)	409
ELMs [548]	0.38 (0.04)	0.96 (0.05)	0.20 (0.03)	–0.52 (0.02)	–0.41 (0.07)	2.55 (0.10)	0.80 (0.07)	478

Table XI *Results of regression analysis on standard dataset and different subsets ($\alpha_A \equiv 0.50$ for all cases). χ^2 is defined as the minimum sum of the square of the observed τ_E minus the calculated τ_E divided by the uncertainty.*

Category [Observations]	α_I	α_B	α_n	α_P	α_ϵ	α_R	α_κ	χ^2
ELM-free [691]	0.74 (0.04)	0.69 (0.07)	0.09 (0.03)	–0.54 (0.02)	–0.06 (0.06)	1.91 (0.09)	0.70 (0.09)	409
	0.91 (0.04)	0	0.08 (0.03)	–0.49 (0.02)	-0.14 (0.06)	1.93 (0.09)	0.27 (0.07)	503
	0.87 (0.04)	0.15 (0.0)	0.08 (0.03)	–0.50 (0.02)	–0.12 (0.06)	1.92 (0.09)	0.36 (0.07)	467
	0.84 (0.04)	0.30 (0.0)	0.09 (0.03)	–0.52 (0.02)	–0.10 (0.06)	1.92 (0.09)	0.46 (0.07)	439

Table XII *Results from regression on the ELM-free subset with different constraints on α_B ($\alpha_A \equiv 0.50$ for all cases).*

Model	NC	MHD τ_E	Dia τ_E	MHD τ_{th}	Dia τ_{th}	H τ_{th}	ELM τ_{th}
Unconstrained	0	16.85	12.69	19.09	15.34	12.42	15.78
High-β coll.	1	16.91	12.69	19.45	15.49	12.43	15.77
Gyro-Bohm	2	16.92	12.80	20.55	16.25	12.66	16.59
Bohm	2	18.84	13.78	22.95	18.35	13.89	18.76
Res. MHD	2	19.92	14.73	24.88	20.08	15.25	20.41
Ideal MHD	3	21.31	16.38	25.01	20.18	15.45	20.49

Table XIII *The rms error obtained for various theoretical transport models by fits to τ_{mhd}, τ_{dia} as well as τ_{th} derived from MHD and diamagnetic data. The last two columns refer to τ_{th} derived from diamagnetic data for phase H only (693 obs) and for phases HSELM , HGELM only (551 obs). NC denotes the number of constraints.*

Model	NC	τ_B	ρ/a	ν*	β	ε	κ	A	q
Unconstrained	0	0.68	−2.21	−0.08	−1.38	−7.46	−1.58	1.13	2.39
High-β coll.	1	1	−1.77	−0.12	−1.33	−7.49	−1.53	1.16	2.19
Gyro-Bohm	2	1	−1	−0.15	−1.30	−5.58	−0.53	1.29	1.77

Table XIV *Exponents x1-x8 of Eq. (11) obtained from fits to τ_{th} derived from diamagnetic data in the ELM free dataset (693 obs.) for various transport models. NC denotes the number of contraints.*

Definition of Plasma Shape Parameters

$\varepsilon = a/R$ (inverse aspect ratio)

$\kappa = b/a$ (elongation)

$\delta = c/a$ (triangularity)

$i = d/2a$ (indentation)

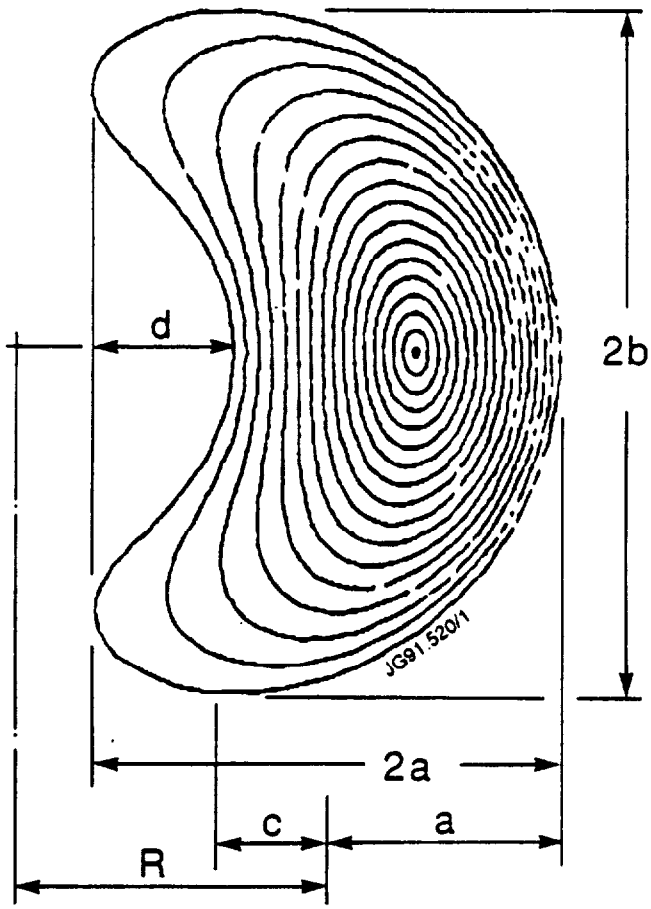

Figure 1

Fig.2

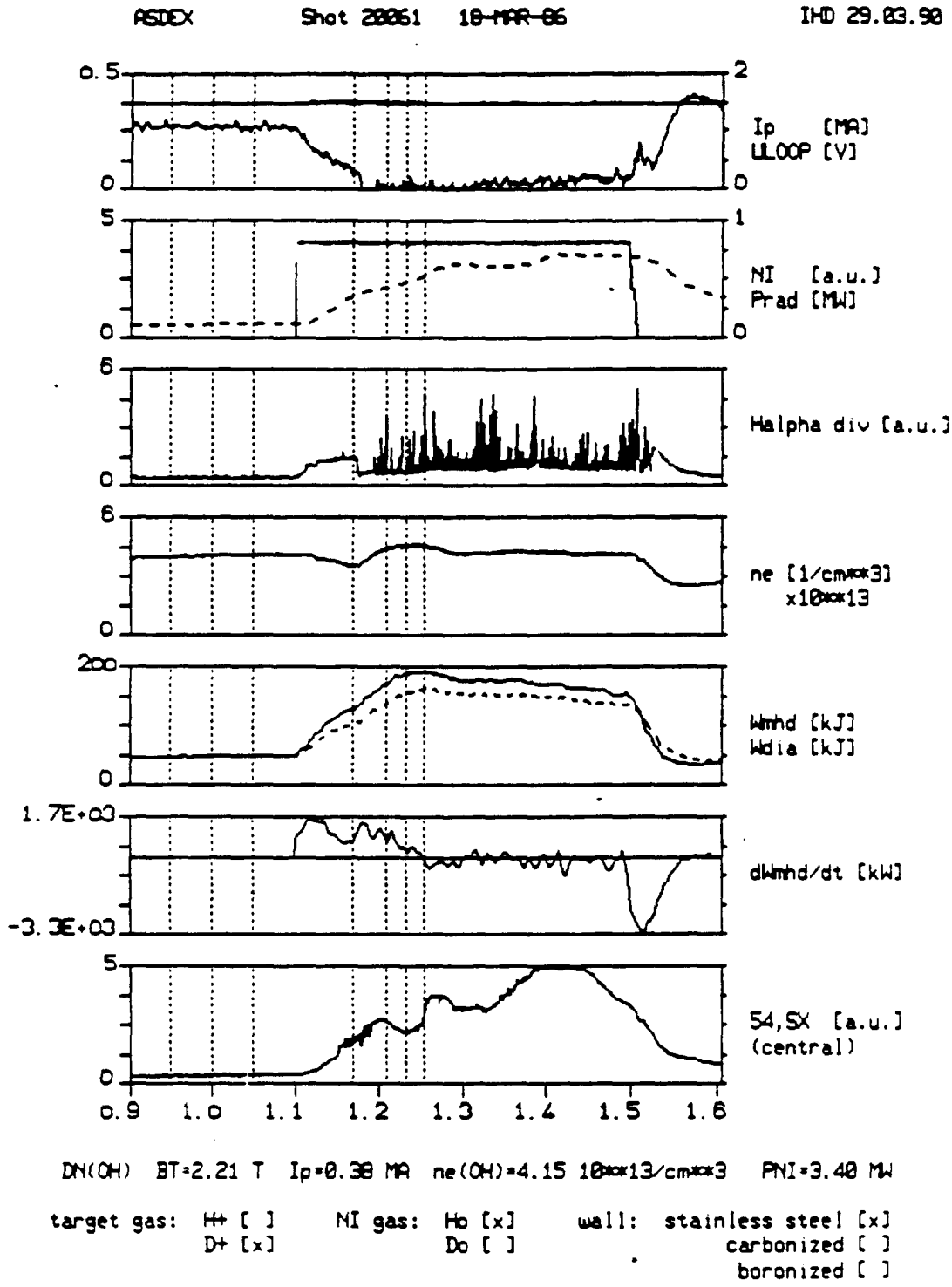
ASDEX
Shot 28061
18-MAR-86
IHD 29.03.98
0.5
0
2
0
Ip [MA]
ULOOP [V]
5
0
1
0
NI [a.u.]
Prad [MW]
6
0
Halpha div [a.u.]
6
0
ne [1/cm**3]
x10**13
200
0
Wmhd [kJ]
Wdia [kJ]
1.7E+03
-3.3E+03
dWmhd/dt [kW]
5
0
54,SX [a.u.]
(central)
0.9
1.0
1.1
1.2
1.3
1.4
1.5
1.6
DN(OH) BT=2.21 T Ip=0.38 MA ne(OH)=4.15 10**13/cm**3 PNI=3.40 MW
target gas: H+ [ ] D+ [x]
NI gas: Ho [x] Do [ ]
wall: stainless steel [x]
carbonized [ ]
boronized [ ]

Fig.3

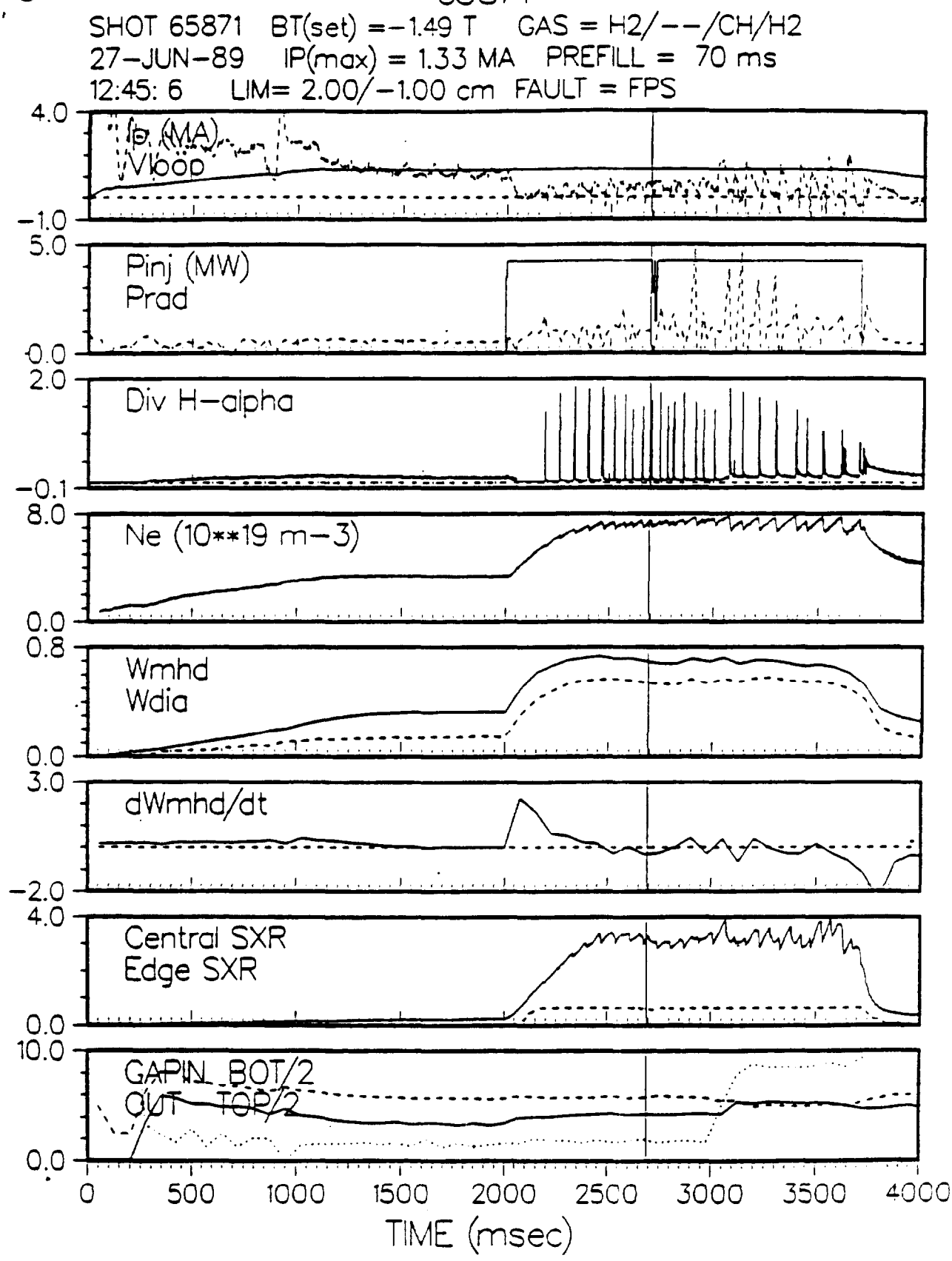
65871
SHOT 65871 BT(set) =−1.49 T GAS = H2/−−/CH/H2
27−JUN−89 IP(max) = 1.33 MA PREFILL = 70 ms
12:45: 6 LIM= 2.00/−1.00 cm FAULT = FPS
4.0
Ip (MA)
Vloop
−1.0
5.0
Pinj (MW)
Prad
0.0
2.0
Div H−alpha
−0.1
8.0
Ne (10**19 m−3)
0.0
0.8
Wmhd
Wdia
0.0
3.0
dWmhd/dt
−2.0
4.0
Central SXR
Edge SXR
0.0
10.0
GAPIN_BOT/2
OUT_TOP/2
0.0
0
500
1000
1500
2000
2500
3000
3500
4000
TIME (msec)

Fig.4

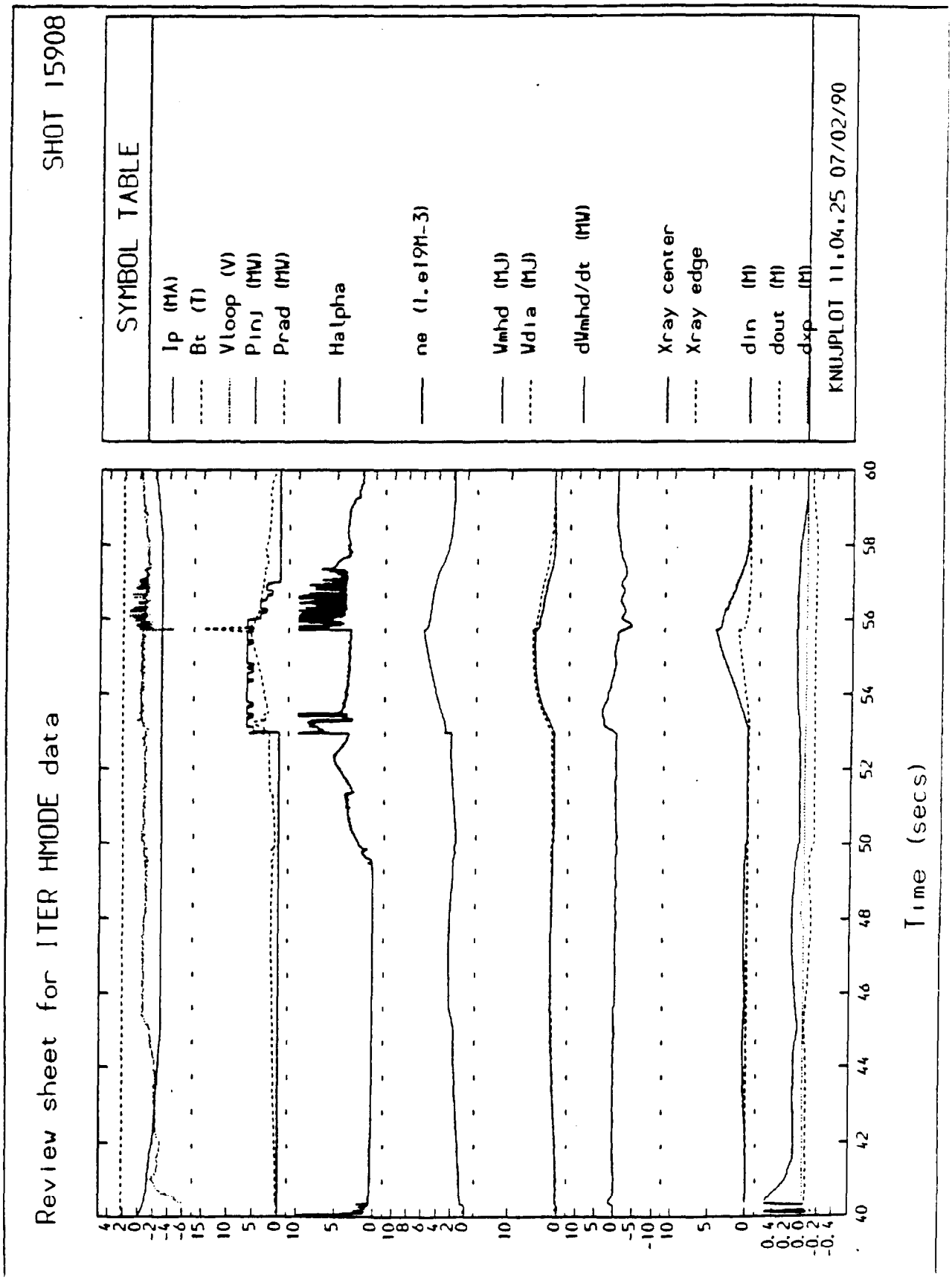
Review sheet for ITER HMODE data
SHOT 15908
SYMBOL TABLE
Ip (MA)
Bt (T)
Vloop (V)
Pinj (MW)
Prad (MW)
Halpha
ne (1.e19M-3)
Wmhd (MJ)
Wdia (MJ)
dWmhd/dt (MW)
Xray center
Xray edge
din (M)
dout (M)
dxp (M)
KNUJPLOT 11.04.25 07/02/90
Time (secs)

Fig.5

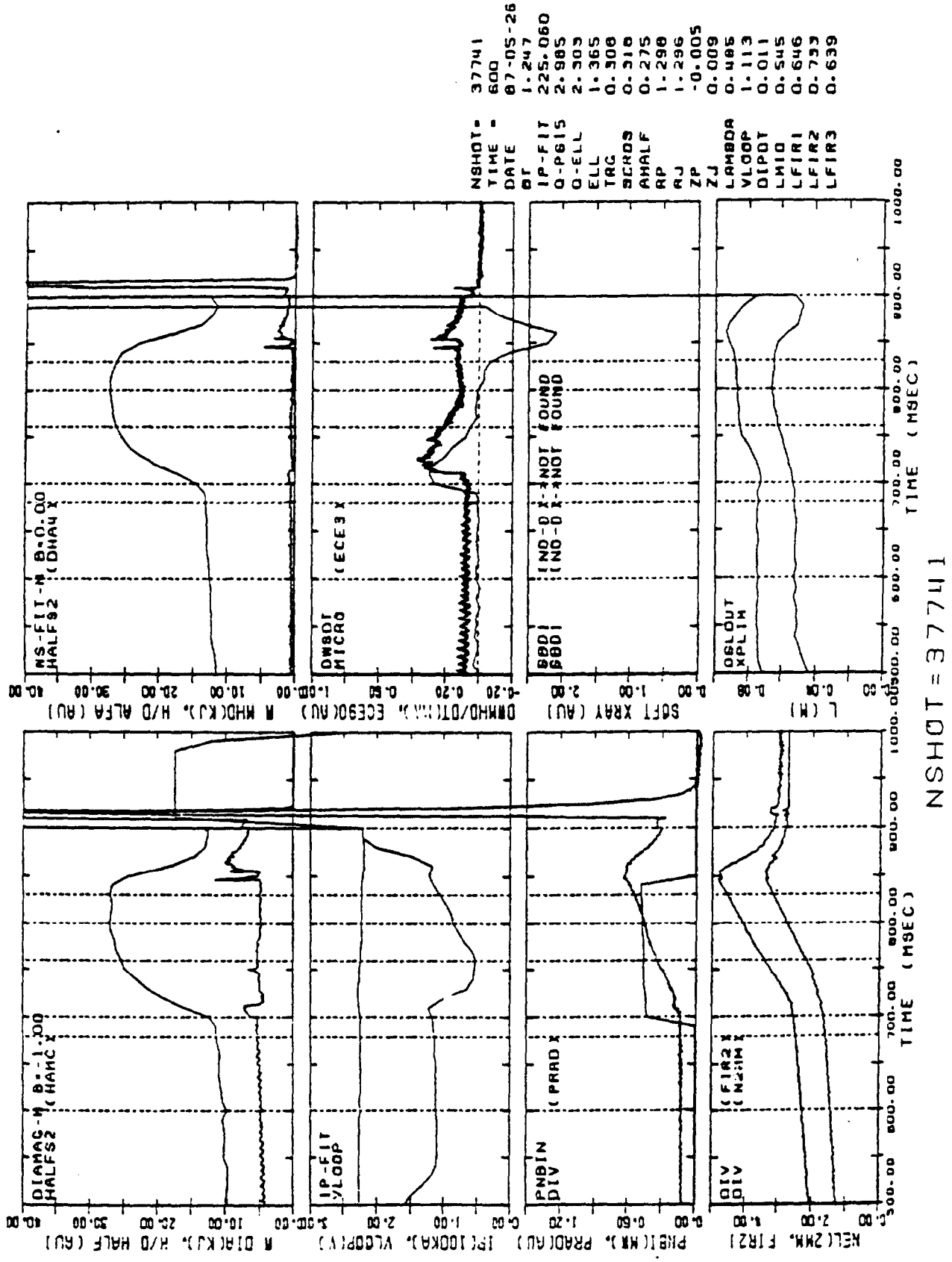
NSHOT= 37741
TIME = 600
DATE 87-05-26
BT 1.247
IP-FIT 225.060
Q-PSI5 2.985
Q-ELL 2.303
ELL 1.365
TRG 0.308
SCROS 0.318
AHALF 0.275
RP 1.298
RJ 1.296
ZP -0.005
ZJ 0.009
LAMBDA 0.485
VLOOP 1.113
DIPOT 0.011
LMIO 0.545
LFIR1 0.646
LFIR2 0.799
LFIR3 0.639
NSHOT=37741
TIME (MSEC)

Fig.6

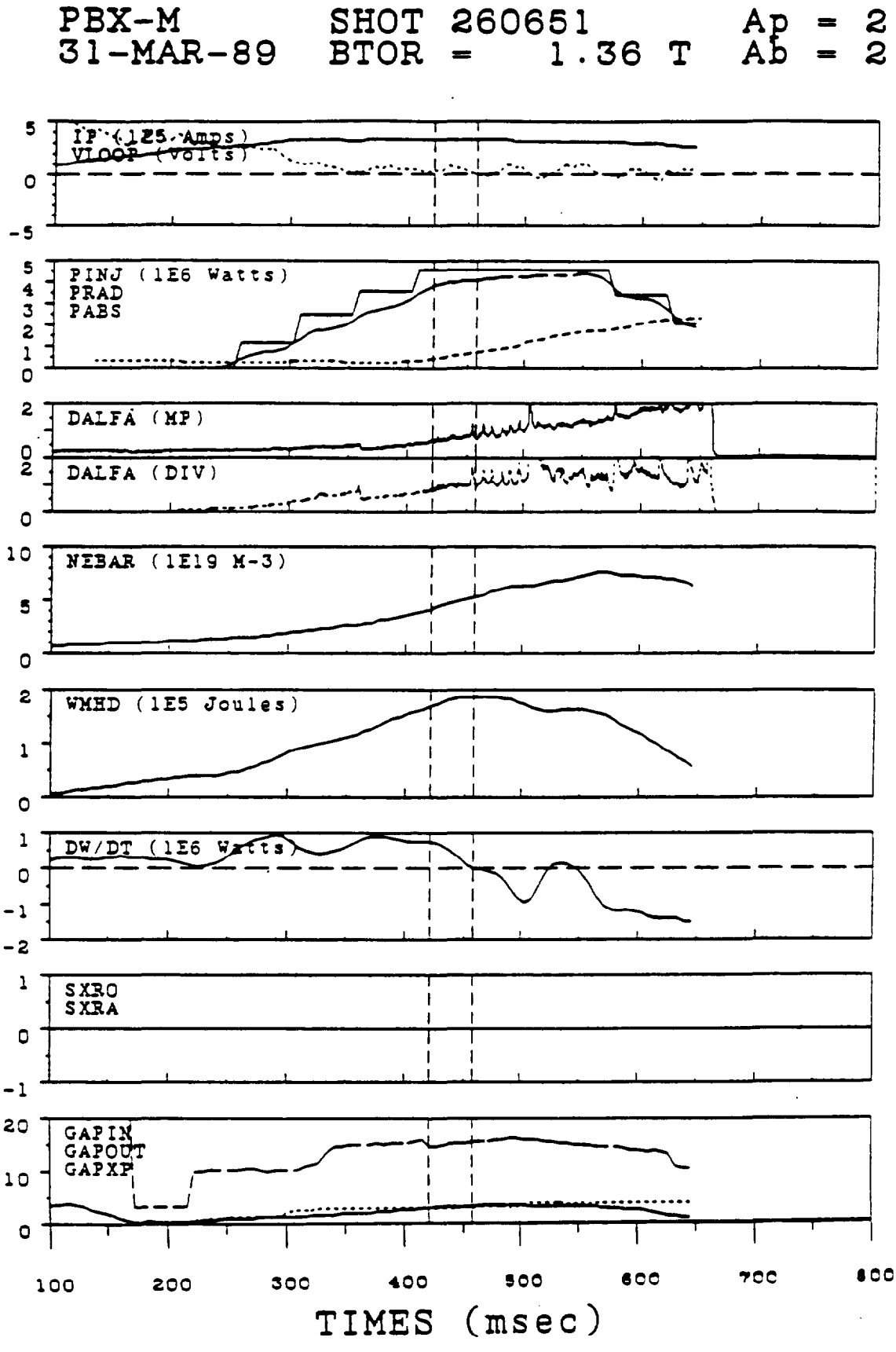
PBX-M SHOT 260651 Ap = 2
31-MAR-89 BTOR = 1.36 T Ab = 2
IP (1E5 Amps)
VLOOP (Volts)
PINJ (1E6 Watts)
PRAD
PABS
DALFA (MF)
DALFA (DIV)
NEBAR (1E19 M-3)
WMHD (1E5 Joules)
DW/DT (1E6 Watts)
SXRO
SXRA
GAPIN
GAPOUT
GAPXP
100
200
300
400
500
600
700
800
TIMES (msec)

Fig.7

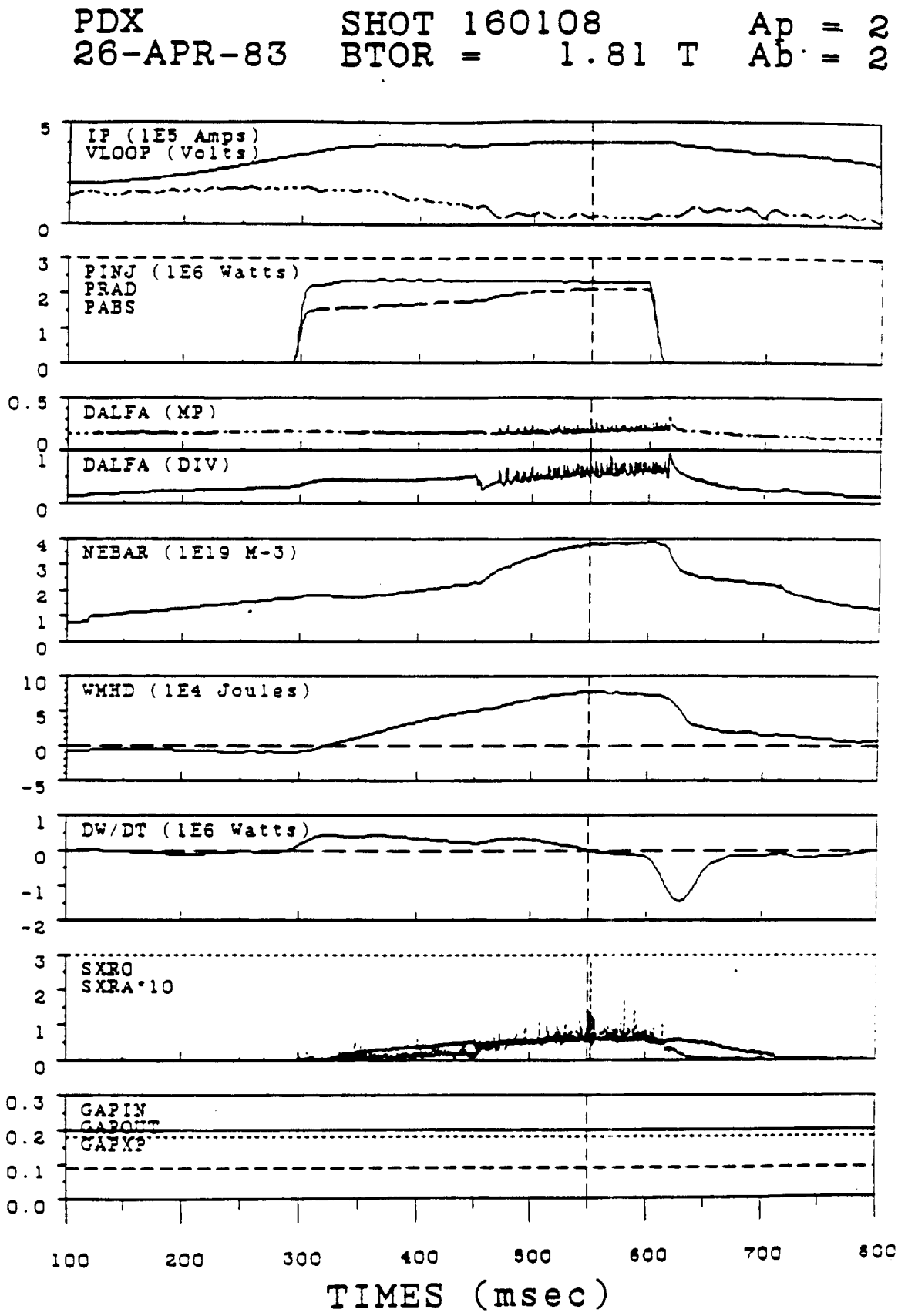
PDX SHOT 160108 Ap = 2
26-APR-83 BTOR = 1.81 T Ab = 2
IP (1E5 Amps)
VLOOP (Volts)
PINJ (1E6 Watts)
PRAD
PABS
DALFA (MP)
DALFA (DIV)
NEBAR (1E19 M-3)
WMHD (1E4 Joules)
DW/DT (1E6 Watts)
SXRC
SXRA*10
GAPIN
GAPOUT
GAPX?
TIMES (msec)

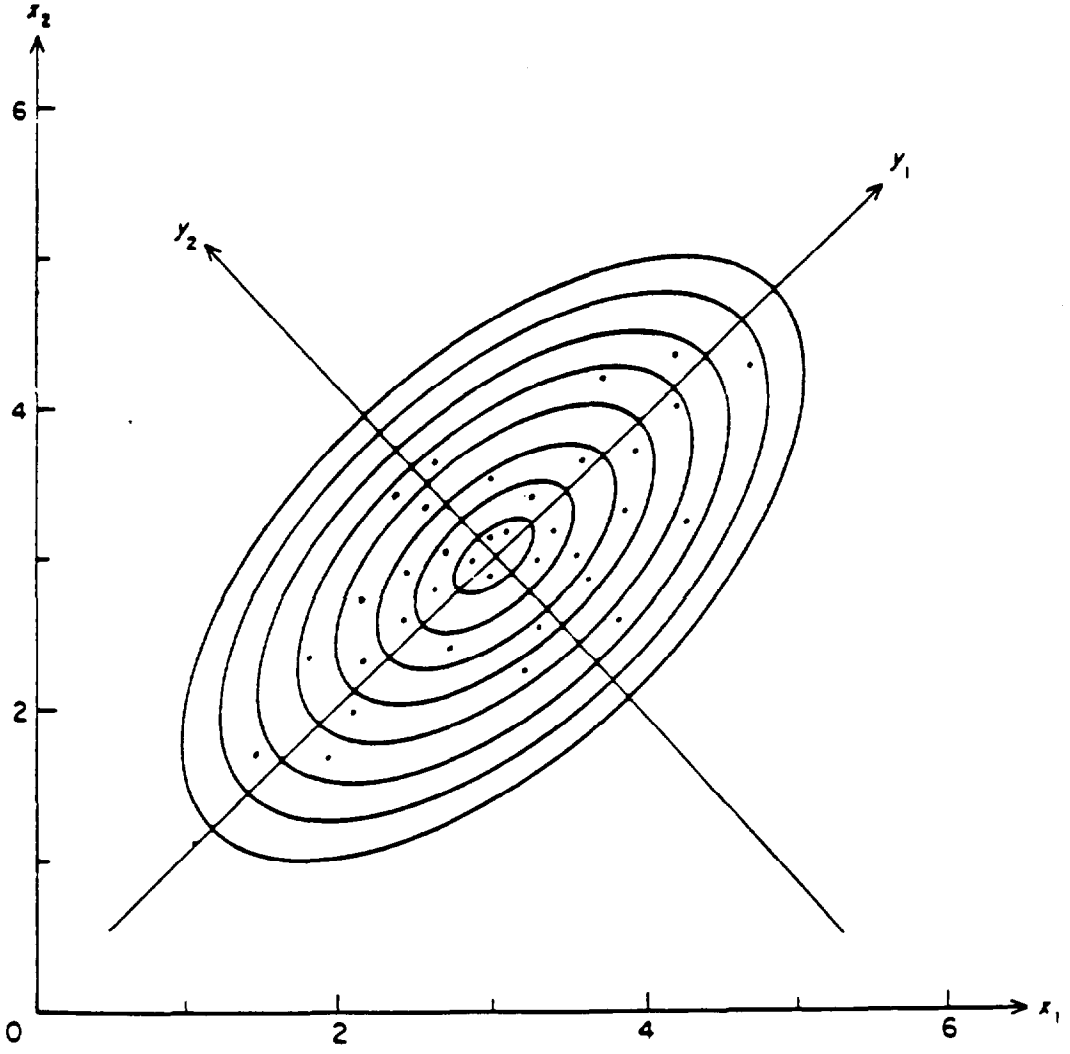

Figure 8

Fig.9a

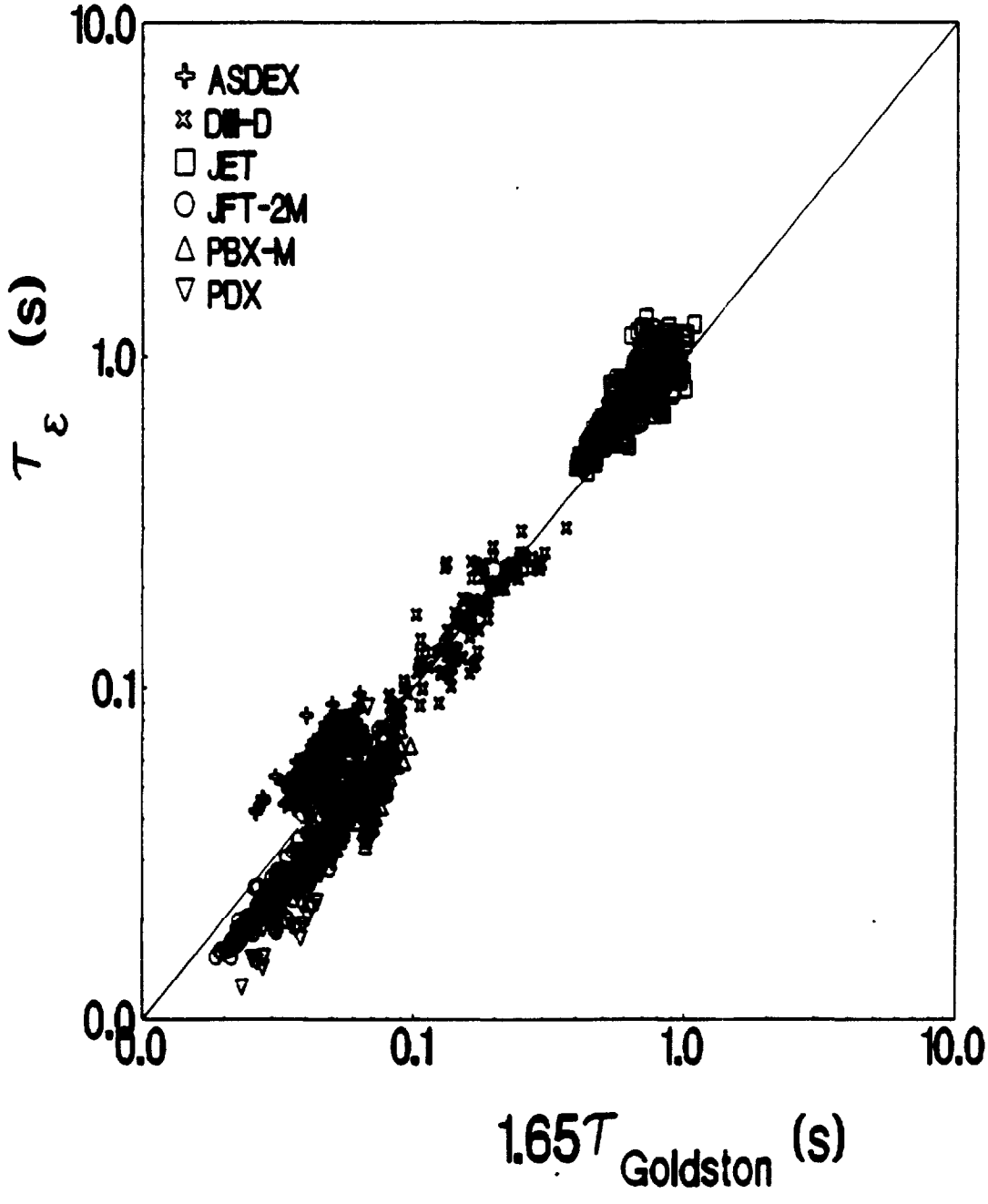
10.0
1.0
0.1
0.0
0.0
0.1
1.0
10.0
ASDEX
DIII-D
JET
JFT-2M
PBX-M
PDX
τ_ε (s)
$1.65\tau_{Goldston}$ (s)

Fig.9b

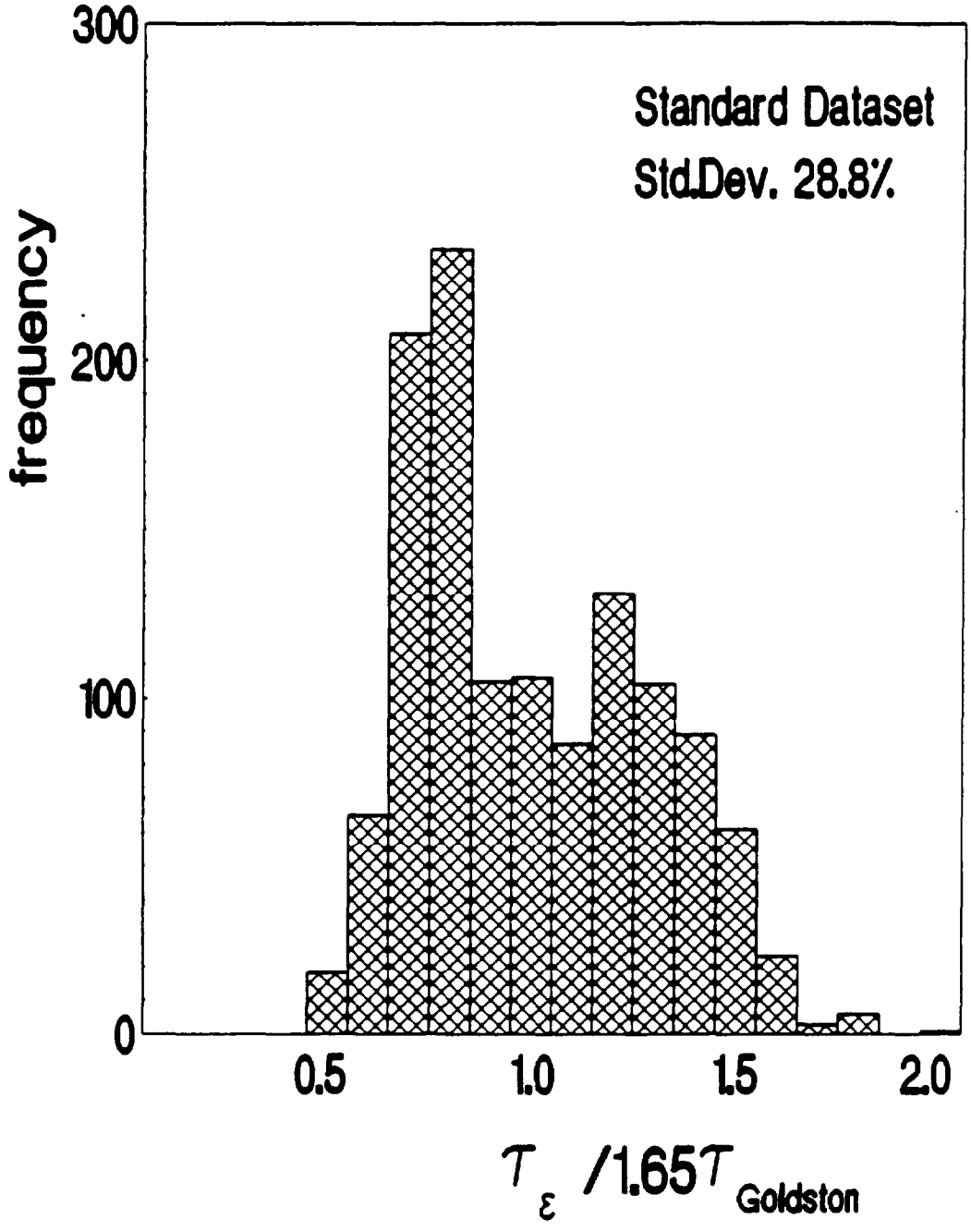
300
200
100
0
frequency
Standard Dataset
Std.Dev. 28.8%
0.5
1.0
1.5
2.0
τ_ε /1.65$\tau_{Goldston}$

Fig.10a

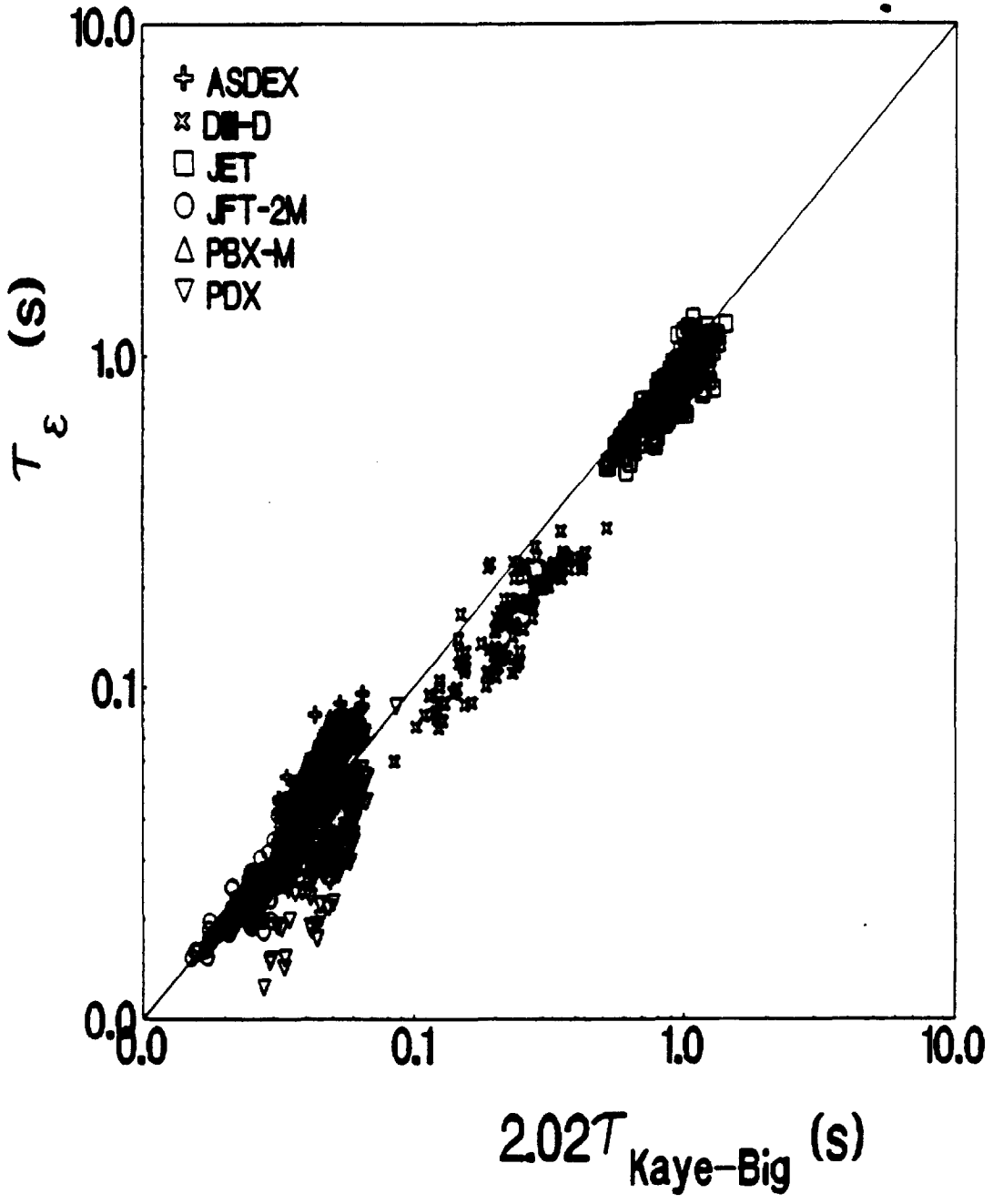
10.0
1.0
0.1
0.0
0.0
0.1
1.0
10.0
ASDEX
DIII-D
JET
JFT-2M
PBX-M
PDX
τ_ε (s)
$2.02\tau_{Kaye-Big}$ (s)

Fig.10b

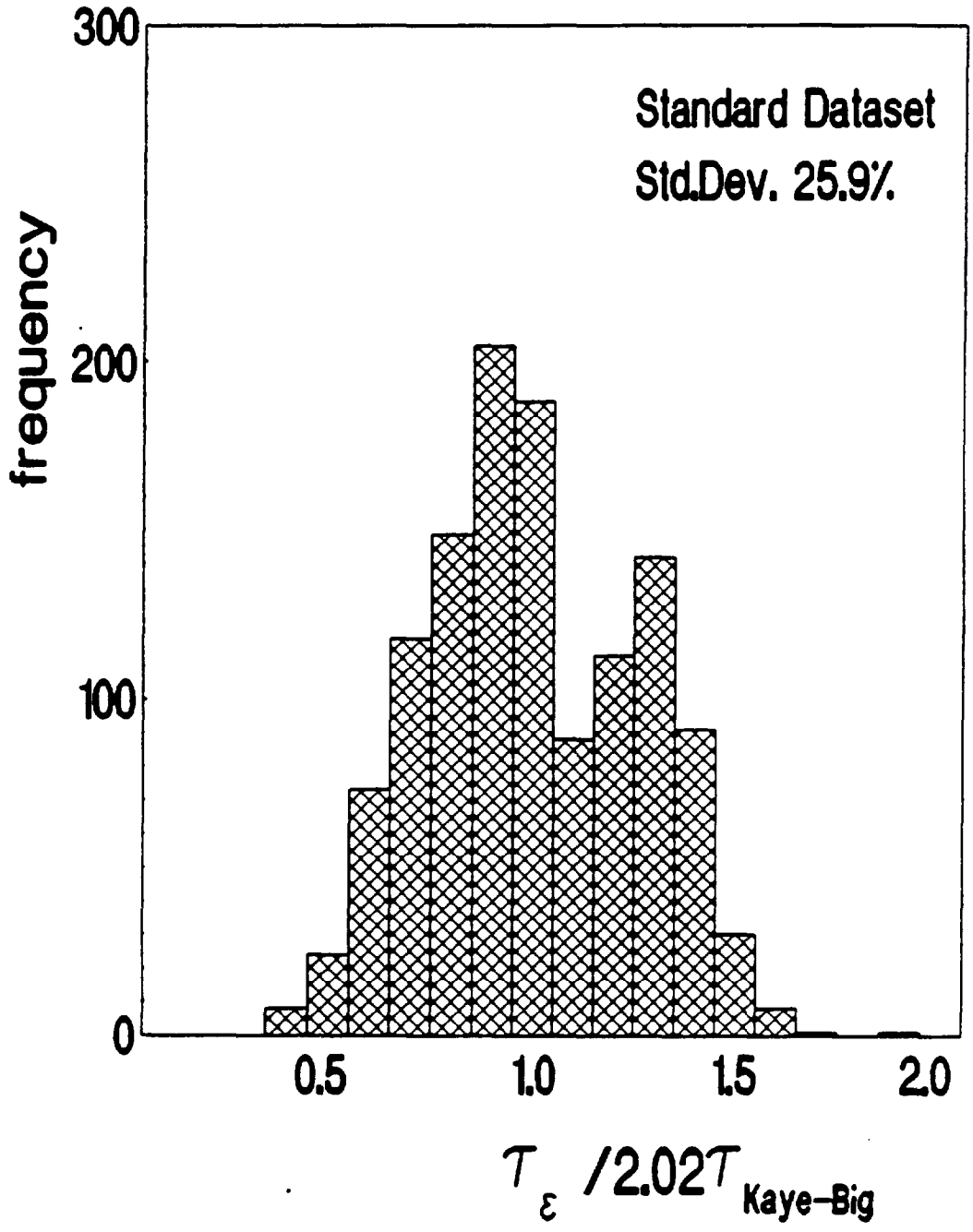
300
200
100
0
frequency
Standard Dataset
Std.Dev. 25.9%
0.5
1.0
1.5
2.0
τ_ε /2.02$\tau_{Kaye-Big}$

Fig.11a

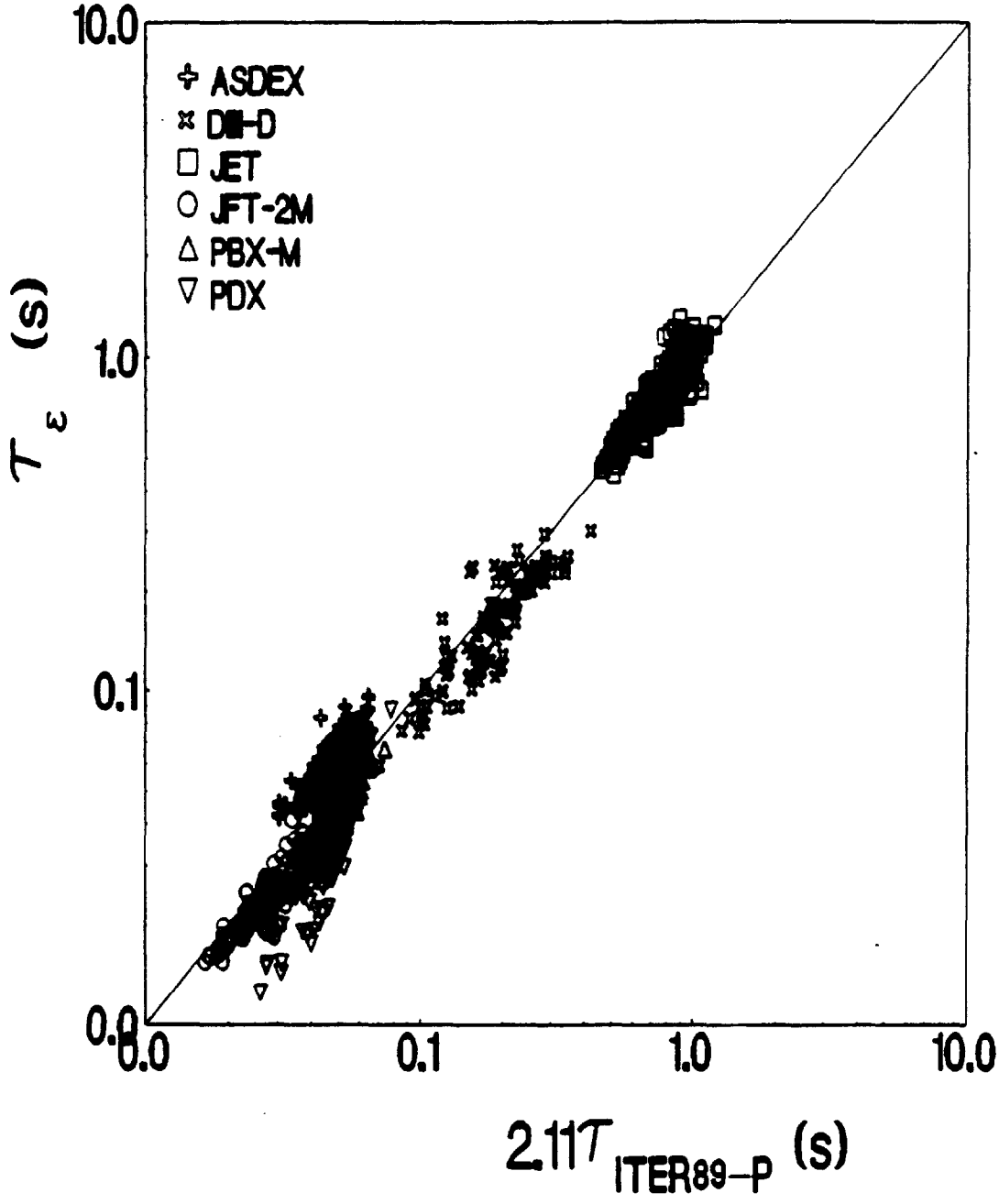
10.0
1.0
0.1
0.0
0.0
0.1
1.0
10.0
ASDEX
DIII-D
JET
JFT-2M
PBX-M
PDX
τ_ε (s)
$2.11\tau_{ITER89-P}$ (s)

Fig.11b

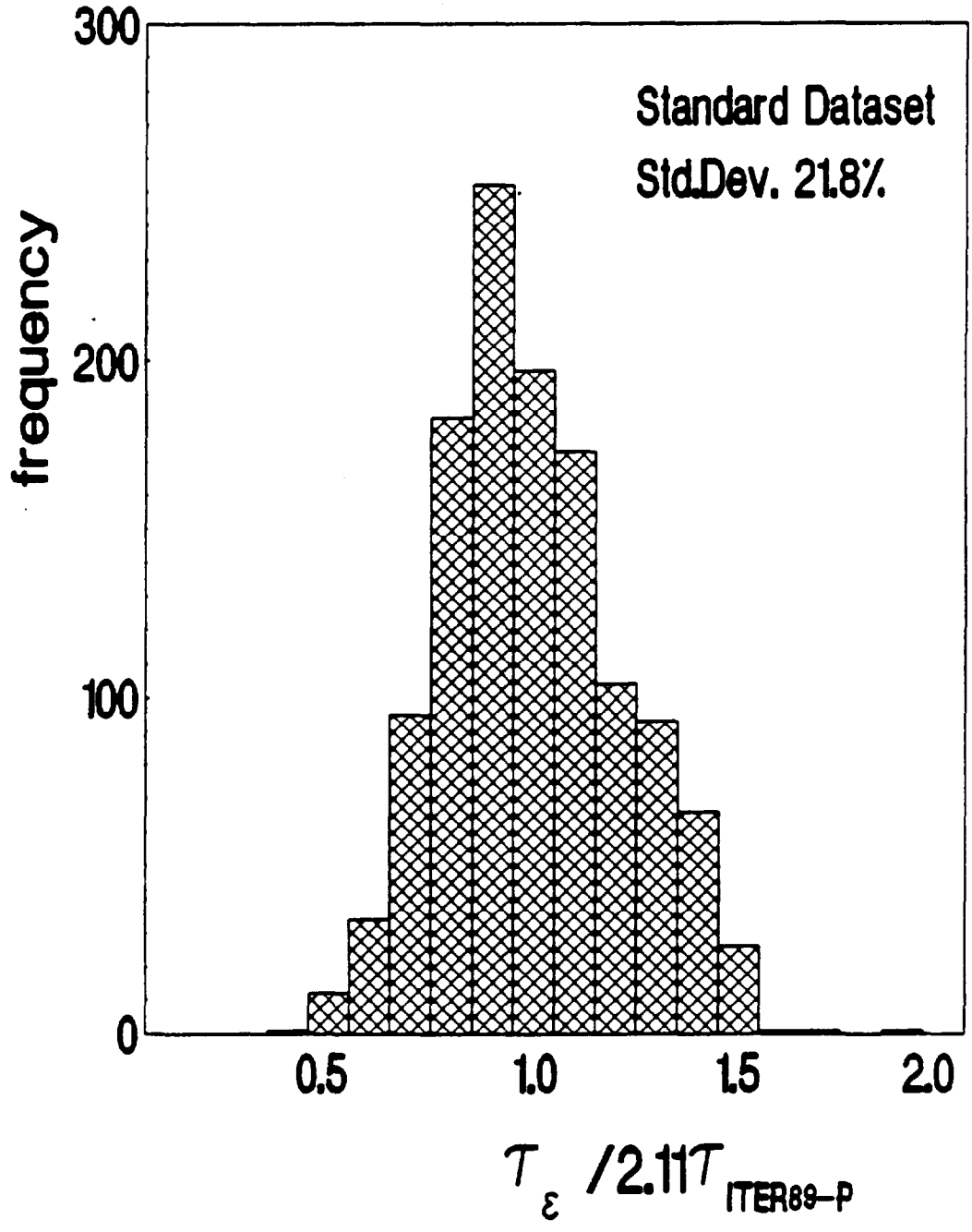
300
200
100
0
frequency
Standard Dataset
Std.Dev. 21.8%
0.5
1.0
1.5
2.0
τ_ε /2.11$\tau_{ITER89-P}$

Fig.12a

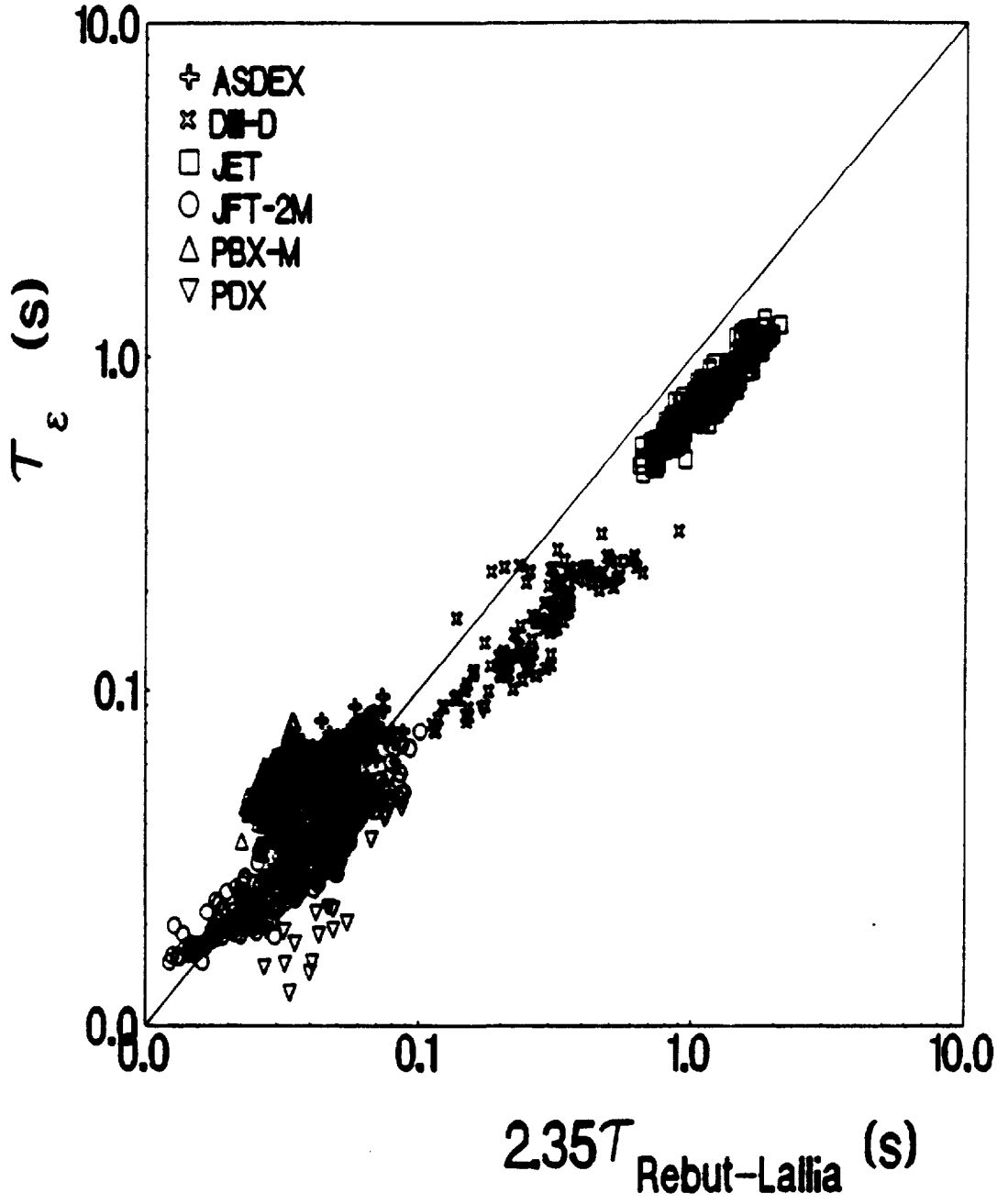
10.0
1.0
0.1
0.0
0.0
0.1
1.0
10.0
ASDEX
DIII-D
JET
JFT-2M
PBX-M
PDX
τ_ε (s)
$2.35\tau_{\text{Rebut-Lallia}}$ (s)

Fig.12b

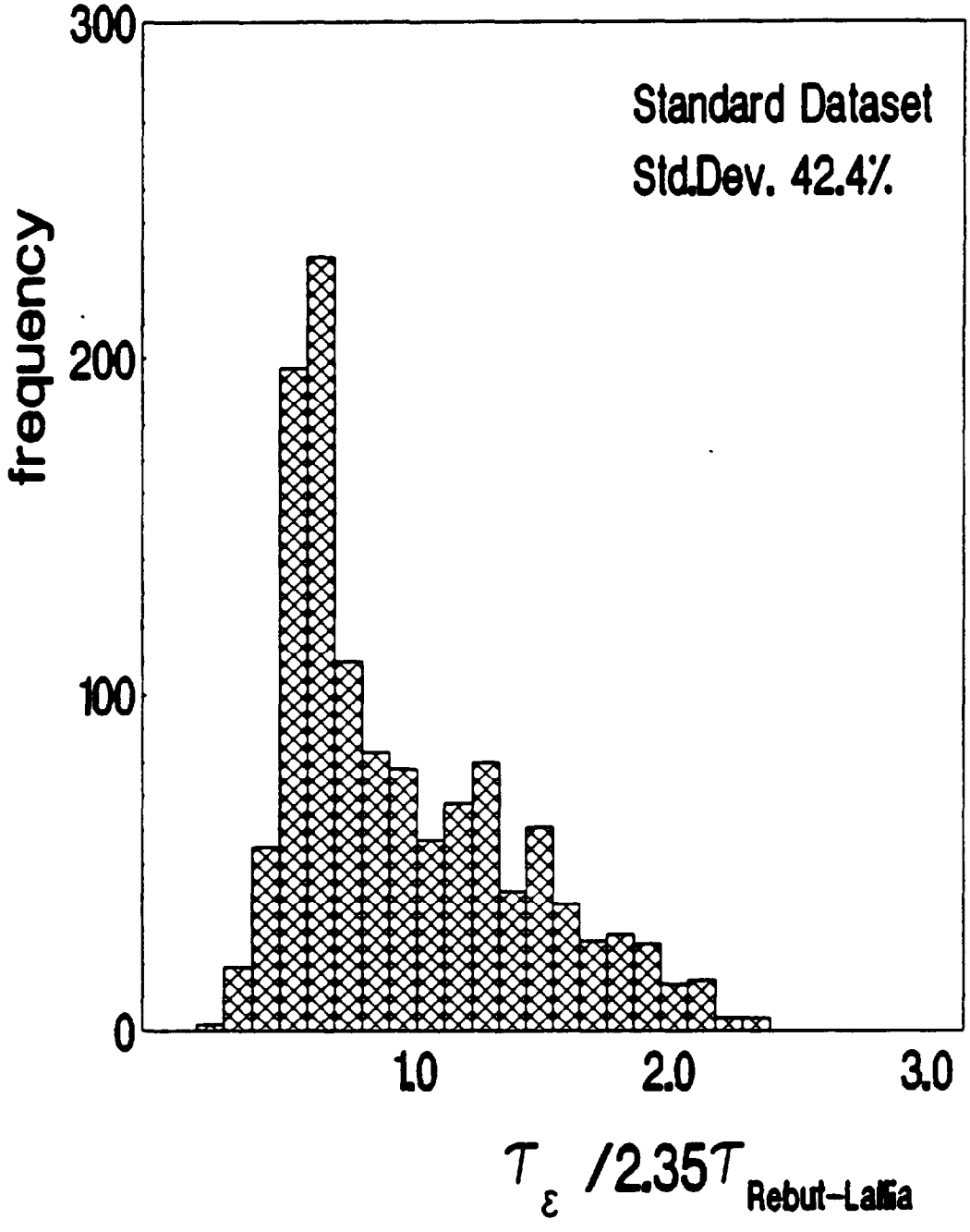
300
200
100
0
frequency
Standard Dataset
Std.Dev. 42.4%
1.0
2.0
3.0
τ_ε /2.35τ Rebut-Lafia

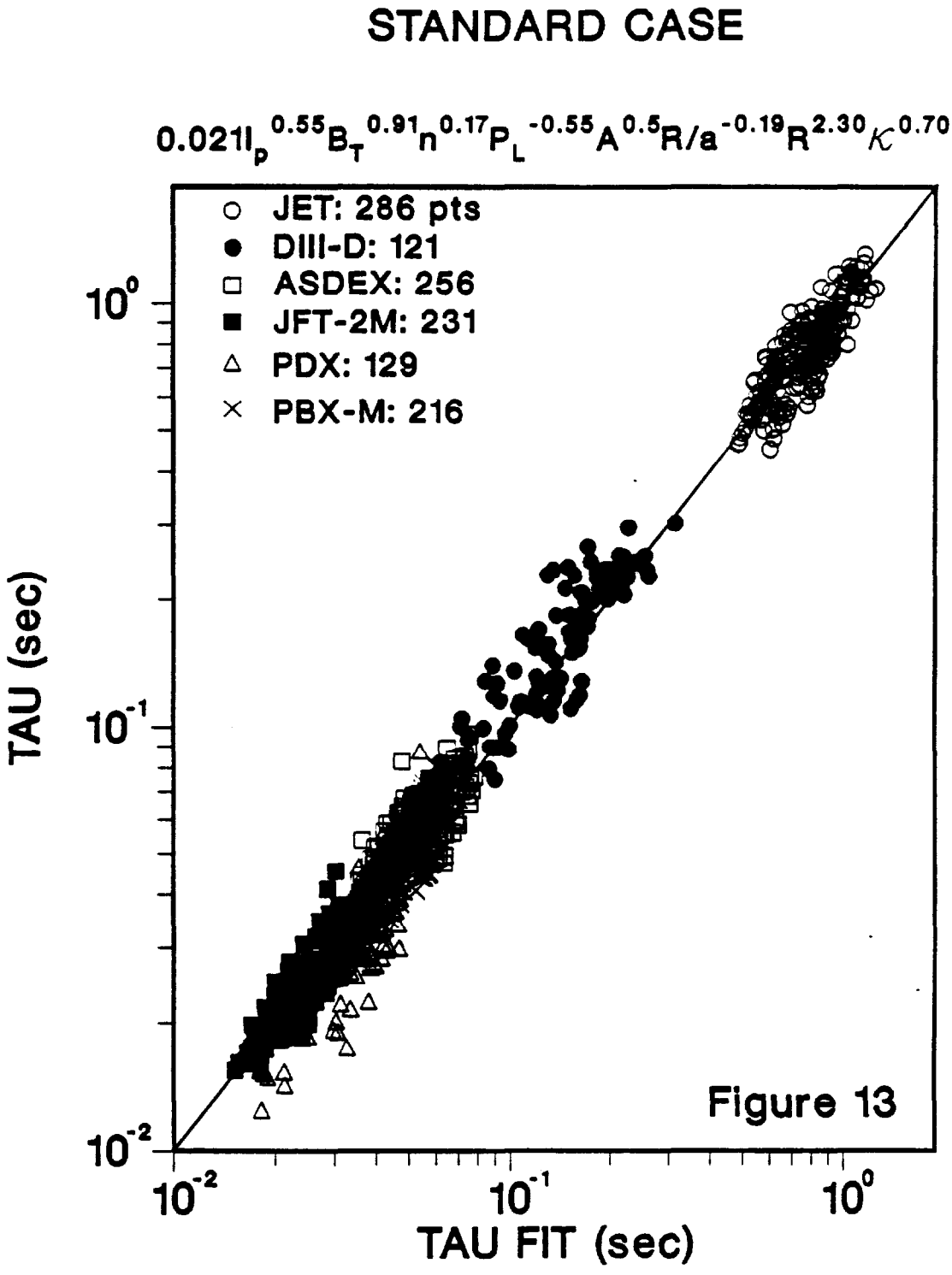
STANDARD CASE
$0.021 I_p^{0.55} B_T^{0.91} n^{0.17} P_L^{-0.55} A^{0.5} R/a^{-0.19} R^{2.30} \kappa^{0.70}$
JET: 286 pts
DIII-D: 121
ASDEX: 256
JFT-2M: 231
PDX: 129
PBX-M: 216
TAU (sec)
TAU FIT (sec)
10^{0}
10^{-1}
10^{-2}
Figure 13

Figure 13

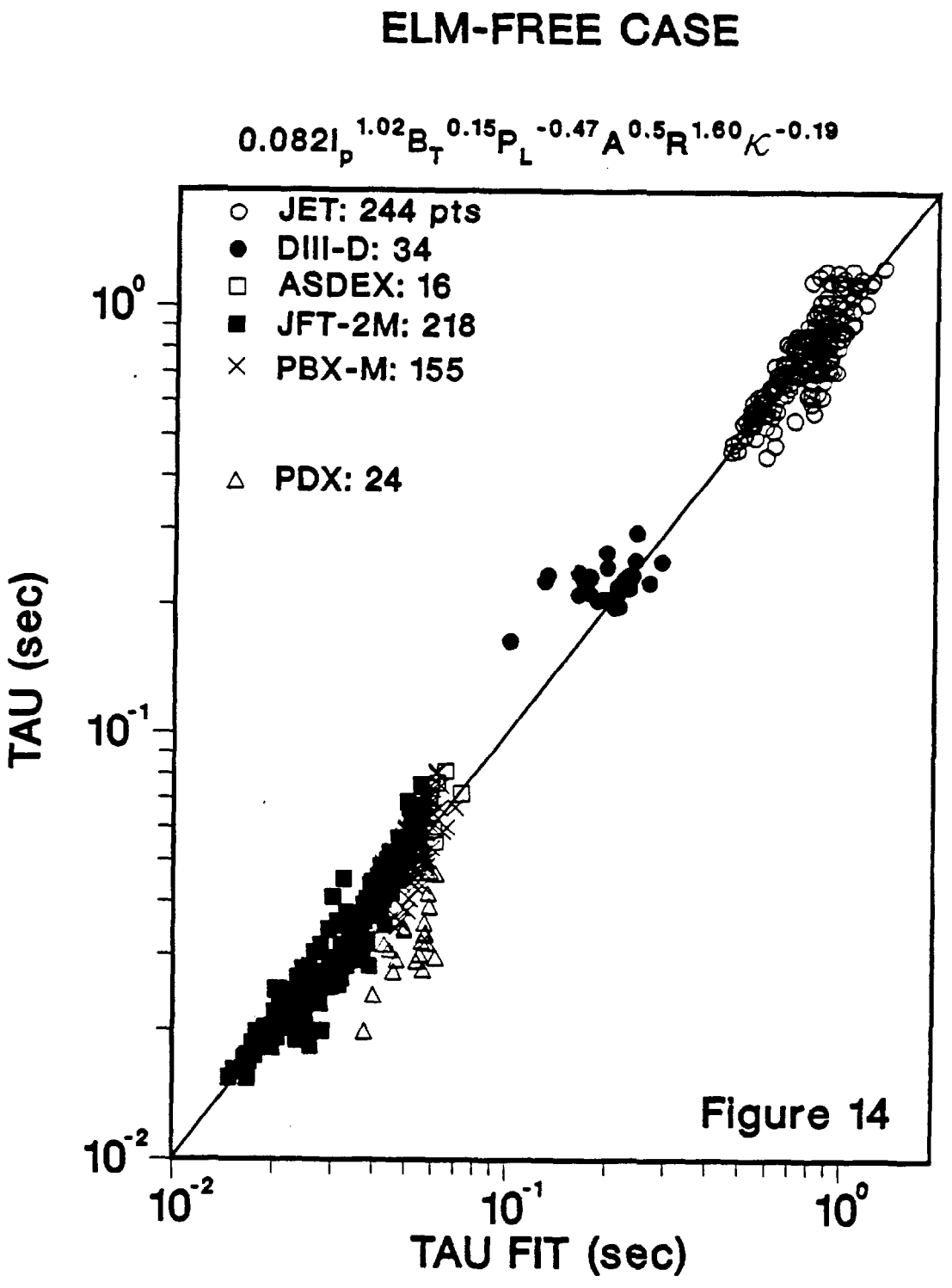
ELM-FREE CASE
$0.082I_p^{1.02}B_T^{0.15}P_L^{-0.47}A^{0.5}R^{1.60}\kappa^{-0.19}$
JET: 244 pts
DIII-D: 34
ASDEX: 16
JFT-2M: 218
PBX-M: 155
PDX: 24
TAU (sec)
TAU FIT (sec)
10^0
10^{-1}
10^{-2}
Figure 14

Figure 14

H – MODE SCALING

(ELM – free)

$$0.026\, I_p^{0.85} B_T^{0.6} P_L^{-0.55} A^{0.5} R^{1.85} \kappa^{0.75} (a/R)^{-0.1} n_e^{0.1}$$

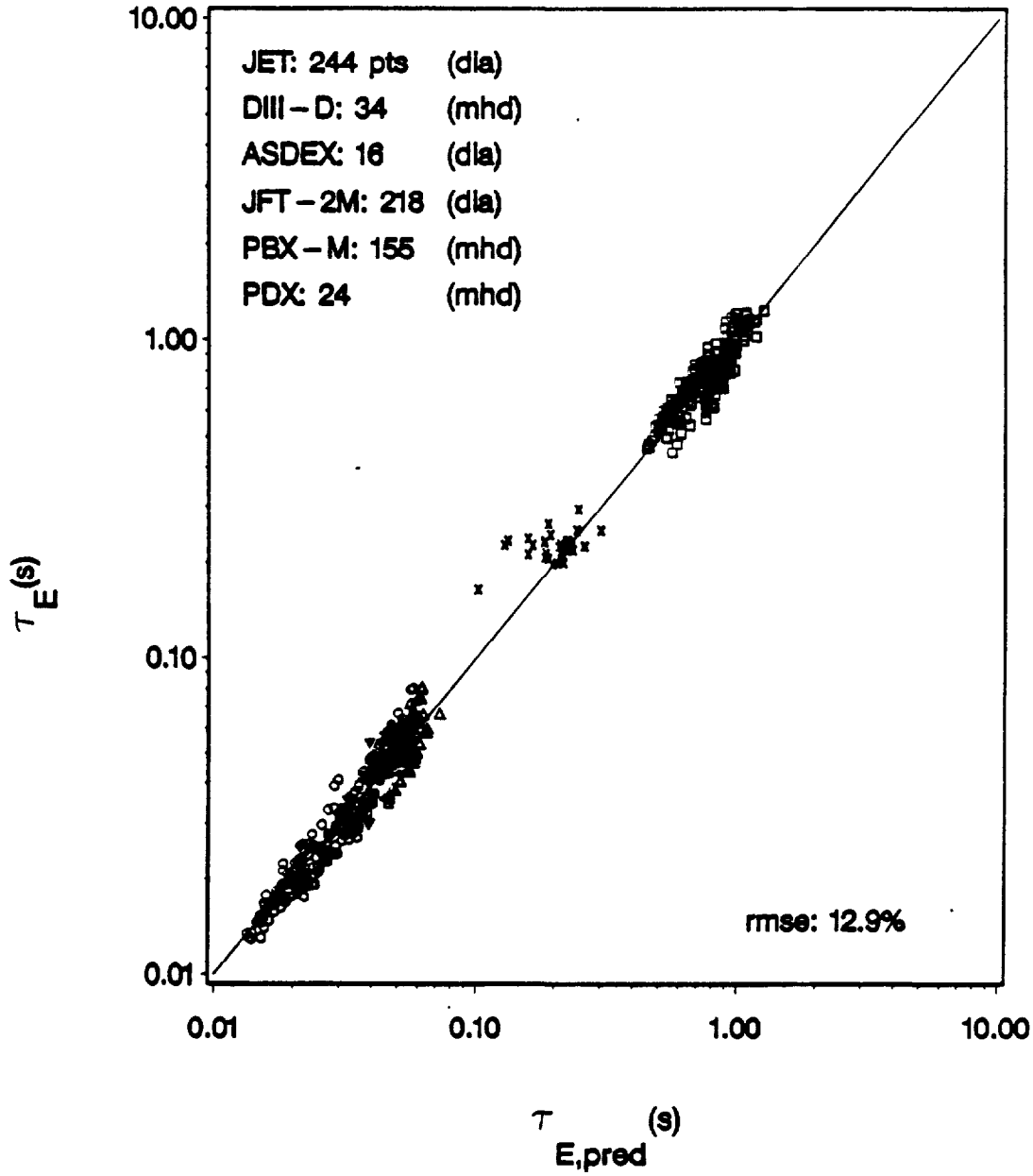

TOK +++ ASDEX XXX DIII-D □□□ JET ○○○ JFT2M △△△ PBXM ▼▼▼ PDX

(Standard dataset)

Figure 15

Figure 16

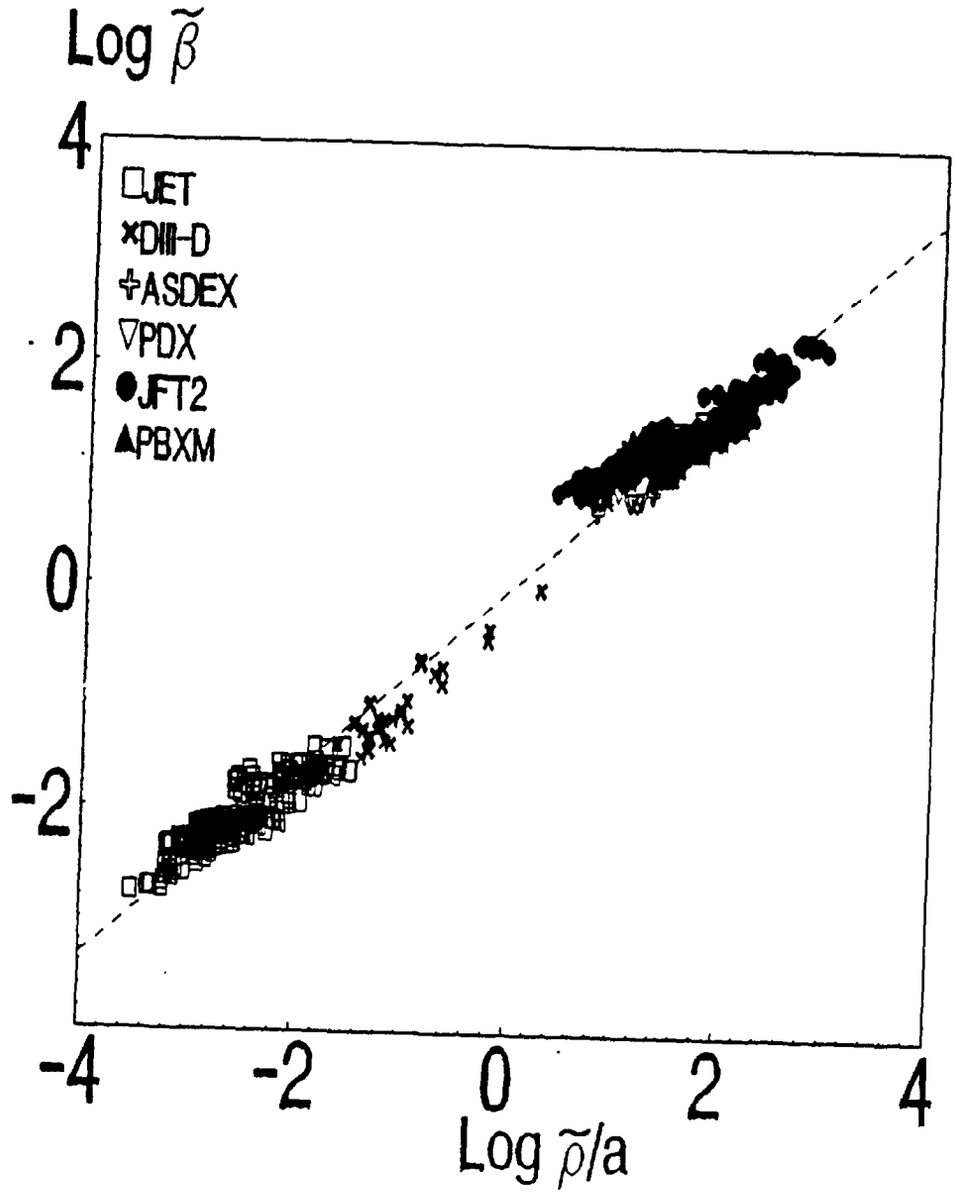
Log $\tilde{\beta}$
4
2
0
-2
-4
-2
0
2
4
Log $\tilde{\rho}$/a
□JET
×DIII-D
+ASDEX
▽PDX
●JFT2
▲PBXM

Figure 17

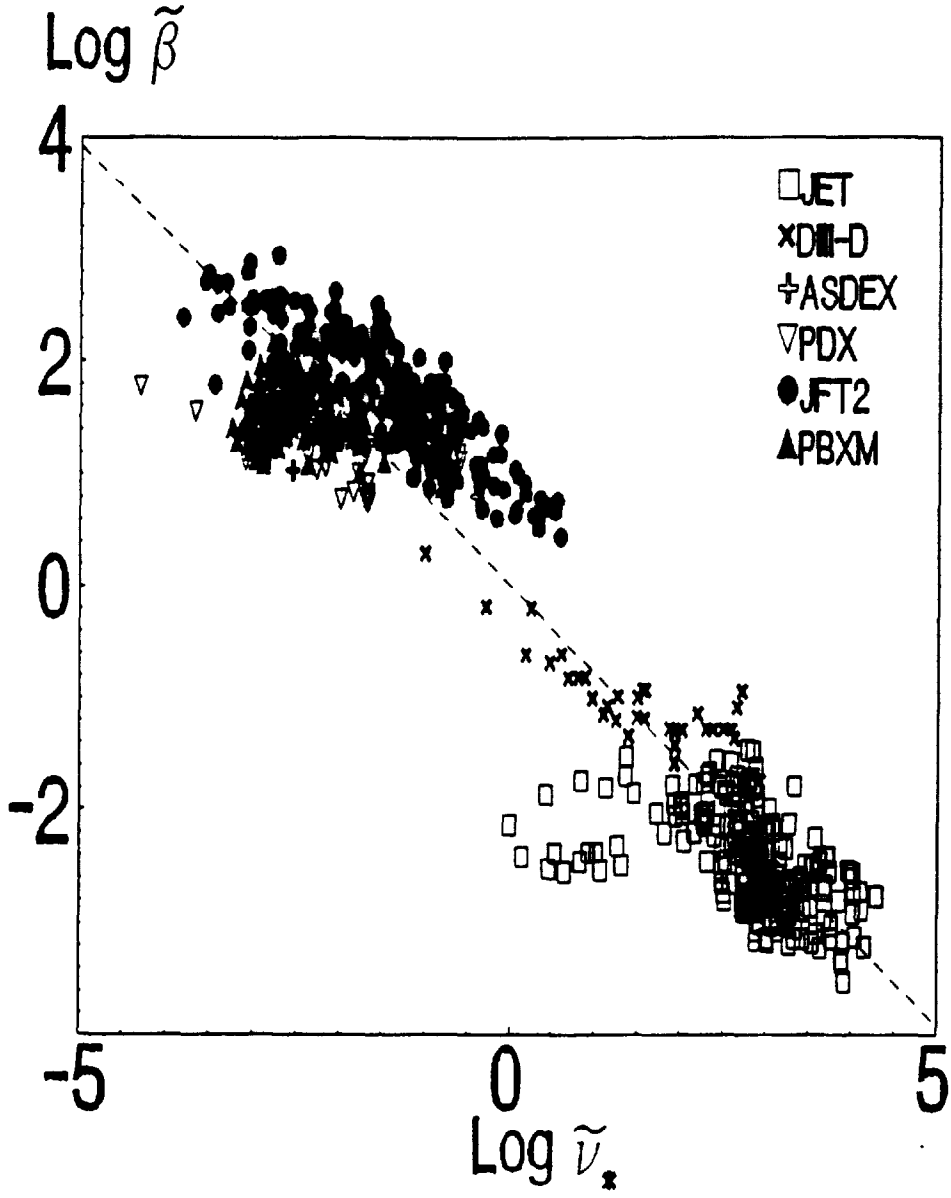
Log $\tilde{\beta}$
4
2
0
-2
-5
0
5
Log $\tilde{\nu}_*$
JET
DIII-D
ASDEX
PDX
JFT2
PBXM

Figure 18

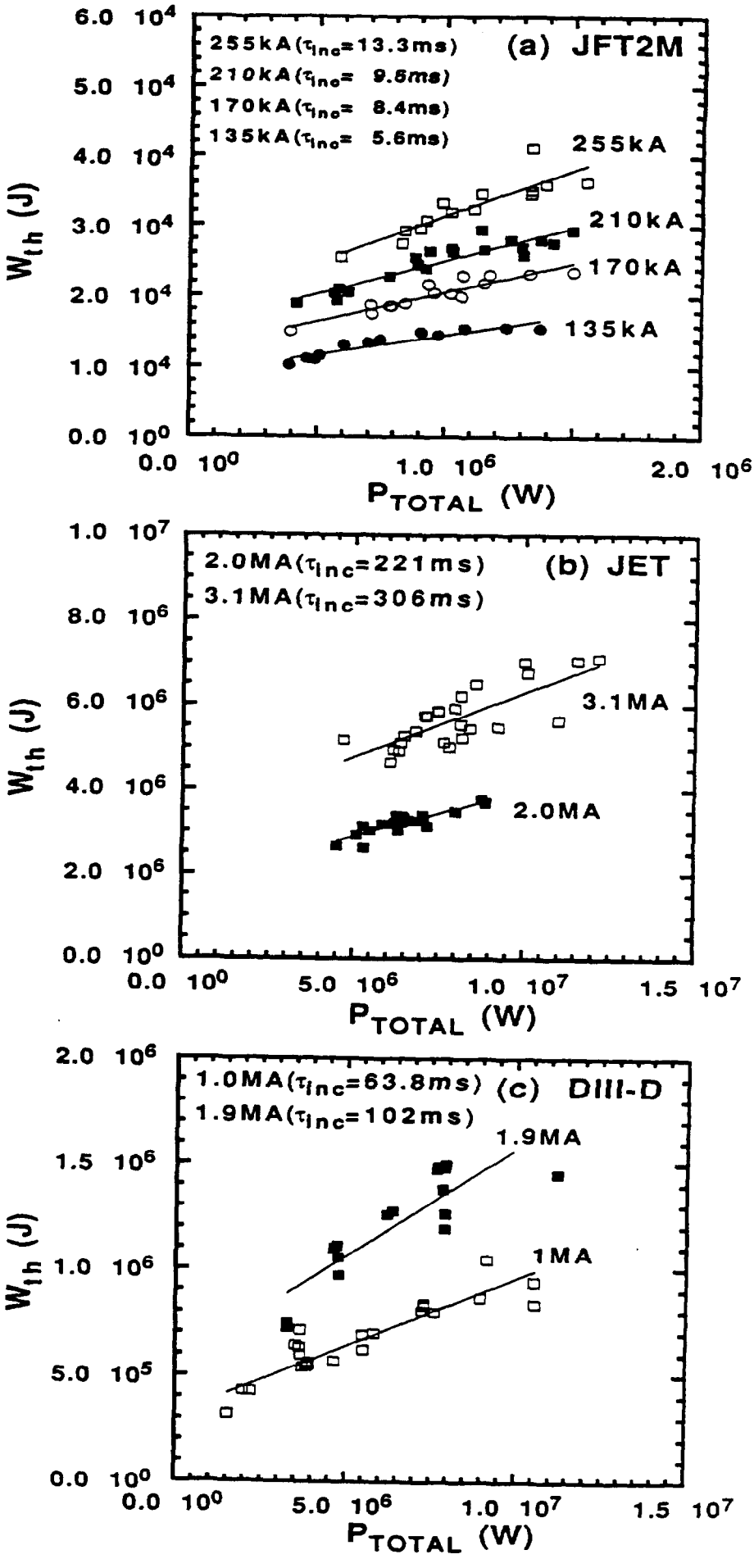
255kA(τinc=13.3ms)
210kA(τinc= 9.5ms)
170kA(τinc= 8.4ms)
135kA(τinc= 5.6ms)
(a) JFT2M
255kA
210kA
170kA
135kA
Wth (J)
PTOTAL (W)
2.0MA(τinc=221ms)
3.1MA(τinc=306ms)
(b) JET
3.1MA
2.0MA
1.0MA(τinc=63.8ms)
1.9MA(τinc=102ms)
(c) DIII-D
1.9MA
1MA

Figure 19

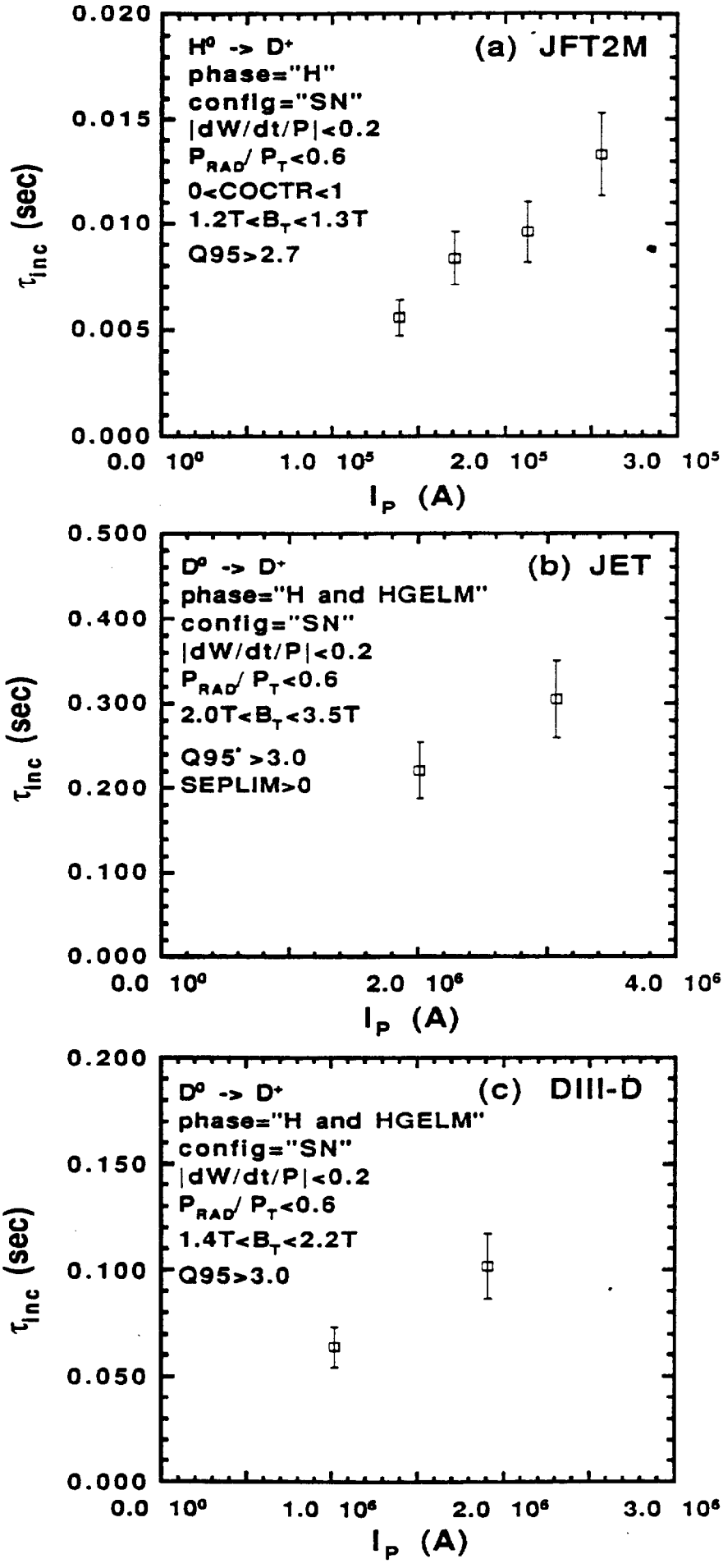
H⁰ -> D⁺
phase="H"
config="SN"
|dW/dt/P|<0.2
P_RAD/ P_T<0.6
0<COCTR<1
1.2T<B_T<1.3T
Q95>2.7
(a) JFT2M
τ_inc (sec)
0.020
0.015
0.010
0.005
0.000
0.0 10⁰ 1.0 10⁵ 2.0 10⁵ 3.0 10⁵
I_P (A)
D⁰ -> D⁺
phase="H and HGELM"
config="SN"
|dW/dt/P|<0.2
P_RAD/ P_T<0.6
2.0T<B_T<3.5T
Q95 >3.0
SEPLIM>0
(b) JET
τ_inc (sec)
0.500
0.400
0.300
0.200
0.100
0.000
0.0 10⁰ 2.0 10⁶ 4.0 10⁶
I_P (A)
D⁰ -> D⁺
phase="H and HGELM"
config="SN"
|dW/dt/P|<0.2
P_RAD/ P_T<0.6
1.4T<B_T<2.2T
Q95>3.0
(c) DIII-D
τ_inc (sec)
0.200
0.150
0.100
0.050
0.000
0.0 10⁰ 1.0 10⁶ 2.0 10⁶ 3.0 10⁶
I_P (A)

Figure 20

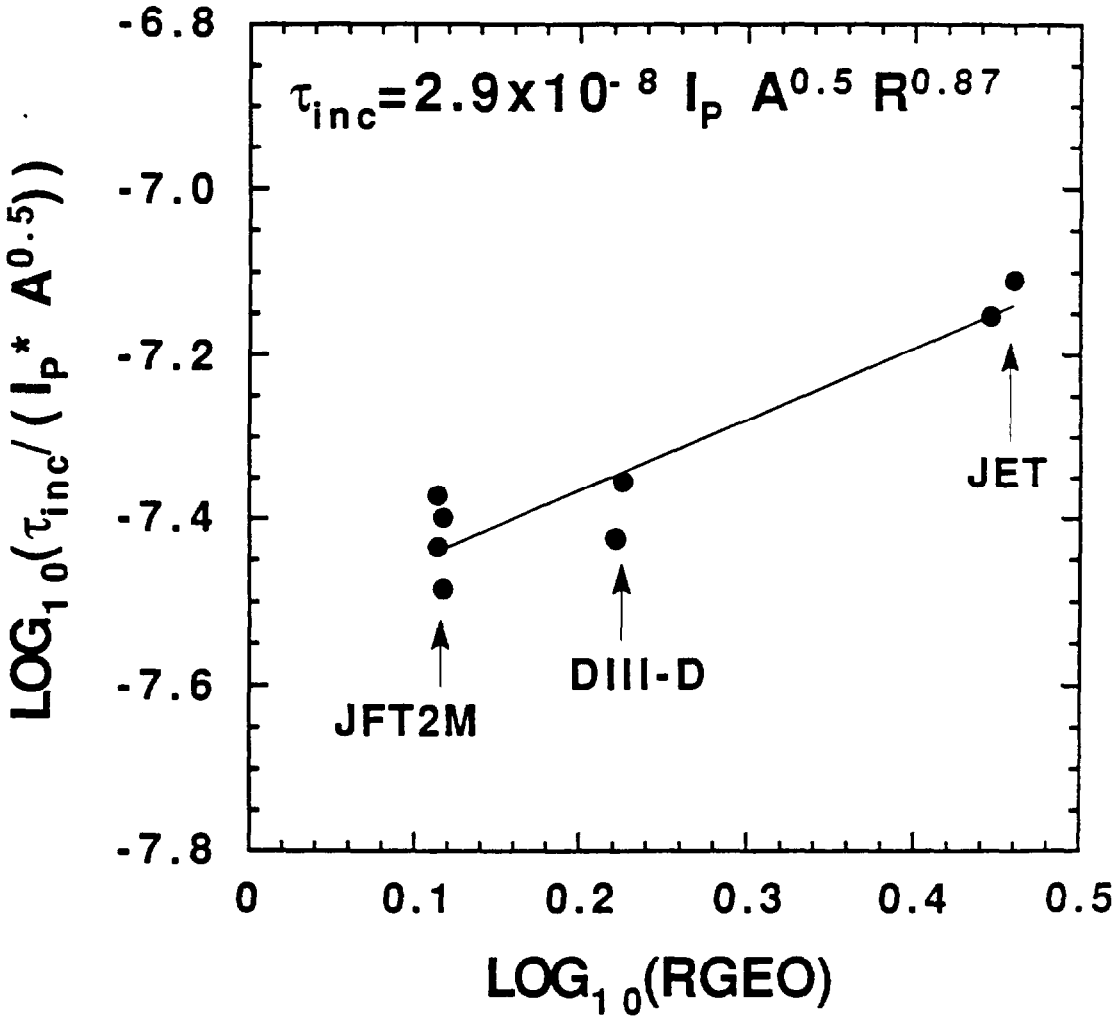
$\tau_{inc}=2.9x10^{-8}\ I_P\ A^{0.5}\ R^{0.87}$
$LOG_{10}(\tau_{inc}/(I_P^*\ A^{0.5}))$
-6.8
-7.0
-7.2
-7.4
-7.6
-7.8
0
0.1
0.2
0.3
0.4
0.5
$LOG_{10}(RGEO)$
JET
DIII-D
JFT2M

Figure 21

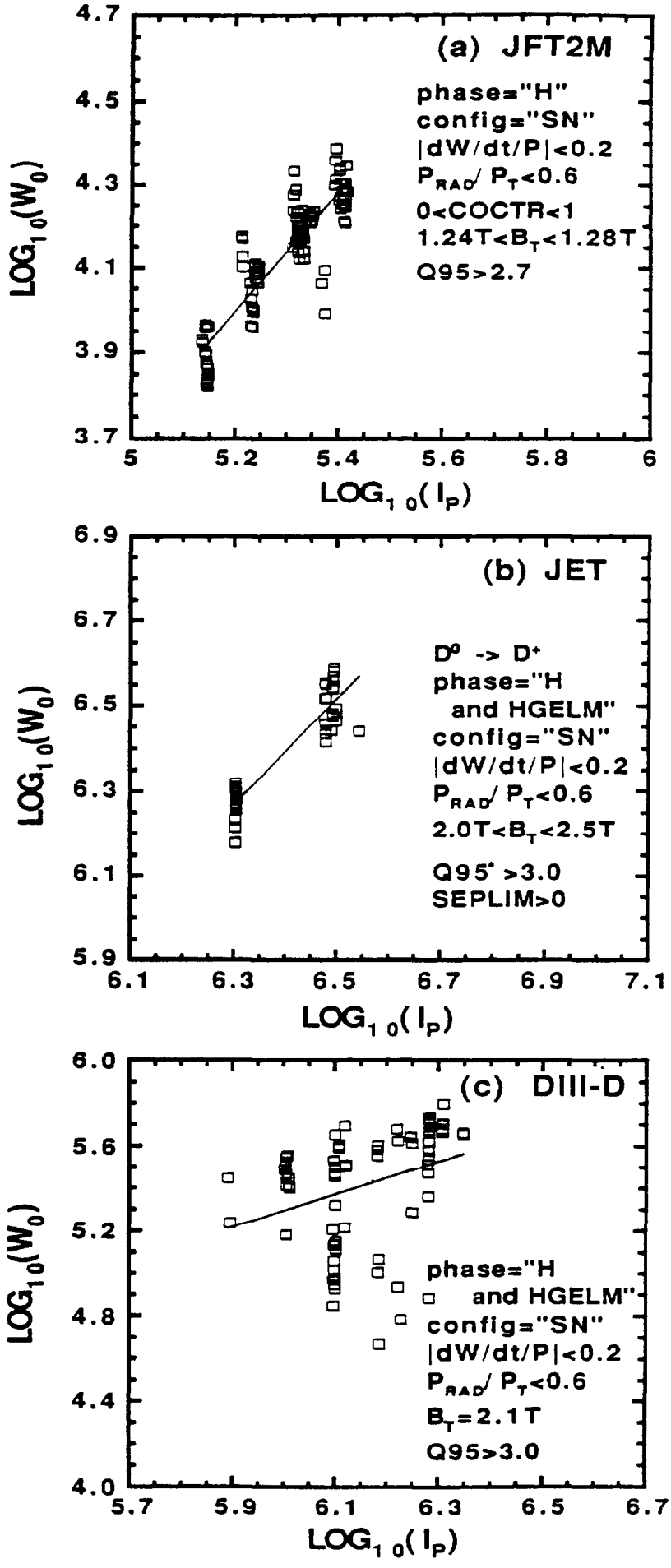
(a) JFT2M
phase="H"
config="SN"
|dW/dt/P|<0.2
P_RAD/ P_T<0.6
0<COCTR<1
1.24T<B_T<1.28T
Q95>2.7
LOG10(W0)
LOG10(IP)
(b) JET
D0 -> D+
phase="H
and HGELM"
config="SN"
|dW/dt/P|<0.2
P_RAD/ P_T<0.6
2.0T<B_T<2.5T
Q95 >3.0
SEPLIM>0
LOG10(W0)
LOG10(IP)
(c) DIII-D
phase="H
and HGELM"
config="SN"
|dW/dt/P|<0.2
P_RAD/ P_T<0.6
B_T=2.1T
Q95>3.0
LOG10(W0)
LOG10(IP)

Figure 22

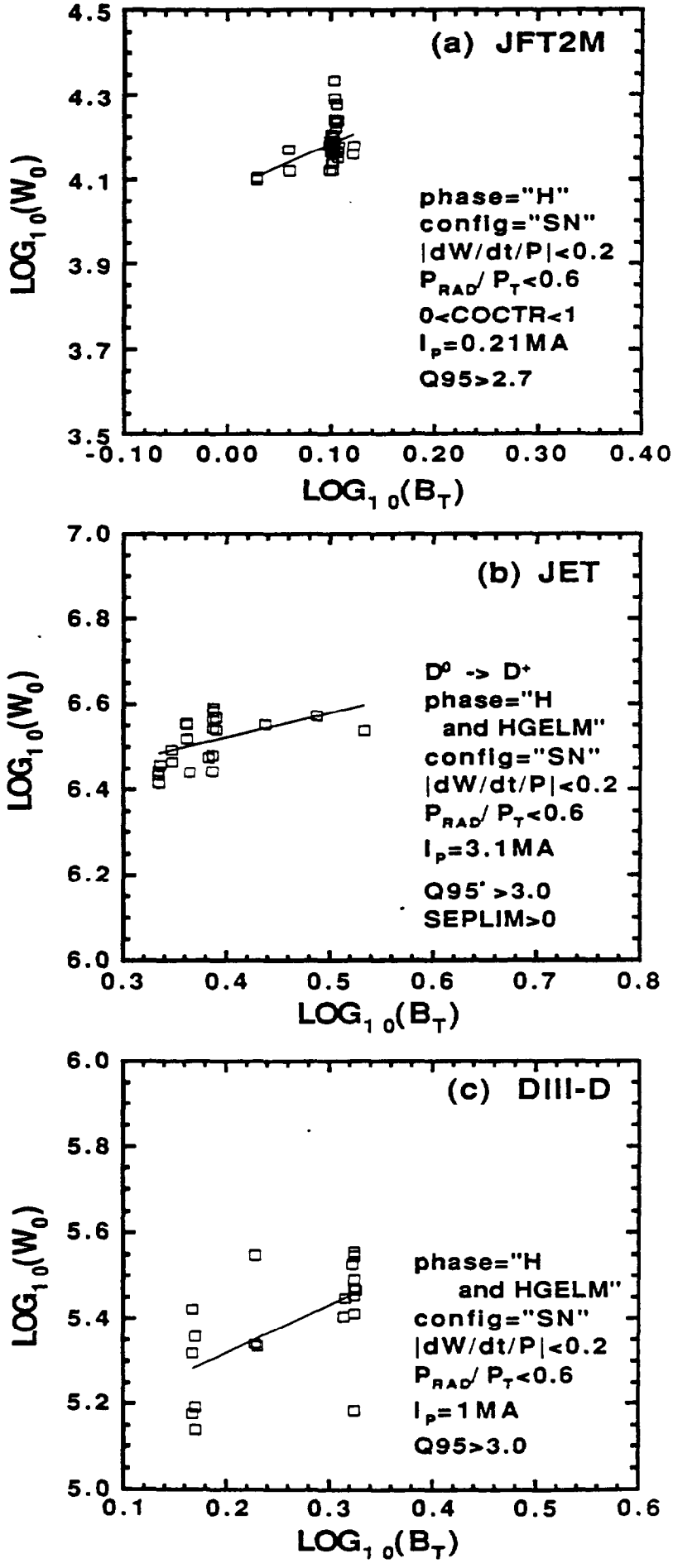
(a) JFT2M
phase="H"
config="SN"
|dW/dt/P|<0.2
P_RAD/ P_T<0.6
0<COCTR<1
I_p=0.21MA
Q95>2.7
LOG_10(W_0)
LOG_10(B_T)
(b) JET
D0 -> D+
phase="H
and HGELM"
config="SN"
|dW/dt/P|<0.2
P_RAD/ P_T<0.6
I_p=3.1MA
Q95>3.0
SEPLIM>0
LOG_10(W_0)
LOG_10(B_T)
(c) DIII-D
phase="H
and HGELM"
config="SN"
|dW/dt/P|<0.2
P_RAD/ P_T<0.6
I_p=1MA
Q95>3.0
LOG_10(W_0)
LOG_10(B_T)

Figure 23

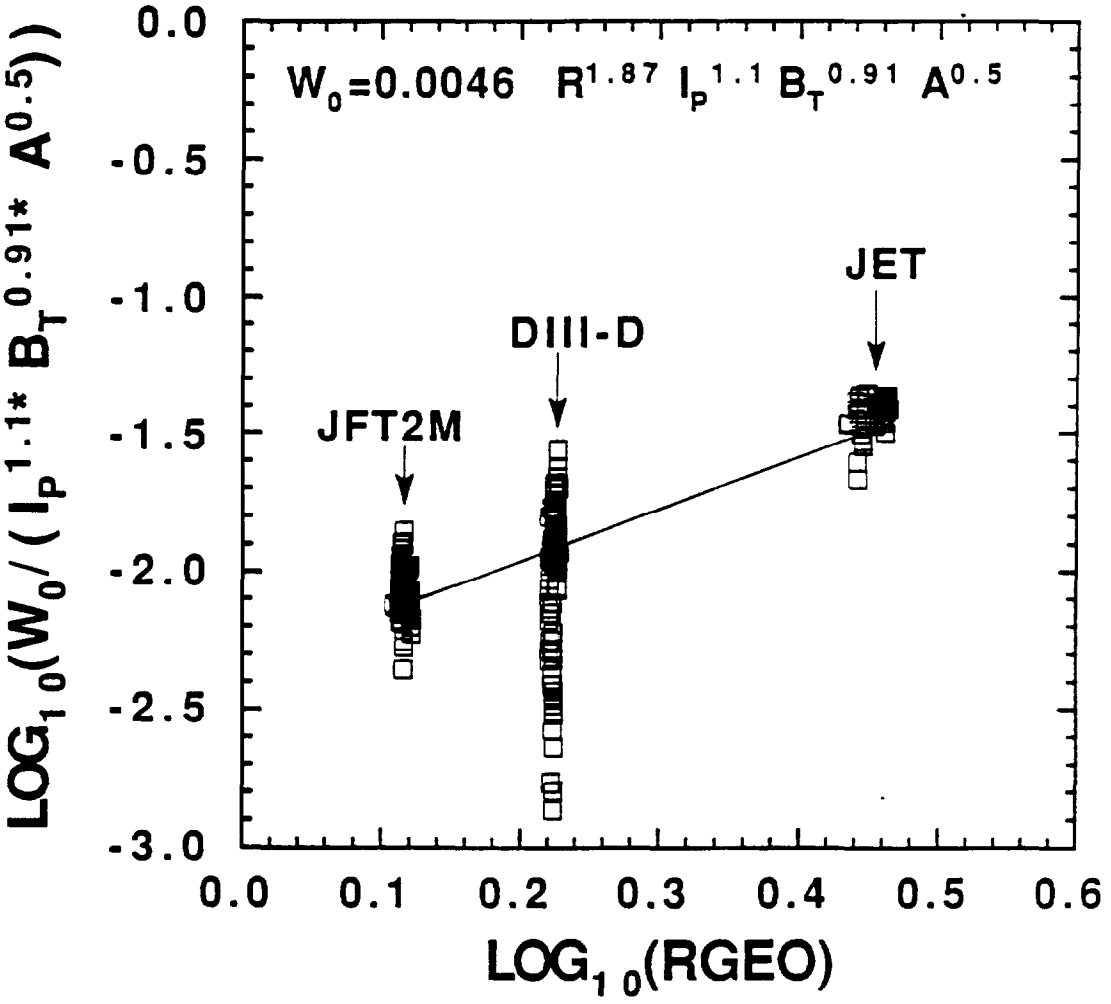
W_0=0.0046 $R^{1.87}$ $I_p^{1.1}$ $B_T^{0.91}$ $A^{0.5}$
JET
DIII-D
JFT2M
$LOG_{10}(W_0/(I_p^{1.1}* B_T^{0.91}* A^{0.5}))$
LOG_{10}(RGEO)
0.0
-0.5
-1.0
-1.5
-2.0
-2.5
-3.0
0.0
0.1
0.2
0.3
0.4
0.5
0.6

Figure 24

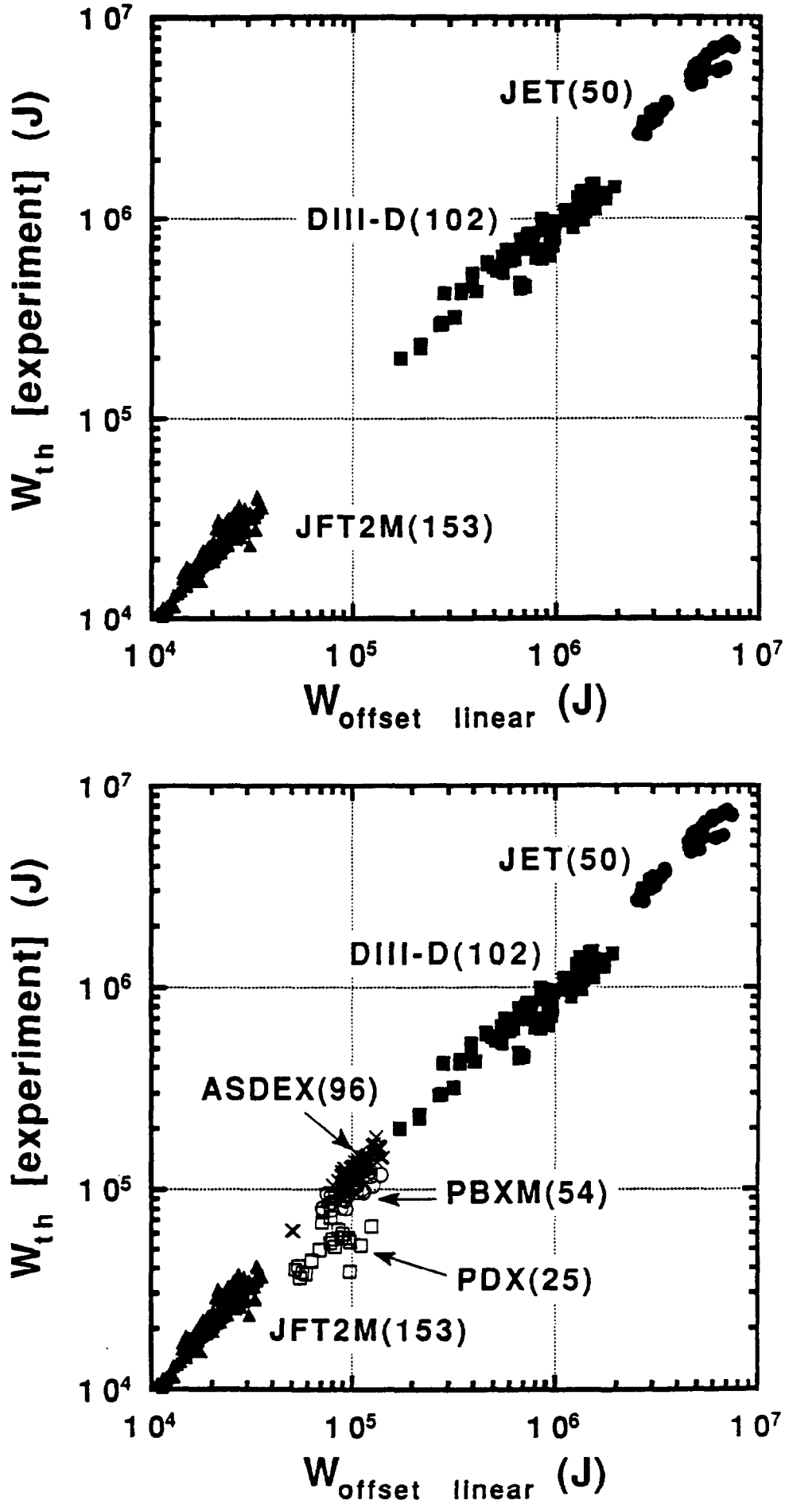
1 0^7
1 0^6
1 0^5
1 0^4
W_th [experiment] (J)
JET(50)
DIII-D(102)
JFT2M(153)
1 0^4
1 0^5
1 0^6
1 0^7
W_offset linear (J)
1 0^7
1 0^6
1 0^5
1 0^4
W_th [experiment] (J)
JET(50)
DIII-D(102)
ASDEX(96)
PBXM(54)
PDX(25)
JFT2M(153)
1 0^4
1 0^5
1 0^6
1 0^7
W_offset linear (J)

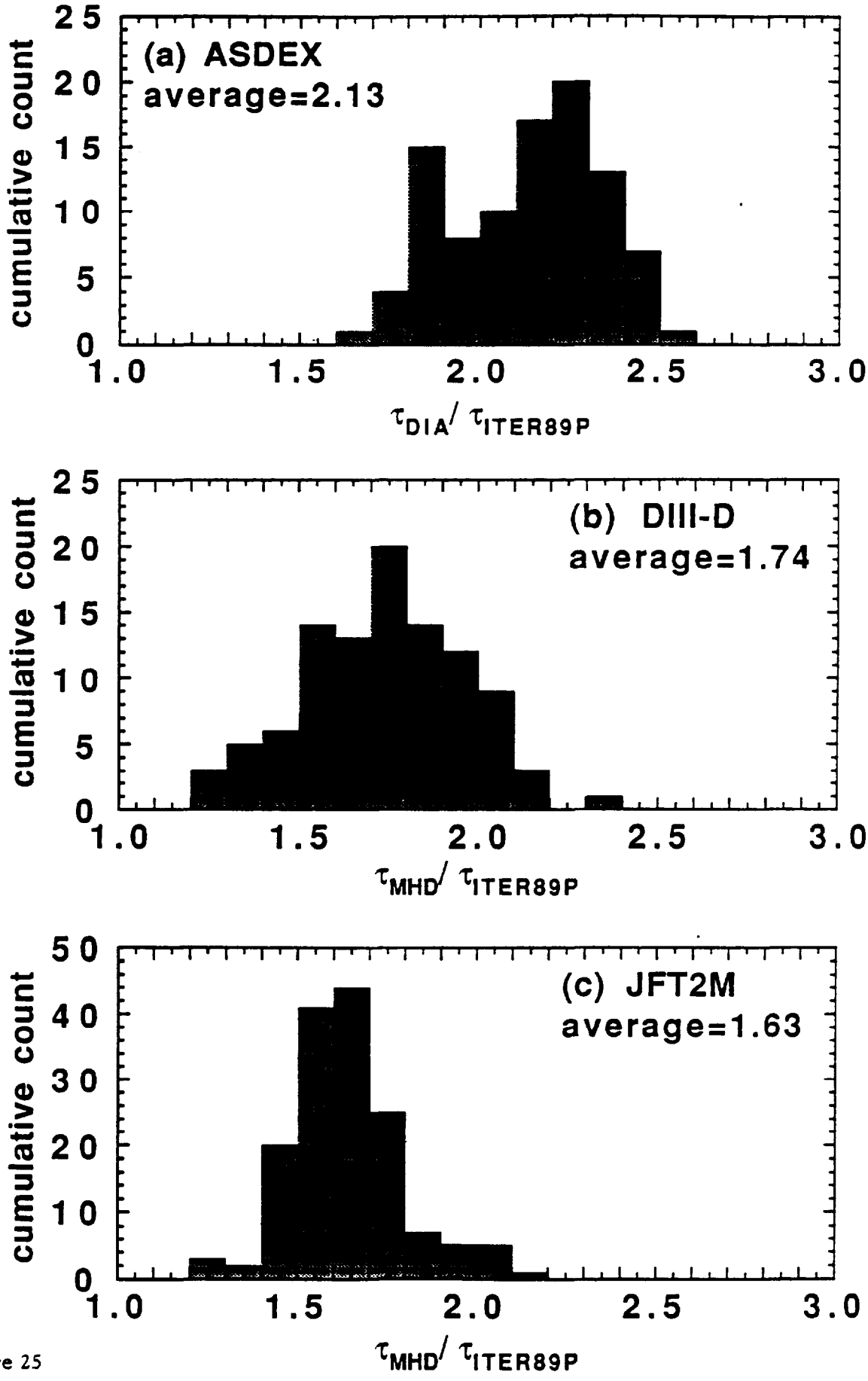
(a) ASDEX
average=2.13
cumulative count
25
20
15
10
5
0
1.0
1.5
2.0
2.5
3.0
τDIA/ τITER89P
(b) DIII-D
average=1.74
cumulative count
25
20
15
10
5
0
1.0
1.5
2.0
2.5
3.0
τMHD/ τITER89P
(c) JFT2M
average=1.63
cumulative count
50
40
30
20
10
0
1.0
1.5
2.0
2.5
3.0
τMHD/ τITER89P

Figure 25

Appendix I

THE JET TEAM

JET Joint Undertaking, Abingdon, Oxon, OX14 3EA, U.K.

J.M. Adams[1], H. Altmann, A. Andersen[14], P. Andrew[18], M. Angelone[29], S.A. Arshad, W. Bailey, P. Ballantyne, B. Balet, P. Barabaschi, R. Barnsley[2], M. Baronian, D.V. Bartlett, A.C. Bell, I. Benfatto[5], G. Benali, H. Bergsaker[11], P. Bertoldi, E. Bertolini, V. Bhatnagar, A.J. Bickley, H. Bindslev[14], T. Bonicelli, S.J. Booth, G. Bosia, M. Botman, D. Boucher, P. Boucquey, P. Breger, H. Brelen, H. Brinkschulte, T. Brown, M. Brusati, T. Budd, M. Bures, T. Businaro, P. Butcher, H. Buttgereit, C. Caldwell-Nichols, D.J. Campbell, P. Card, G. Celentano, C.D. Challis, A.V.Chankin[23], D. Chiron, J. Christiansen, C. Christodoulopoulos, P. Chuilon, R. Claesen, S. Clement, E. Clipsham, J.P. Coad, M. Comiskey[4], S. Conroy, M. Cooke, S. Cooper, J.G. Cordey, W. Core, G. Corrigan, S. Corti, A.E. Costley, G. Cottrell, M. Cox[7], P. Cripwell, H. de Blank[15], H. de Esch, L. de Kock, E. Deksnis, G.B. Denne-Hinnov, G. Deschamps, K.J. Dietz, S.L. Dmitrenko, J. Dobbing, N. Dolgetta, S.E. Dorling, P.G. Doyle, D.F. Düchs, H. Duquenoy, A. Edwards, J. Ehrenberg, A. Ekedahl, T. Elevant[11], S.K. Erents[7], L.G. Eriksson, H. Fajemirokun[12], H. Falter, D. Flory, J. Freiling[15], C. Froger, P. Froissard, K. Fullard, M. Gadeberg, A. Galetsas, D. Gambier, M. Garribba, P. Gaze, R. Giannella, A. Gibson, R.D. Gill, A. Girard, A. Gondhalekar, C. Gormezano, N.A. Gottardi, C. Gowers, B.J. Green, R. Haange, G Haas, A. Haigh, G. Hammett[6], C.J. Hancock, P.J. Harbour, N.C. Hawkes[7], P. Haynes[7], J.L. Hemmerich, T. Hender[7], F.B. Herzog, R.F. Herzog, J. Hoekzema, J. How, M. Huart, L Hughes, T.P. Hughes[4], M. Hugon, M. Huguet, A. Hwang[7], B. Ingram, M. Irving, J. Jacquinot, H. Jaeckel, J.F. Jaeger, G. Janeschitz[13], S. Jankowicz[22], O.N. Jarvis, F. Jensen, E.M. Jones, L.P.D.F. Jones, T.T.C. Jones, J-F. Junger, E. Junique, A. Kaye, B.E. Keen, M. Keilhacker, G.J. Kelly, W. Kerner, R. Konig, A. Konstantellos, M. Kovanen[20], G. Kramer[15], P. Kupschus, R. Lässer, J.R. Last, B. Laundy, L. Lauro-Taroni, K. Lawson[7], M. Lennholm, A. Loarte, R. Lobel, P. Lomas, M. Loughlin, C. Lowry, B. Macklin, G. Maddison[7], G. Magyar, W. Mandl[13], V. Marchese, F. Marcus, J. Mart, E. Martin, R. Martin-Solis[8], P. Massmann, G. McCracken[7], P. Meriguet, P. Miele, S.F. Mills, P. Millward, R. Mohanti[17], P.L. Mondino, A. Montvai[3], S. Moriyama[28], P. Morgan, H. Morsi, G. Murphy, M. Mynarends, R. Myrnäs[16], C. Nardone, F. Nave[21], G. Newbert, M. Newman, P. Nielsen, P. Noll, W. Obert, D. O'Brien, J. O'Rourke, R. Ostrom, M. Ottaviani, M. Pain, F. Paoletti, S. Papastergiou, D. Pasini, A. Peacock, N. Peacock[7], D. Pearson[12], R. Pepe de Silva, G. Perinic, C. Perry, M. Pick, R. Pitts[7], J. Plancoulaine, J-P. Poffé, F. Porcelli, L. Porte[19], R. Prentice, S. Puppin, S. Putvinsko[23], G. Radford[9], T. Raimondi, M.C. Ramos de Andrade, P-H. Rebut, R. Reichle, E. Righi, F. Rimini, D. Robinson[7], A. Rolfe, R.T. Ross, L. Rossi, R. Russ, P. Rutter, H.C. Sack, G. Sadler, G. Saibene, J.L. Salanave, G. Sanazzaro, A. Santagiustina, R. Sartori, C. Sborchia, P. Schild, M. Schmid, G. Schmidt[6], B. Schunke, S.M. Scott, A. Sibley, R. Simonini, A.C.C. Sips, P. Smeulders, R. Stankiewicz[27], M. Stamp, P. Stangeby[18], D.F. Start, C.A. Steed, D. Stork, P.E. Stott, T.E. Stringer, P. Stubberfield, D. Summers, H. Summers[19], L. Svensson, J.A. Tagle[21], A. Tanga, A. Taroni, A. Tesini, P.R. Thomas, E. Thompson, K. Thomsen, J.M. Todd, P. Trevalion, B. Tubbing, F. Tibone, E. Usselmann, H. van der Beken, G. Vlases, M. von Hellermann, T. Wade, C. Walker, R. Walton[6], D. Ward, M.L. Watkins, M.J. Watson, S. Weber[10], J. Wesson, T.J. Wijnands, J. Wilks, D. Wilson, T. Winkel, R. Wolf, B. Wolle[24], D. Wong, C. Woodward, Y. Wu[25], M. Wykes, I.D. Young, L. Zannelli, Y. Zhu[26], W. Zwingmann.

PERMANENT ADDRESSES

1. UKAEA, Harwell, Didcot, Oxon, UK.
2. University of Leicester, Leicester, UK.
3. Central Research Institute for Physics, Academy of Sciences, Budapest, Hungary.
4. University of Essex, Colchester, UK.
5. ENEA-CNR, Padova, Italy.
6. Princeton Plasma Physics Laboratory, New Jersey, USA.
7. UKAEA Culham Laboratory, Abingdon, Oxon, UK.
8. Universidad Complutense de Madrid, Spain.
9. Institute of Mathematics, University of Oxford, UK.
10. Freien Universität, Berlin, F.R.G.
11. Swedish Energy Research Commission, S-10072 Stockholm, Sweden.
12. Imperial College of Science and Technology, University of London, UK.
13. Max Planck Institut für Plasmaphysik, Garching bei München, FRG.
14. Risø National Laboratory, Denmark.
15. FOM Instituut voor Plasmafysica, 3430 Be Nieuwegein, The Netherlands.
16. University of Lund, Sweden.
17. North Carolina State University, Raleigh, NC, USA
18. Institute for Aerospace Studies, University of Toronto, Downsview, Ontario, Canada.
19. University of Strathclyde, 107 Rottenrow, Glasgow, UK.
20. Nuclear Engineering Laboratory, Lapeenranta University, Finland.
21. CIEMAT, Madrid, Spain.
22. Institute for Nuclear Studies, Otwock-Swierk, Poland.
23. Kurchatov Institute of Atomic Energy, Moscow, USSR
24. University of Heidelberg, Heidelberg, FRG.
25. Institute for Mechanics, Academia Sinica, Beijing, P.R. China.
26. Southwestern University of Physics, Leshan, P.R. China.
27. RCC Cyfronet, Otwock Swierk, Poland.
28. JAERI, Naka Fusion Research Establishment, Ibaraki, Japan.
29. ENEA, Frascati, Italy.

At 1st June 1991